Universidade do Porto

Faculdade de Engenharia

FEUP

AUTOMATIC ANALYSIS OF MAMMOGRAPHY IMAGES: ENHANCEMENT AND SEGMENTATION TECHNIQUES

Célia Freitas da Cruz

July 2011

Universidade do Porto
Faculdade de Engenharia
FEUP

Engineering Faculty – Porto University

AUTOMATIC ANALYSIS OF MAMMOGRAPHY IMAGES: ENHANCEMENT AND SEGMENTATION TECHNIQUES

M.Sc. Thesis

Célia Freitas da Cruz

Supervisor:
Prof. João Manuel R. S. Tavares (Ph.D)
Departamento de Engenharia Mecânica
Faculdade de Engenharia da Universidade do Porto

Porto, July 2011

Master in Bioengineering – Biomedical Engineering

To those who have suffered
from breast cancer.

ACKNOWLEDGMENTS

I greatly acknowledge Professor João Manuel R. S. Tavares for the support granted to this work.

I would also like to thank Serviço Médico de Imagem Computorizada (SMIC), in Porto, Portugal, and especially Dr. António Paulo Cardoso, for the availability to introduce me some radiology concepts and the clinic reality.

I would also like to acknowledge to all the doctors and clinical staff of Clínica da Mama of Hospital de São João, Porto, Portugal, for the availability for some clinical demonstrations.

I am indebted to all of my colleagues and friends to support me whenever I needed in many different numbers of ways. A special thanks for Carla Santos for all those moments and for my “work team” Ana Priscila Alves and Andreia Silva.

Lastly, I would like to show my immense gratitude to my family. They gave me wisdom to make my own decisions and support in the moments that I most need.

ABSTRACT

Breast cancer is the utmost usual cancer among the women world population. However, when premature detected, the treatment can be performed earlier and therefore be more efficient.

Mammography is the most common exam to early detect this disease. There are different lesions that are breast cancer characteristic such as microcalcifications which can be detected trough this technique.

Computed aided detection (CAD) intends to provide assistance to the mammography detection, reducing breast cancer misdiagnosis, thus allowing better diagnosis and more efficient treatments. CAD systems result of a collection of computed algorithms which characterize lesions through automatic image analysis.

The main aim of this master dissertation corresponds to the automatic enhancement and segmentation of microcalcifications in mammographic images. This dissertation includes implementation and application of image enhancement techniques such as contrast-limited histogram equalization, contrast stretching, adaptive neighborhood contrast enhancement, unsharp masking, adaptive unsharp masking and homomorphic filter, with the evaluation of several different parameters. The techniques were evaluated with emphasis on microcalcifications enhancement on real mammographic images, where the adaptive techniques had better performance. Image segmentation techniques were also implemented and applied, such as adaptive threshold, adaptive threshold followed by morphological operators, threshold and difference of Gaussians, region growing of selected areas, active contours of selected areas and edge detection. The segmentation technique edge detectors and regions growing of selected areas had higher sensitivity, while edge detection and threshold and difference of Gaussians had higher accuracy, precision and F-measure. A dataset was additionally created with the features extracted from the segmented objects and preliminary classification studies were performed. All the experiments were performed in a set of twenty real case mammograms with different breast densities from mini MIAS Database and implemented in MATLAB®.

KEYWORDS

Breast; Cancer; Computer-aided detection; Image analysis; Image processing; Mammography; Medical imaging; Microcalcification.

RESUMO

Cancro da mama corresponde ao cancro mais comum entre a população feminina mundial. No entanto, quando detectado precocemente, o seu tratamento pode ser realizado de modo mais eficiente.

A mamografia é o exame mais comummente usado para detectar esta doença. Existem diferentes lesões características do cancro da mama, tais como microcalcificações que podem ser detectados através desta técnica.

Detecção assistida por computador (CAD) pretende assistir a detecção de mamografia, reduzindo erros de diagnóstico e permitindo, assim, melhores diagnósticos e tratamentos mais eficientes. Sistemas CAD consistem em um conjunto de algoritmos computacionais que tentam caracterizar as lesões por meio de processamento e análise de imagem.

O objectivo principal desta dissertação corresponde ao melhoramento automático de mamografias, bem como a segmentação automática de microcalcificações. Esta dissertação inclui a implementação de técnicas de melhoramento de imagem, tais como equalização adaptativa de histograma com contraste limitado, alongamento do contraste no histograma, melhoramento do contraste por detecção adaptativa dos vizinhos, filtro de *unsharp,* filtro de *unsharp* adaptativo e filtro homomórfico. Foram testados diversos parâmetros dos vários algoritmos considerados. As técnicas adaptativas de melhoramento obtiveram melhor desempenho. Também foram implementadas técnicas de segmentação de imagem, tais como *threshold* adaptativo, *threshold* adaptativo seguido por operadores morfológicos, *threshold* e diferença de Gaussianos, *region growing* de áreas seleccionadas, contorno activos de áreas seleccionadas e detecção de contornos. A técnica de segmentação por detectores de contornos e *region growing* de áreas selecionadas obtiveram maior sensibilidade, enquanto *threshold* e diferença de Gaussianos e detectores de contornos obtiveram maior exatidão, precisão e *F-measure*. Um *dataset* foi ainda criado, com características extraídas dos objetos segmentados. Todos as implementações foram realizadas em MATLAB® e num conjunto de vinte casos reais de mamografias com densidades de mama variáveis retirados da base de dados mini-MIAS.

PALAVRAS-CHAVE

Análise de imagem, Cancro; Imagiologia médica; Mama; Mamografia; Microcalcificações; Processamento de imagem; Sistema de detecção auxiliada por computador.

CONTENTS

LIST OF FIGURES

List of Tables

GLOSSARY

AEC – Automatic Exposure Control

ANCE – Adaptive Neighborhood Contrast Enhancement

ANN – Artificial Neural Network

ASNR – Average Signal to Noise Ratio

BBN – Bayesian belief network

BIRADS – Breast imaging reporting and data system

BNL – Background noise level

CAD – Computer aided detection

CADx – Computer aided diagnosis

CC – Cranio-caudal

CII – Contrast Improvement Index

CLAHE – Contrast-limited adaptive histogram equalization

CR – Computed radiography

FDA – Food and Drug Administration

FFDM – Full Field Digital Mammography

FN – False negative

FNN – Fuzzy Nearest Neighbor

FNSE – Fixed-Neighborhood Statistical Enhancement

FP – False positive

FPI – False positive *per* image

FROC – Free-response receiver operating characteristic

FSM – Film-screen mammography

HNN – Hybrid Neural Network

KNN – K-Nearest Neighbors

MAR – Minimum aspect ratio

MLO – Mediolateral oblique

PSNR – Peak signal to noise ratio

ROC – Receiver operating characteristic

ROI – Region of interest

RVM – Relevance vector machine

SVM – Support vector machine

TP – True positive

TN – True negative

CHAPTER 1

INTRODUCTION

Breast cancer is the most common cancer among the women world population, affecting each year an average of 1.4 million people (Autier, et al., 2010).

Breast cancer comprises 1 in 5 of all new cases of cancer, Figure 1.1. It is also the most common form of cancer death, representing 1 in 8 of all deaths from cancer, according to the International Agency of Research on Cancer (Ferlay, Shin, Bray, Forman, Mathers, & Parkin, 2010). More than 150 000 women around the world die of breast cancer annually (Ferlay, Shin, Bray, Forman, Mathers, & Parkin, 2010). Only 1% of breast cancer cases occur in men (Gunderman, 2006).

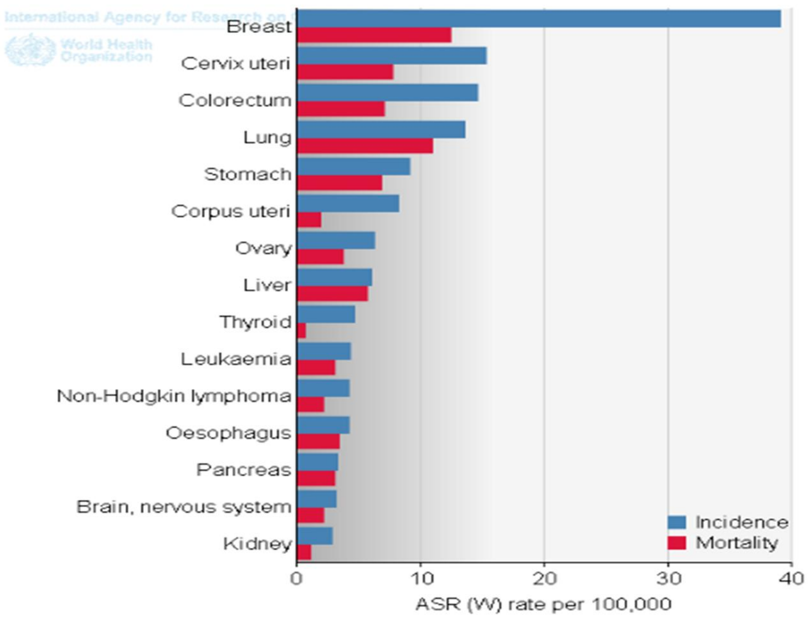

Figure 1.1 – Cancer incidence among women world population (from (Ferlay, Shin, Bray, Forman, Mathers, & Parkin, 2010)).

The survival rate and the disease prognosis differ greatly on the cancer stage. The treatment is more efficient when detected early, as the evolution into a more severe stage is avoided.

Breast cancer can be detected through imaging exams as mammography, ultrasonography, magnetic resonance imaging, where mammography is the most common exam. Mammography, as the other exams, aims to detect characteristic breast cancer lesions.

Computed aided detection intends to provide assistance to the mammography detection, reducing breast cancer misdiagnosis, and consequently allowing better treatment and prognosis.

1.1. Goals

This dissertation aims to analyze automatic enhancement and segmentation of microcalcifications in mammographic images. Hence, the specific objectives defined for this dissertation include:

- Research about the usual methodologies to process and analyze mammographic images;
- Development and implementation of image enhancement techniques;
- Evaluation of image enhancement techniques with emphasis on microcalcifications enhancement on real mammographic images;
- Development and implementation of image segmentation techniques;
- Evaluation of the mammographic microcalcifications segmentation techniques implemented on real mammographic images;
- Analysis about the effect of the image enhancement techniques on the results of the mammographic microcalcifications segmentation techniques.

The developed techniques have been implemented in MATLAB® and tested on real case studies from mini MIAS Database (Suckling, 1994).

1.2. Contributions

This dissertation aimed to provide and initial study about breast diseases, mammography. It provided also a review of mammographic image processing techniques enhancement and segmentation methods. Algorithms as adaptive neighborhood contrast enhancement and adaptive unsharp algorithm were implemented, whereas algorithms as homomorphic filtering were adapted.

An algorithm that detects the breast in mammograms was developed. Algorithm as adaptive threshold and morphological operator, threshold and difference of Gaussians were implemented and adapted, while some pre-processing techniques for region growing and active contour of selected areas were developed.

The enhancement and segmentation algorithms were evaluate in order to evidence the most robust, fast and flexible techniques suitable for mammographic images. The methods identified can be the basis for more efficient computer aided detection solutions

This dissertation also assessed the importance of image enhancement in the detection of lesions in mammographic images.

1.3. Overview

This thesis is organized according to the following chapters:

CHAPTER 2 – BREAST ANATOMY AND PATHOLOGIES: This chapter intends to explain the overall anatomy and physiology of the breast. Breast cancer, its imaging and other breast pathologies are analyzed in order to explain the differences between breast cancer and their imaging.

CHAPTER 3 – MAMMOGRAPHY AND COMPUTER AIDED DETECTION: In this chapter is given an explanation on the components and physics of the usual equipment of mammography. This chapter also defines computer aided detections and provides its advantages and classification. The history of those systems is also introduced.

CHAPTER 4 – IMAGE PROCESSING AND ANALYSIS ON MAMMOGRAPHIC IMAGES: In this chapter, there is an explanation of the different algorithms of the various phases of image processing and analysis and their application in mammographic images.

CHAPTER 5 – IMPLEMENTATIONS, RESULTS AND DISCUSSION: This chapter presents the methodologies developed and implemented during this project, and includes the experimental results and their evaluation.

CHAPTER 6 – CONCLUSIONS AND FUTURE PERSPECTIVES: In this chapter are presented the final conclusions of this dissertation, as well as some future perspectives concerning the implementation of an efficient algorithm of automatic analysis of mammographic images.

CHAPTER 2

BREAST ANATOMY AND PATHOLOGIES

This chapter aims to demonstrate the importance of the breast cancer study and to provide some fundamental knowledge on the breast structure and diseases. Thus, the anatomic structure of the breast is introduced, along with a description of the different types of breast cancer and some other diseases that affect the breast.

2.1. Breast Anatomy

In humans, the breasts are located in left and right sides of the upper ventral region of the trunk and each extends from the second rib above to the sixth rib below. The female breasts correspond to two large hemispherical eminences, which contain the mammary gland, Figure 2.1. This gland secretes milk, when stimulated, which usually corresponds to the period after giving birth. The mammary glands are sweat glands modified. They exist both in female and male, but in the former is only rudimentary, except in some peculiar circumstances (Gray, 2000), (Seeley, Stephens, & Tate, 2004).

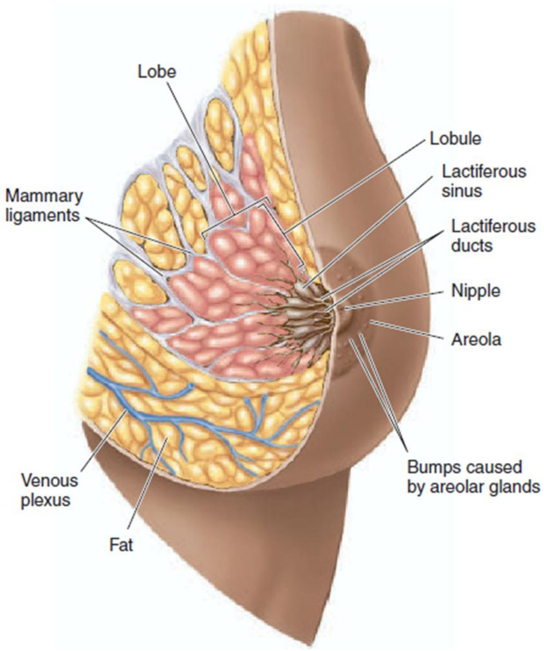

Figure 2.1 – Anatomy of the breast
(from (Seeley, Stephens, & Tate, 2004)).

The surface of the breast is convex and has, just below the center, a small conical prominence, called papilla or nipple. It is located about the level of the fourth intercostals space. The base of the papilla is surrounded by an areola (Gray, 2000), which has a slightly rough surface due to the presence of rudimentary mammary glands, areolar glands, just under the surface (Seeley, Stephens, & Tate, 2004).

The adult female breast consists of gland tissue, fibrous tissue, fatty tissue, blood vessels, nerves and ducts. The breast has numerous lobes, usually 15 to 20 (Seeley, Stephens, & Tate, 2004), which are composed of lobules. Those consist of alveoli and lactiferous ducts. These lactiferous ducts enlarge to form a small lactiferous sinus, which accumulates milk during lactation. The milk leaves the breast trough some holes in the nipple. The fibrous tissue lays at the entire surface of the breast and connects the lobes together. The fatty tissue covers the surface of the gland, except for the areola, and is located between the lobes. Usually, this tissue is abundant and determines the form and size of the gland (Gray, 2000), (Seeley, Stephens, & Tate, 2004).

The breast is hold in place as a result of the Cooper's ligaments support, which extends from fascia over the pectoralis major muscles to the skin over the mammary glands (Seeley, Stephens, & Tate, 2004).

The breast weight and dimension differ between individuals and at different periods of life (Gray, 2000), (Seeley, Stephens, & Tate, 2004). The female breasts start to develop at puberty, stimulated by the hormones estrogens and progesterone of the female sexual menstrual cycle. Higher glands development occurs during pregnancy, when the estrogens levels rise as they are secreted by the placenta and increase even more after delivery, when they are secreting milk to feed the baby. The breasts become atrophied in old age (Gray, 2000), (Guyton & Hall, 2000), (Seeley, Stephens, & Tate, 2004).

A children breast consists principally of ducts with dispersed alveoli, being similar in both female and male. A teenage breast mostly consists on fibrous and gland tissue. When adult, the fat substitutes some of the fibrous and gland tissue. During menopause, the breast is mainly adipose tissue.

The breast is intensely influenced by some hormones. Estrogens stimulate the breast adipose deposition and the growth of the mammary glands, as well as the initial development of lobules and alveoli of the breast. Progesterone and prolactin cause the final growth, are responsible for the function of these structures, and cause the external appearance of the mature female breast (Guyton & Hall, 2000).

During pregnancy, the concentration of estrogens and progesterone increases. This phenomenon causes expansion and branching of the breast gland ducts and deposition of additional adipose tissue. Prolactin is responsible for the milk production (Gunderman, 2006), (Seeley, Stephens, & Tate, 2004).

2.2. Breast Cancer

The breast can be affected by many pathologies. Nevertheless, the imagiology of the breast is almost completely addressed to the breast cancer (Gunderman, 2006).

As the other cancers, breast cancer corresponds to a malignant growth, which, in this case, begins in the cells of breast tissues. In normal situations, the cell division cycle is controlled and ordered, allowing tissue formation, growth and regeneration. When the control fails and there is no reparation of the eventual mutations, a tumor formation occurs.

After its formation, the evolution depends on the patient. However, an early detection and treatment is essential to stop the cancer evolution and to minimize the damages. The breast cancer, as the majority of other cancers, can have the ability to spread to other tissues, metastasizing, allowing the dissemination of cancer. When the breast cancer is premature detected, this phenomenon is avoided, which provides a better prognosis for the patient.

The breast cancer risk is increased with the age, where the majority of patients are over 50 years (Gunderman, 2006). Other risk factors correspond to family history of breast cancer, previous breast cancer, early menarche, late menopause, obesity, null parity and chest radiation exposure, abnormal cells in fibrocystic disease and hormone replacement therapy (Gunderman, 2006), (Seeley, Stephens, & Tate, 2004).

Due to these risks, some countries developed screening programs, where women over 40 or with higher risk of developing breast cancer perform mammographic exams in a periodic interval.

2.2.1. Breast cancer lesions

Breast cancer has some characteristic lesions such as microcalcifications, masses, architectural distortions. Asymmetry between breasts can also be a breast cancer indicator.

Microcalcifications are small size lesions, typically in the range 0.05 to 1 mm. With these dimensions, microcalcifications are relatively difficult to detect. They are bright and have various sizes, shapes and distributions and in some cases low contrast due to a reduced intensity difference between the suspicious areas and the surroundings. Another reason to their difficult detection is the proximity to the surrounding tissues. In dense tissues, suspicious areas are almost invisible as a result of the tissue superimposition. Some anatomic structures such as fibrous strands, breast borders or hypertrophied lobules are similar to microcalcifications in the mammographic image (Sankar & Thomas, 2010).

There is a high correlation between the presence of microcalcifications and breast cancer, particularly when the microcalcifications appear in clusters. Therefore, an accurate detection of microcalcifications is essential to an early detection of the majority of breast cancers (Li, Liu, & Lo, 1997). Generally, larger, round and oval shaped calcifications with uniform size have higher probability of being benign, while smaller, irregular, polymorphic and branching calcifications, with heterogeneous size and morphology have higher probability of being malignant (Arnau, 2007), Figure 2.2.

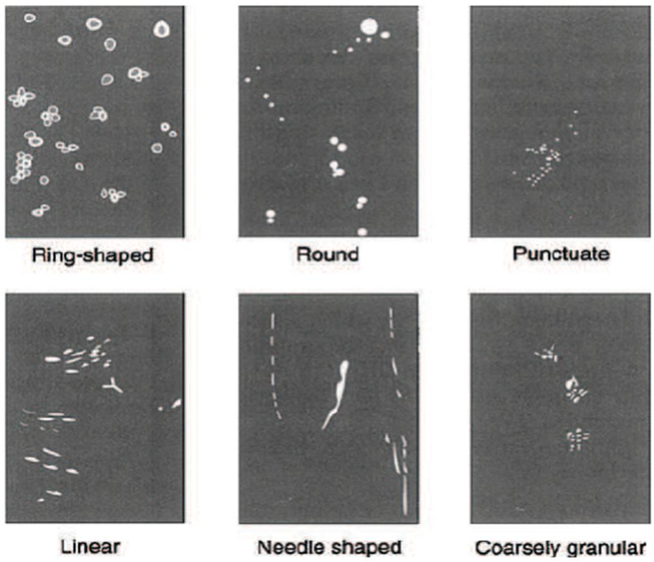

Figure 2.2 – Type of microcalcifications commonly seen on mammographic images (from (Gunderman, 2006)).

Masses appear as dense regions of different sizes and properties. They can be circular, oval, lobular or irregular/spiculated and their margins can be (Arnau, 2007), Figure 2.3 and Figure 2.4:

- circumscribed, which are well-defined and distinctly demarcated borders;
- obscured, which are hidden by superimposed or adjacent tissue;

- micro-lobulated, which have undulating circular borders;
- ill-defined, which are poorly defined scattered borders;
- spiculated, which are radiating thin lines.

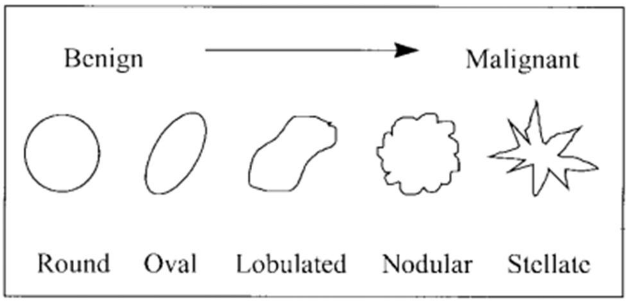

Figure 2.3 – Morphologic spectrum of mammographic masses (from (Bruce & Adhami, 1999)).

Depending on the morphology, the masses have different malignant probability. The ill-defined and spiculated borders have higher probability of malignancy (Arnau, 2007). A benign process is usually associated with the presence of circular or oval masses. However, the great variability of the mass appearance is an obstacle to a correct mammography analysis (Mini & Thomas, 2003). Some masses can incorporate microcalcifications, as in Figure 2.5.

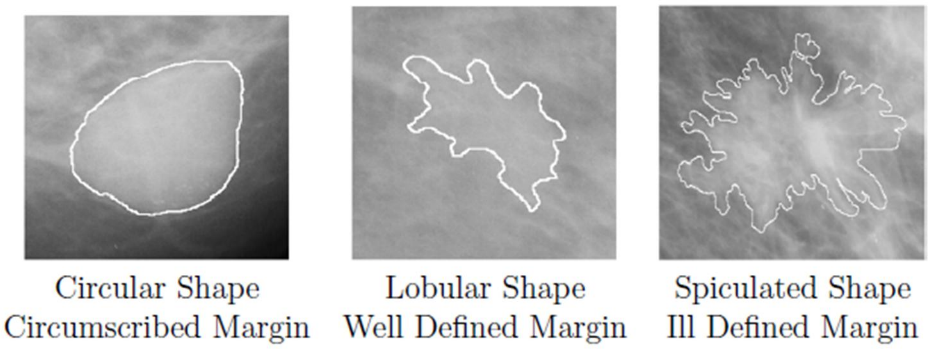

Figure 2.4 – Mass examples with different shapes and borders (from (Arnau, 2007)).

Architectural distortions refer to the derangement of the normal disposition of the parenchyma in a radiating or arbitrary pattern, without a visible center or mass. They are very variable and, consequently, very difficult to detect (Mini & Thomas, 2003).

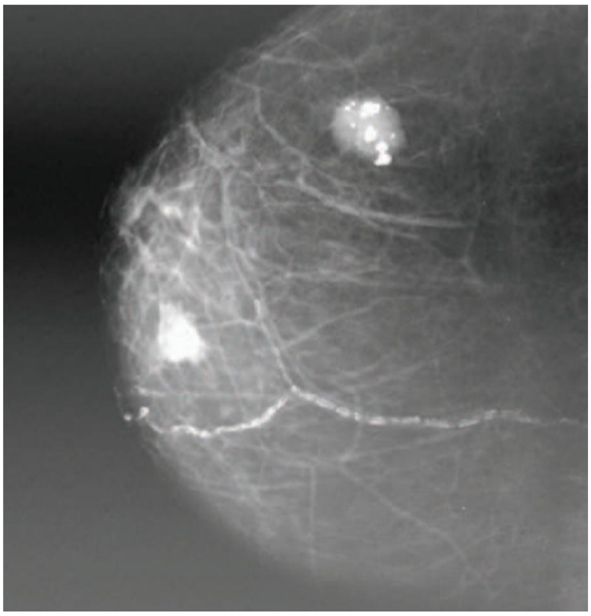

Figure 2.5 – A craniocaudal view of the right breast demonstrates benign vascular calcifications as well as two well-circumscribed masses containing “popcorn” calcifications classic for involuting fibroadenomas (from (Gunderman, 2006)).

2.2.2. Types of Breast Cancer

Breast cancer can be classified according to the breast tissue where the cancer was originated (glands, ducts, fat tissue or connective tissue) and according to the extent of the cancer spread (non-invasive/*in situ* or invasive/infiltrating) (Gunderman, 2006).

Carcinoma *in situ* tumor is an early form of carcinoma (invasive malignant tumor due to muted epithelial cells) detected in an early stage and with the absence of invasion of surrounding tissues. A cancer is known as infiltrating when the cells that started in the glands or ducts spread to healthy surrounding tissue. This type of cancer can have a variety of appearances (Eastman, Wald, & Crossin, 2006).

Both *in situ* and infiltrating cancers can be ductal and lobular, depending on the breast cancer location. Ductal carcinoma arises from the epithelial cells that line the breast milk ducts. In the ductal carcinoma *in situ*, cancer cells have not penetrated the basement membrane of the ducts. In the mammographic images is characterized by fine microcalcifications; however, the degree of cancer infiltration is not generally visible (Gunderman, 2006). The infiltrating ductal carcinoma is the most frequent type of breast cancer, being responsible for nearly 80% of cases. A tumor irregular mass is characteristic in the mammography of this type of cancer.

Lobular carcinoma begins in the milk glands, in the terminal lobules. Approximately, 10% of breast cancer is lobular carcinoma (Gunderman, 2006). The lobular carcinoma in situ is hardly detected in mammography.

Figure 2.6 – Invasive Ductal Carcinoma showing microlobulated borders and microcalcifications (from (Kaushak, 2007)).

When cancer spreads to other parts of the body through blood and lymph circulation, is called metastization.

When the ductal carcinoma invades the skin of the nipple is called Paget's disease.

Inflammatory breast cancer corresponds to an aggressive tumor that invaded the dermal lymphatics (Gunderman, 2006), representing about 1 to 4% of the breast cancer. This cancer usually presents breast inflammation.

Medullary breast carcinoma arises from the stromal cells of the breast (Gunderman, 2006). Mucinous carcinoma is associated with large amounts of cytoplasmic mucin (Gunderman, 2006). The last two types of cancer generally experience lower ability to create metastasis than the ductal and lobular.

2.3. Other breast pathologies

Some changes in the breast are not malignant. To analyze breast cancer lesions is necessary to regard some other similar lesions caused by different pathologies and benign processes in order to distinguish them.

Fibroadenoma is a benign tumor of the breast developed usually in young women, below 30 years old. This tumor remains in place for some time, but never progresses to a malignant cancer. It can grow rapidly due to the proliferation of the strome and epithelium cells. In mammography, is characterized as an oval mass with smooth borders, which may have some calcifications (Eastman, Wald, & Crossin, 2006).

A cyst is a closed structure which contains a distinct membrane and may contain air, fluid or semi-solid material. Generally, arises from dilated glandular ducts or lobules. In some rare cases cancer may occur inside the cyst, usually when the inside liquid contains some blood. Some cysts may contain calcium and develop calcification within the walls. Mammographically is a rounded mass with a well-defined contour (Eastman, Wald, & Crossin, 2006). After a breast injury with hematoma and fat tissue necrosis, oil cyst may occur, being physically similar to a simple cyst; however, with density equivalent to fat tissue (Eastman, Wald, & Crossin, 2006).

Mastitis is the inflammation of breast tissue due to an infection. In plasma cell mastitis, there are solid, dense, regular rodshape calcifications in the glandular ducts of the breast (Eastman, Wald, & Crossin, 2006).

Mammary dysplasia, also called fibrocystic disease or mastopathy, is a common condition due to excess of estrogen or higher tissue response to estrogens. It is characterized by three major conditions: formation of fluid filled cysts, breast duct system hyperplasia and fibrous connective tissue deposition (Eastman, Wald, & Crossin, 2006).

2.4. Breast Imaging Reporting and Data System

The breast imaging resulting of the image analysis can be classified in the level of suspicion of the possibility of breast cancer: breast imaging reporting and data system (BIRADS) score. There are seven categories (Eberl, Fox, Edge, Carter, & Mahoney, 2006):

- Category 0 – assessment incomplete. The mammogram (or ultrasound) did not provide enough information to a clear diagnosis. Another image exam is required.
- Category 1 – normal. There is an absence of abnormalities.
- Category 2 – benign or negative. There is evidence of benign masses.
- Category 3 – probably benign. The exams are probably normal, but a repeat mammogram should be completed in 6 months.

- Category 4 – possibly malignant. There are suspicious abnormalities. A biopsy is recommended to make a final diagnosis.
- Category 5 – malignant. There is indication of malignant lesions. A biopsy is recommended.
- Category 6 – malignant. This category indicates that a malignant diagnosis has already been done.

2.5. Summary

The breast cancer affects a large amount of people, particularly women. Additionally, this cancer is the most common reason of cancer death. However, when early detected, the possibilities of treatment are promising.

The breasts are composed of gland tissue, fibrous tissue, fat tissue, blood vessels, nerves and ducts. The percentage of these components varies with age and between women.

There are different lesions that are breast cancer characteristic such as microcalcifications, masses and architectural distortions.

Breast cancer can be classified according to the breast tissue where the cancer was originated, usually glands, ducts, fat tissue or connective tissue, and according to the extent of the cancer spread, where it can be non-invasive/*in situ* or invasive/infiltrating. These lesions have some variability, becoming of challenging detection. Some other diseases have patterns similar to the breast cancer, which difficult the diagnosis.

A breast imaging reporting and data system (BIRADS) score is, generally, used to classify the suspicion of breast cancer.

CHAPTER 3

MAMMOGRAPHY AND COMPUTER AIDED DETECTION

Mammography is the most commonly used technique to detect breast cancer at early stages, usually pre-symptomatic. When symptoms are developed, the cancer has typically become invasive, and consequently the prognosis is less favorable (Oliver, et al., 2010).

The techniques of computer aided detection aim to assist the radiologist detection to reduce missed breast lesion detection and consequently prevent the propagation of the cancer into a more severe stage.

3.1. Mammography

Currently, the mammogram is the most efficient system to detect clinically occult illness, being the only image-based method recommended for breast cancer screening (Chagas, Rodrigues, Tavares, Reis, Miranda, & Duarte, 2007). Mammography can greatly reduce the breast cancer mortality in a well-organized screening program over the population, being the breast cancer detection technique that most reduces mortality (Eastman, Wald, & Crossin, 2006). The performance of the mammography decreases as the density of the breast increases. This situation is inconvenient since breast cancer risk increases as the breast density increases (Oliver, et al., 2010).

3.1.1. Conventional Mammography Equipment

Mammography is a diagnosis exam that uses low-amplitude and high current X-rays to examine the human breast. X-ray is an electromagnetic radiation with high energy: wavelength in the range of 10^{-12} m and high frequency (10^{16} - 10^{19} Hz). These characteristics allow the penetration of objects and bodies (Bronzino, 2000), (Nersissian, 2004).

The main X-ray photons interactions with the tissue are photoelectric effect and Compton scattering (Akay, 2006), (Bronzino, 2000). The photoelectric effect occurs when an X-ray photon of short wavelength interacts with the electric field of an atom nucleus and ejects one of its inner electrons. The free electron becomes an ionizing particle (Lima, 1995). In Compton scattering, the X-ray photon interacts with an external electron and becomes free. The incident photon transfers energy to the scattering electron, which is ejected and becomes ionized. The photon changes direction (Lima, 1995). The photoelectric effect is the primary responsible for the radiologic image contrast, while Compton scattering is the primary mechanism for the image resolution limit.

Currently, mammography equipment has an X-ray tube which produces X-rays, Figure 3.1. This radiation crosses a metal filter and a collimator, which narrows the beam wave. The radiation is transmitted to the breast, which transmits a portion to an anti-scatter grid, passing to the image receptor. There, the photons interact and deposit their energy locally, allowing the image formation.

A fraction of X-rays passes through the receiver without interaction, reaching a sensor, which is used to activate the mechanism of automatic exposure control (Bronzino, 2000), (Webster, 2006).

The image formation will depend on the structures' densities when penetrated with the X-rays, as it absorption is dependent on the structures' densities. The image must have high spatial resolution to delineate the edges of structures of reduced dimension, as microcalcifications.

Usually, there are two standard image projections: craniocaudal (CC), which is a view from top, allowing a better imaging of the central and inner breast sectors; and mediolateral oblique (MLO), which is a lateral view from a certain angle, having an enhanced perspective of the glands (Arnau, 2007), Figure 3.2.

The structures of the conventional mammography are explained in detail below.

a) X-ray Source

X-rays used in mammography are originated by the electron bombardment of a hot vacuum tube (cathode) in a metal target (anode), usually molybdenum. The vacuum glass tube heats with the passage of electric current. Usually, this current is superior to 200 mA for short exposures of time (Webster, 2006). Electrons from X-ray tube acquire enough thermal energy to the leave the cathode (thermoelectric emission), being accelerated toward the anode. X-rays are produced through the de-excitation of the anode element. The resulting photons are transmitted in all directions, so it is necessary the existence of a collimator and filters to limit and direct the output of radiation. Generally, the X-ray tube uses a rotating anode. The cathode electrons reach this anode in a low angle (0º to 16º) of normal incidence (Akay, 2006), (Bronzino, 2000).

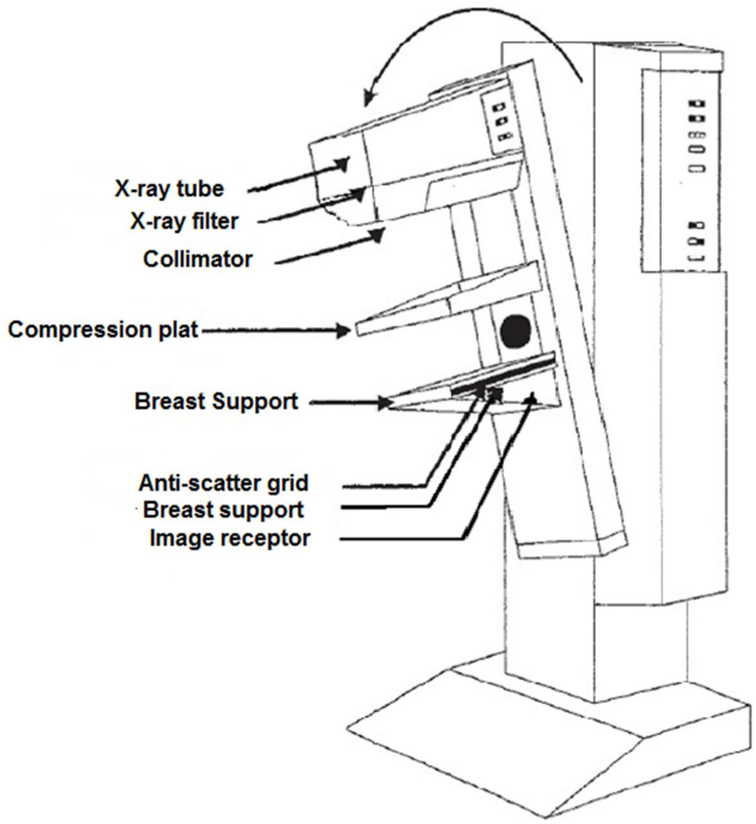

Figure 3.1 – Diagram of a common mammography equipment (adapted from (Bronzino, 2000)).

The actual focal point corresponds to the anode region involved in the production of X-rays. This region is determined by the width of the electron beam that reaches the anode and the inclination angle. The size of the focal point limits the resolution of the equipment. Small focal points create detailed images with better spatial resolution, allowing detection of microcalcifications, for example. Major focal points allow superior heat dissipation (Nersissian, 2004). The angle at which the X-rays hit the target also allows it, but it implies that the effective focal point varies across the image. In modern equipment, the typical size of the focal point for mammography normal contact is 0.3 mm while the small focal point mainly used for the magnification is 0.1 mm (Akay, 2006) (Bronzino, 2000).

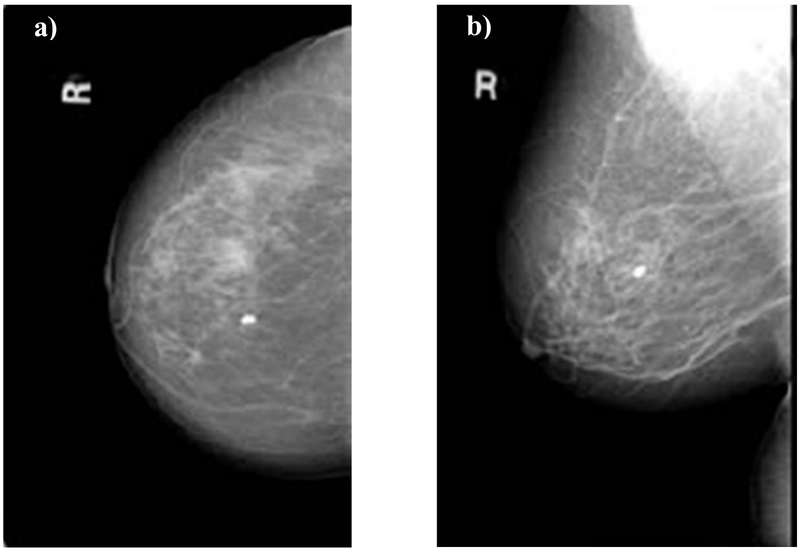

Figure 3.2 – Two distinct mammography projections: a) craniocaudal view, b) mediolateral oblique view (from (Arnau, 2007)).

b) X-ray Filter

X-ray filter, usually a molybdenum filter, is needed in order to filter the low energy photons, which creates image artifacts and photons of high energy (higher than 20 keV). This reduction allows the reduction of radiation transmitted to the breast and high contrast images (Haus & Yaffe, 2000).

c) Compression Unit

Breast compression allows: dispersion of the dissimilar breast tissues, minimizing the overlap of different breast plans; reduction of the absorbed radiation; breast immobility reducing noise and scattering of the X-rays in the film and homogenization of the radiation in the distinct tissues, minimizing the noise and improving the image contrast (Akay, 2006), (Bronzino, 2000).

d) Anti-scatter Grid

Anti-scatter grids are used to avoid an image contrast decrease produced by scattered radiation when reaches de image receptor. The scattered radiation is due to Compton scattering. Consequently, these grids only allow the passage of primary radiation to create the image. These grids are composed of thin slides made from a non-emitting X-ray material (Akay, 2006), (Bronzino, 2000), (Webster, 2006).

e) Image Receptor

The film-screen receptor is usually used as image receptor in the conventional mammography. X-rays get through the light-proof cassette and the film-screen and collide in a phosphor intensifier. The crystals absorb the phosphor energy and produce light with an isotropic distribution. The film emulsion is pressed against the screen, preventing dispersion of photons, which degrade the spatial resolution. The screen is usually treated with chemicals that absorb most of the light, allowing a more accurate image. Thus, the photons penetrate again the film, forming the image, as schematized in Figure 3.3 (Bronzino, 2000). Due to this type of image receptor, this mammography is commonly designed film-screen mammography (FSM).

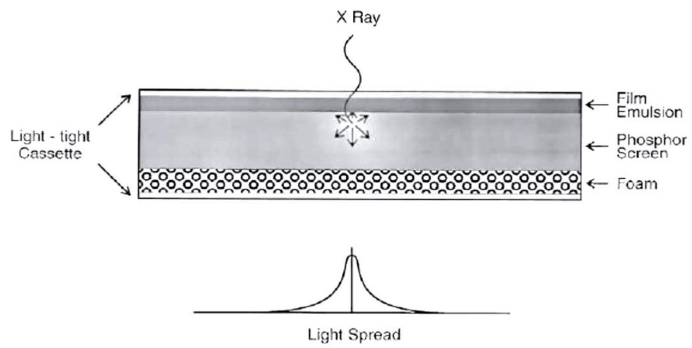

Figure 3.3 – A film-screen receptor (from (Bronzino, 2000)).

f) Automatic Exposure Control

Proper operations of automatic exposure control (AEC) are essential to obtain mammograms with good image resolution and adjusted amount of radiation. It controls the time of exposure for each examination using sensors adjusting the amount of radiation to the thickness of compressed breast (Akay, 2006), (Bronzino, 2000).

3.1.2. Noise and Radiation Dose

The noise in the mammogram has origin mainly in two sources: 1) X-ray detector random absorption and 2) granularity associated with the screen-film system. The first, known as quantum noise, depends on the amount of radiation that reaches the image receptor *per* unit area and on the attenuation coefficient of phosphorous material compared with the thickness of the screen. The granularity of the film increases the higher the speed of film used. Hence, there is a necessity to adjust the speed to maintain a high image quality (Bronzino, 2000).

In mammography, high image quality is essential because most of the relevant information of the mammogram corresponds to small details, such as microcalcifications, which can only be identified with a high spatial resolution image.

Although X-rays of low energy allow a better differentiation between tissues, there is a higher dose absorption by tissues and a greater exposure time. Hence, a balance between dose and image quality is necessary. The dose is dependent on several factors such as the speed of receptor-screen film, the existence of anti-scatter grid, the filtration of X-rays, to breast compression, density and composition of breast tissue, the applied current, processing the film and the magnification, i.e. the distance from the source to the image (Akay, 2006).

3.1.3. Full Field Digital Mammography

A full field digital mammography (FFDM) uses, essentially, the same equipment and physical principles as the conventional mammography equipment, but the image receptor is digital and the images are acquired digitally and send to a computer platform. This method can overcome disadvantages related with film-screen receptors such as poor image contrast and noise due to the granularity of the film emulsion.

With digital mammography, the magnification, orientation, brightness and contrast of the images can be adjusted after the exam to allow a better visualization of breast structures. Digital mammography can also make improvements related with more efficient image acquisition, since the detector is thin enough to absorb a large fraction of X-rays transmitted by the breast. The digital mammography may improve diagnostic capability and should outweigh the potential reduction in limiting spatial resolution (Akay, 2006).

In digital mammography, digital detectors have higher response to a linear increase of absorbed radiation dose than film-screen systems without saturation of high intensities. Thus, a more efficient absorption of the radiation beam incident occurs, as well as decreased intrinsic noise and higher spatial resolution (Akay, 2006), (Bronzino, 2000).

The image quality of mammography may be measured with the efficiency of the detector to convert the information from X-ray photons to a signal capable of producing an image. When compared to screen-film system, digital mammography has a higher efficiency for equal or even inferior radiation dose (Akay, 2006).

The acquisition system of digital mammography has advantages such as elimination of artifacts from signal processing, contrast enhancement, less time *per* patient and availability of images. There is the possibility to optimize each of the processes of image acquisition, such as display and storage, as those procedures are performed independently. However, there is higher equipment cost, there is the need to integrate the equipment in the system, and the images require much processing power from the computer and workstations (Evans, 2007).

Despite the digital mammography being quite promising, some improvements must be done in respect of having a high image resolution with lower cost.

3.2. Computer Aided Detection

Correct mammographic detection of asymptomatic lesions is essential to discover early breast cancer phases, increasing the treatment options and survival rate (Lee C. , 2002).

To properly detect mammogram lesions, radiologists may double read the exams as distinct readers miss different cancers (Blanks, Wallis, & Moss, 1998). However, less costly in man terms, would be the improvement of the performance of individual readers, as the double reading stops being required. In this process, software may be an important assistance (Astley, 2003).

Computer aided detection aims to improve the correct detection of abnormalities in the breast. Computed aided detection and computer aided diagnosis, commonly abbreviated as CAD and CADx respectively, can be defined as the detection and/or diagnosis made by the radiologist considering the results of a computed algorithm which characterize lesions through automatic image analysis (Masala G. , 2006), (Simonetti, Cossu, Montanaro, Caschili, & Giuliani, 1998). CAD systems are used to assist radiologists to locate the lesions, being a “second opinion”, rather than substitute the human diagnosis. This allows the reduction of variability in the radiologists’ mammograms interpretation and the frequency of errors by assuring that suspicious regions are revised and increasing the influence of subtle signs, which may be dismissed otherwise (Akay, 2006).

The use of CAD is supposed to follow the subsequent steps (Rangayyan, Ayres, & Desautels, 2007):

- Initial radiologist mammography reading, marking suspicious areas;
- A CAD system scanning to detect suspicious features;
- Radiologists' analysis of the prompts given by the CAD system and verification if the suspicious areas were left unchecked in the first reading.

3.2.1. CAD evaluation

The efficiency of a CAD system can be classified in four perspectives (Sampat, Markey, & Bovik, 2005):

1. True Positive (TP), when the suspected abnormality is, in fact, malignant;
2. True negative (TN), when there is no detection of abnormality in a healthy person;
3. False positive (FP), when occurs detection of abnormality in a healthy person;
4. False negative (FN), when there is no detection of a malignant lesion.

The last two classifications are critical situations. The false positive requires an invasive examination which implies patient anxiety, stress and unnecessary costs. The false negative is an even worse situation as it compromises the health of the patient and the disease treatment (Sampat, Markey, & Bovik, 2005), (Thangavel, Karnan, Sivakumar, & Mohideen, 2005).

The evaluation of mammography images is performed by expert radiologists, by histological examination, in the pathological cases and by three-year follow-ups in the negative results (Sampat, Markey, & Bovik, 2005), (Thangavel, Karnan, Sivakumar, & Mohideen, 2005).

The performance criteria are evaluated through sensitivity and specificity. The sensitivity is the fraction of the true positive cases over the real positive cases:

$$sensitivity = \frac{true\ positives}{true\ positives + false\ negatives}. \tag{3.1}$$

High values of sensitivity imply minimal false negative detection.

The specificity of the test is the fraction of the true negative cases over the real negative cases:

$$specificity = \frac{true\ negatives}{true\ negatives + false\ positives}. \quad \textbf{(3.2)}$$

High values of specificity imply minimal false positive detection.

There are other criteria that include those four perspectives, such as accuracy that is the measure of the global performance of the algorithm about the correct decisions; precision which corresponds to the fraction of relevant detections and F-measure, which corresponds to a harmonic mean of precision and sensitivity:

$$accuracy = \frac{true\ positives + true\ negatives}{true\ negatives + true\ positives + false\ positives + false\ negatives}, \quad \textbf{(3.3)}$$

$$precision = \frac{true\ positives}{true\ positives + false\ positives}, \quad \textbf{(3.4)}$$

$$F\ measure = 2\ \frac{precision \times sensitivity}{precision + sensitivity}. \quad \textbf{(3.5)}$$

Using sensitivity and specificity, the results are usually defined in terms of Receiver Operating Characteristic (ROC) curve, Figure 3.4, which corresponds to the tradeoff between the true-positive rate and the false-positive rate inherent in selecting specific thresholds on which predictions might be based (Thangavel, Karnan, Sivakumar, & Mohideen, 2005). ROC also shows the true positive fraction (sensitivity), as a function of the false positive fraction (FP fraction = 1-specificity) obtained varying the threshold level of the region of interest (ROI) selection procedure. Thus, the ROC curve produced allows the detection of massive lesions with predictable performance. The area over the ROC curve represents the error due to the use of the same test. The area under the curve represents the probability that, given a positive and a negative case, the classifier rule will be higher for the positive case, independently of the choice of the threshold decision. The overall performance is evaluated in terms of the area under the ROC curve and the relative errors (Sampat, Markey, & Bovik, 2005), (Thangavel, Karnan, Sivakumar, & Mohideen, 2005).

A perfect classifier would have a true positive rate of 1 (one) and a false positive rate of 0 (zero), for which the rule decision does not fail, as it has no false positive or false negative. Therefore, would have an area under the curve of one. As the ROC curve is arched towards this point, the better the decisional test. Random guessing would result in an area under the ROC curve of 0.5 (Sampat, Markey, & Bovik, 2005), (Thangavel, Karnan, Sivakumar, & Mohideen, 2005).

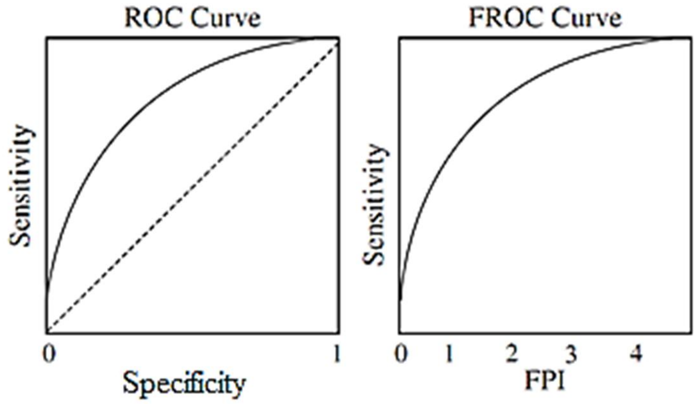

Figure 3.4 – Two plots illustrating receiver operating characteristics (ROC) and free-response receiver characteristics (FROC) curves. The dotted line in the ROC curve represents chance performance. ROC curves are used for diagnosis studies, and FROC curves are used for detection studies (adapted from (Sampat, Markey, & Bovik, 2005)).

To evaluate true-positive detection, sometimes is also required the localization of the tumor. A superior method for this case is Free-Response Receiver Operating Characteristic (FROC), which is a plot of sensitivity versus the false positive *per* image (FPI), Figure 3.4. It is typically used to report the performance of the detection algorithm (Sampat, Markey, & Bovik, 2005).

Both FROC and ROC analysis suffer from their limitations. Neither addresses the complexity of the input images and it is difficult to transform the subjective measurements (radiologists' observations) to the objective FROC curve (Thangavel, Karnan, Sivakumar, & Mohideen, 2005). ROC analysis has been more developed than FROC curves (Sampat, Markey, & Bovik, 2005).

3.2.2. CAD Benefits

The human detection of abnormalities in the mammography is often performed subconsciously, without a rule definition, which makes the computer-aided detection a challenging task (Masala G. , 2006).

The radiologist analysis of the mammography is fallible, increased by the repetitive and fatiguing task of detection abnormalities, poor image quality, subtlety of some abnormalities, occlusion of anatomical structures in the mammogram, low disease prevalence and breast structure complexity. These difficulties can be overcome by approaches such as double reading, which provides double perception and interpretation. Obviously, this procedure is too expensive, complex, and time consuming, particularly in screening programs with a high amount of mammographic images. The development of computerized systems as second readers represents an alternative (Mencattini, Salmeri, Rabottino, & Salicone, 2010).

According to Ciato et al. (2003) CAD had almost the same performance of simulated conventional double reading. However, Khoo, Taylor and Given-Wilson (2005) is indicated that CAD increases sensitivity of single reading by 1.3%, whereas double reading increases sensitivity by 8.2%.

The use of CAD increases the time taken for an individual reader to review the images. Still, this extra-time taken is not prohibitively slow in practice and the time taken is less than the one taken for double-reading situations (Astley, 2003).

Computers are consistent and indefatigable, and do not require years of practice to acquire the experience need to analyze mammographs (Simonetti, Cossu, Montanaro, Caschili, & Giuliani, 1998). Hence, the CAD systems are most helpful in those situations and in other circumstances such as screening mammography, when there is large volume of examinations with low disease incidence (up to 30% missed lesions); follow-up examinations, where lesion extraction and quantification are needed in order to measure it (Masala G. , 2006).

Consequently, 10 to 30% (Bird, Wallace, & Yankaskas, 1992) of cancers are not detected by radiologists due to misdiagnosis or misinterpretation, where about two/thirds of those are lesions that were evident *a posteriori* (Sampat, Markey, & Bovik, 2005), (Simonetti, Cossu, Montanaro, Caschili, & Giuliani, 1998).

Studies indicate that radiologists have false-negative rate diagnosis of 21%. CAD has potential to reduce this false-negative rate by 77% (Burhenne, et al., 2000). However, there is some controversy in the efficiency of CAD, when comparing with the radiologists' performance.

Cancers may also be ignored if the signs are subtle, being wrongly dismissed by the radiologist as being normal. In this case, a correct prompt would add weight to the lesion as abnormal, thus reducing the possibility of misclassification. Many of the very early cancers seen retrospectively show only subtle changes, but there is evidence that CAD systems are sensitive enough to prompt in such cases (Astley, 2003), (Burhenne, et al., 2000).

Additionally, from the masses referred to surgical biopsies only 10 to 20% are actually malignant (Simonetti, Cossu, Montanaro, Caschili, & Giuliani, 1998).

CAD has, in general, good performance detecting microcalcifications, which can be as high as 99% (Burhenne, et al., 2000), and detecting breast masses, which have been reported to 75 to 89% (Houssami, Given-Wilson, & Ciatto, 2009). Architectural distortion cannot be so accurately detected (Baker, Rosen, Lo, Gimenez, Walsh, & Soo, 2003).

According to Baker et al. (2003), where the sensitivity of two commercial CAD systems to architectural distortions was studied, fewer than one half of the cases were detected. Improvements still need to be done in order to increase the detection of this lesion.

The consequences of a benign lesion misdiagnosed as malignant is a biopsy which implies cost and psychological effects such as women anxiety, discomfort and stress. However, the cost and the consequences of a missed cancer are much higher than to a benign lesion misdiagnosed as malignant (Rangayyan, Ayres, & Desautels, 2007), (Schulz-Wendtland, Fuchsjäger, Wackerc, & Hermannd, 2009), (Simonetti, Cossu, Montanaro, Caschili, & Giuliani, 1998).

CAD needs image digitalization, in case of film-screen mammography, image analysis and characterization of the abnormalities (Simonetti, Cossu, Montanaro, Caschili, & Giuliani, 1998). The use of CAD with digital mammography has advantages when compared with screen-film mammography, which mammograms have to be digitized. Beyond time and money for digitalization, the image quality decreases with this system (Pisano & Yaffe, 2005). Thus, with digital mammography, CAD increases the detections (Akay, 2006). CAD false positive rates are higher for the digital system when compared with the screen-film system (Pisano & Yaffe, 2005).

Breast cancer CAD has commonly higher sensitivity and positive predictive value than radiologists. However, its false positives need to be reduced in order to increase even further the positive predictive value (Simonetti, Cossu, Montanaro, Caschili, & Giuliani, 1998).

As the radiologists makes the final decision, some of the CAD false prompts are easily dismissed when they are benign calcifications or image artefacts. However, the effect of false prompts high ratio will reduce the potential of CAD to overcome misclassification errors. False prompts may also degrade performance, as they act as distracters, drawing attention away from genuinely abnormal regions. Therefore, successful CAD requires algorithms that are both sensitive and specific (Astley, 2003).

According to Freer and Ulissey (2001) the number of cancers detected increased by 19.5% with the use of CAD, and the proportion of early-stage malignancies detected increased from 73 to 78%. The sensitivity rate increased from 6.5 to 7.7%, and the positive-predictive value of biopsy remained unchanged at 38%. Therefore, with this study was concluded that CAD can improve the detection of early-stage malignancies without an excessively adverse effect on the sensitivity rate or the positive-predictive value of biopsy. Another study, presented by Taplin, Rutter and Lehman (2006), indicated that CAD increased interpretive specificity but did not affect the sensitivity as unmarked visible non-calcified lesions were less likely to be assessed as abnormal by radiologists. Breast density did not affect CAD's performance.

However, improvements still need to be done in order to decrease to the minimal the failure of those systems as a consequence of the importance of the diagnosis, due to the large variability of the abnormal features and to the difficulty to detect lesions in dense breast tissues (Sampat, Markey, & Bovik, 2005).

The consequences of its failures can have serious implications. For these reasons, CAD detection has been quite challenging.

3.2.3. CAD History

The first paper dealing with computers identifying lesions at mammography was published in 1967 (Winsberg, Elkin, Macy, Bordaz, & Weymouth). It was based on bilateral comparison, which was recognized as useful in screening mammography with routine viewing of a large number of mostly normal examinations. The concept of computer diagnosis or automated diagnosis in radiology was established at that time (Doi, 2007). Although some interesting results were reported, these early attempts were not successful, because computers were not sufficiently powerful, digital images were not easily accessible and advanced image processing and analysis techniques were not available (Doi, 2007).

By 1980, improvements in Computer Vision techniques, mammographic quality and digitalization methods started to make clinical CAD possible (Masala G. , 2006), (Simonetti, Cossu, Montanaro, Caschili, & Giuliani, 1998). Before this, the concept was that computer would replace radiologists, giving the diagnosis, which was called automated computer diagnosis. Due to this notion, there was some criticism in the early phase to the implementation of computational software to aid diagnosis. By this time, the computer aided detection concept arises (Doi, 2007).

Considerably research has been done from that date on, mainly towards the computer aided diagnosis and the radiologists' acceptation to this technique started to increase. CAD was introduced in clinical practice in April 1995, at the University of Chicago, where routine screening mammograms are digitalized and analyzed for masses and calcifications by a clinical workstation (Simonetti, Cossu, Montanaro, Caschili, & Giuliani, 1998).

The United States Food and Drug Administration (FDA) approved the first CAD system in screening mammography in 1998. In 2001, only 130 CAD units were in clinical operation in the U.S. In 2005, this increased up to 1600 (Arnau, 2007), (Masala G. , 2006).

The first CAD approved by FDA was ImageChecker© of R2 Technology Inc (Hologic, 2010), which system detects potential microcalcifications clusters and masses. This system incorporates a digitizer to convert film mammograms to digital format, detection algorithms and prompts appear on suspicious abnormalities. It has suffered some improvements to strength the evidence and provides detailed examination of the suspicious regions, such as the presence of a threshold to establish whether or not a prompt is displayed. The threshold is set to achieve the optimum balance between sensitivity and specificity. The detection accuracy of calcifications was reported as 98.5% sensitivity at 0.74 false positives *per* case (set of four images). The detection accuracy of masses was reported as 85.7% at 1.32 false positive marks *per* case (Sampat, Markey, & Bovik, 2005), (Taylor, Champness, Reddy, Taylor, & Given-Wilson, 2003).

In 2002, two new mammographic CAD systems were approved: MammoReader™ from iCad (2009) and Second Look™ from CADx (2003). They have similar principle to the Image Checker©, but with different algorithms, and therefore responding differently to the potential lesions.

MammoReader™ was designed to detect primary signs of breast cancer in mammogram images, including microcalcification clusters, well and ill-defined masses, spiculated lesions, architectural distortions, and asymmetric densities. The reported overall sensitivity was 89.3% (91.0% in cases in which microcalcifications were the only sign of cancer and 87.4% in the remaining cases where malignant masses were present).

Second Look™ detects mainly microcalcifications and masses. The sensitivity of the system was reported to be 85% for screening detected cancers.

3.3. Summary

Mammography is important to detect early stages of breast cancer, as it detects asymptomatic lesions.

Conventional mammographic equipment has an X-ray tube, which produces X-rays, a metal filter to narrow the beam, an anti-scatter grid, a breast compressor and an image receptor. Additionally, an automatic exposure control is available to adjust the amount of radiation.

The image receptor in the conventional mammography is a screen-film system, while in the full-film digital mammography is a digital receptor. The digital mammography may improve diagnostic capability due to the potential to improve contrast resolution compared with film-screen imaging.

Computer aided diagnosis is a computational tool that radiologists can use, which aims to improve the correct detection of abnormalities in the breast. CAD results of a computational algorithm which characterizes lesions through automatic image analysis.

The CAD evaluation tools are based on their values of false positives and negatives and true positive and negatives, and thus on the sensitivity and specificity.

There is still some controversy in this area. However, there are some evidences indicating that this tool, when correctly used, improves the correct detection of microcalcification and masses and consequently the presence of a breast tumor. Some CAD systems have already been commercialized and approved by FDA. Nevertheless, some improvements still need to be done to decrease to the minimal the failure of those systems due to the large variability of the abnormalities and to the difficulty to detect lesions in dense breast tissues.

CHAPTER 4

IMAGE PROCESSING AND ANALYSIS ON MAMMOGRAPHIC IMAGES

The development of new breast cancer computer-aided detection is an active research field, particularly regarding the detection of subtle abnormalities in mammograms (Rangayyan, Ayres, & Desautels, 2007).

A typical computer aided mammography screening system is composed by several steps, as described in Figure 4.1. Regularly, the preprocessing block includes digitization of the mammograms with different sampling and quantization rates. Then, the regions of interests selected from the digitized mammogram are de-noised and enhanced. Enhancement and segmentation/detection of regions of interest are essential steps of any CAD software. Some regions have a high probability of lesion, thus, segmentation allows the reduction of the amount of data to process. Following the segmentation, feature extraction is important in order to characterize the objects. The features should have similar values for objects in the same categories and different ones for distinct categories in order to distinguish them. The last step of common CAD software corresponds to the classification based in the features (Cheng, Cai, Chen, Hu, & Lou, 2003), (Sampat, Markey, & Bovik, 2005).

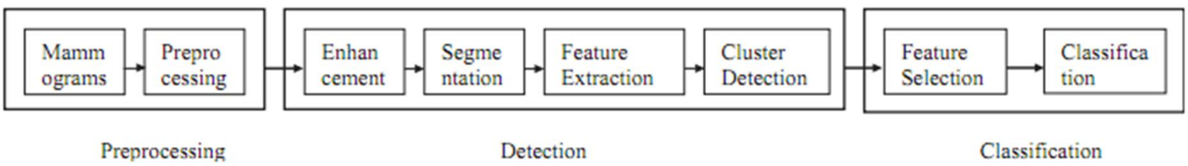

Figure 4.1 – Block diagram of a common CAD software (from (Cheng, Cai, Chen, Hu, & Lou, 2003)).

4.1. Enhancement of Breast Cancer Lesions

Despite the developments in the biomedical imaging techniques over the past years, some factors lead to the acquisition of images with less than the desired levels of contrast visibility of details (Rangayyan R. , 2005).

Mammography lesions, such as microcalcifications and masses, are usually small and have low contrast regarding to the contiguous breast tissues, so consequently these abnormalities are hard to detect. Image enhancement can improve the radiologists' perception to subtle diagnosis, and thus to more accurate diagnosis (Rangayyan, Ayres, & Desautels, 2007).

Some false positive rates are due to low contrast, noise in the image and reduced sharpness in features of interest caused by overlapping of structures (Sivaramakrishna, Obuchowski, Chilcote, Cardenosa, & Powell, 2000).

Image enhancement includes techniques such as contrast manipulation, reduction of noise and edges sharpening. The usual task of mammogram enhancement is to increase the contrast between regions of interest and background and to sharpen the edges or borders of the ROI (Cheng, Cai, Chen, Hu, & Lou, 2003).

However, some image enhancement techniques may distort diagnostic features appearance and shape, leading to misdiagnosis (Kimme-Smith, Gold, Bassett, Gormley, & Morioka). The major problem corresponds to the under-enhancement of some regions and over-enhancement of others. Under-enhancement can cause false negatives, and over-enhancement can cause false positives (Cheng, Cai, Chen, Hu, & Lou, 2003).

With the introduction of digital mammography, there is no need to digitalize film mammograms, which increases the dynamic range, signal to noise, and therefore reduced need of image enhancement (Rangayyan, Ayres, & Desautels, 2007).

In this section, some enhancement techniques are introduced, Figure 4.2.

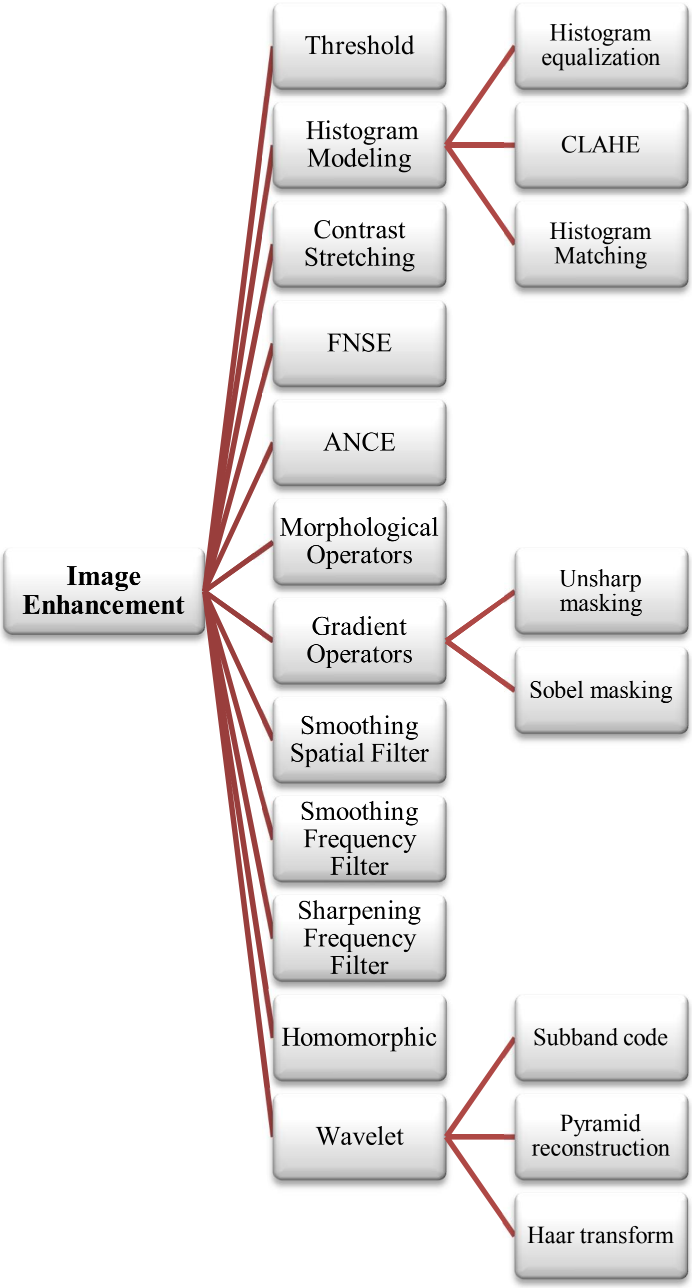

Figure 4.2 – Schematic classification of some image enhancement techniques.

4.1.1. Threshold

Image threshold is a basic and frequently used technique of image processing (Gonzalez & Woods, 2002).

If the gray levels of regions of interest of an image are distinguishable from the background, the image can be thresholded in order to obtain the selected features of interest, i.e., a specific value can be determined in order to distinguish features of interest from the background. If the values lower than threshold T_1 are considered as noise or feature without interest and those higher than T_1 are of interest, the output image can be defined as:

$$g(x,y) = \begin{cases} 0 & if\ f(x,y) \leq T_1 \\ f(x,y) & if\ f(x,y) \geq T_1 \end{cases}. \quad \textbf{(4.1)}$$

The resulting image includes the features of interest (Rangayyan R. , 2005).

Threshold can also be implemented associated with other techniques and also be implemented in the frequency domain.

Threshold is primarily used for image segmentation. In section 4.2.1, further explanations on this technique are given intending image segmentation.

4.1.2. Histogram Modeling

An image histogram represents the relative frequency of occurrence of different gray levels in the image. It corresponds to a discrete function $h\ (r_k) = n_k$, where r_k is the kth gray level and n_k is the number of pixels in the image having the gray level r_k (Gonzalez & Woods, 2002).

Histogram modeling modifies the original histogram into a shape as the image gets enhanced. As an example, when the histogram is narrow, it is useful to stretch the low contrast levels.

a) Histogram equalization

This technique corresponds to the redistribution of the gray levels in order to obtain a histogram as uniform as possible, maximizing the mammogram information (Cheng, Cai, Chen, Hu, & Lou, 2003), (Rangayyan, Ayres, & Desautels, 2007).

In histogram equalization every pixel is replaced by the integral of the histogram of the image in that pixel (Baert, Reiser, Hricak, & Kanuth, 2010), (Sivaramakrishna, Obuchowski, Chilcote, Cardenosa, & Powell, 2000). Considering that variable r represents the gray levels of the image, in a continuous function the transformation resulting from histogram equalization, equation 4.2, produces a level s for each pixel with gray level r in the original image. It is assumed that $T(r)$ is single-valued and monotonically increasing (Gonzalez & Woods, 2002).

$$s = T(r) = \sum_{j=0}^{k} p_r(r_j) = \sum_{j=0}^{k} \frac{n_j}{n}\ ,\ k = 0, 1, 2, \ldots L, \qquad \textbf{(4.2)}$$

where *p(r)* corresponds to the probability of occurrence of gray level r_k in the image, which can be determined by the histogram of the image (Gonzalez & Woods, 2002), (Rangayyan R. , 2005). Thus, *T(r)* equalizes the histogram of the given image, having as result a uniform histogram.

Karssemeijer, N (1993) used this technique to rescale mammographic images in order to equalize image noise, which indicated significantly reduction of the variation of the sensitivity of local feature extraction.

b) Contrast Limited Adaptive Histogram Equalization

Contrast limited adaptive histogram equalization (CLAHE) was initially implemented by Pizer, F. et al. (1987) in medical images, having considerable success. In this technique, a local histogram is calculated and a different grayscale transform is computed at each image location, based on the neighborhood. In standard adaptive histogram equalization, there is a possibility of image over-enhancement as noise is enhancement. Nearly uniform regions in the image generate high peaks in the histogram, leading to large values in the final image as a result of integration. This problem can be corrected through the limitation of the amount of contrast enhancement at every pixel, which is achieved by clipping the original histogram to a limit (Sivaramakrishna, Obuchowski, Chilcote, Cardenosa, & Powell, 2000). The CLAHE procedure consists of obtaining a local histogram with the neighbors of every pixel, clip this histogram to the specified limit, modifying the histogram by redistributing pixels, as given by equation 4.2., and integrating the histogram up to the value of the pixel to obtain the final value (Sivaramakrishna, Obuchowski, Chilcote, Cardenosa, & Powell, 2000).

c) Histogram Matching

Histogram matching or histogram specification corresponds to the processing of the histogram of the image in order to be similar to a prespecified one (Rangayyan R. , 2005).

The initial step of in this technique corresponds to the calculation of the histogram of the entire image. Through equation 4.2 the gray levels of the original images, r_k, are mapped into corresponding levels s_k based on the histogram of the original image.

A transformation function G of the given histogram $p_z(z_i)$ is also computed (Gonzalez & Woods, 2002):

$$v_k = G(z_k) = \sum_{i=0}^{k} p_z(z_i) = s_k \quad , \quad k = 0, 1, 2, \dots, L-1, \tag{4.3}$$

$$z_k = G^{-1}(s_k) \quad , \quad k = 0, 1, 2, \dots, L-1. \tag{4.4}$$

The late equation 4.4 corresponds to an approximation of the desired levels of the image with that histogram. G^{-1} has to be single valued and monotonic, which requires G to be strictly monotonic. z_k is then computed for each value of s_k (Gonzalez & Woods, 2002). For each pixel in the original image, if the pixel value is r_k, it is mapped to its corresponding level s_k. The final level z_k is obtained by the level inverse transformation function G^{-1} (Gonzalez & Woods, 2002).

The disadvantage of this technique is that the transformation must be designed for each image individually in order to have the wanted results (Morrow, Paranjape, Rangayyan, & Desautels, 1992).

4.1.3. Contrast Stretching

Contrast stretching, also called normalization, aims to improve the image through stretching the range of intensity values. Those intensity values are rescaled, usually through the analysis of the image histogram. Generally, contrast stretching is employed when the gray-level distribution is narrow due to poor illumination, lack of dynamic range in the imaging sensor or others (Yang, 2006). This technique aims to adjust the histogram to achieve a higher separation between the foreground and the background gray-level distribution. However, it is difficult to remove noise whose gray-level are similar to the objects' ones, such as the microcalcification (Cheng, Cai, Chen, Hu, & Lou, 2003), (Thangavel, Karnan, Sivakumar, & Mohideen, 2005).

A linear rescaling transformation associated is (Morrow, Paranjape, Rangayyan, & Desautels, 1992):

$$y = kx + m, \tag{4.5}$$

where x corresponds to the input gray scale image, y to the output values and k and m corresponds to non-zero transformation parameters. The variation of the values of k and m allows increased or decreased contrast (Morrow, Paranjape, Rangayyan, & Desautels, 1992). An example of this application is shown in Figure 4.3.

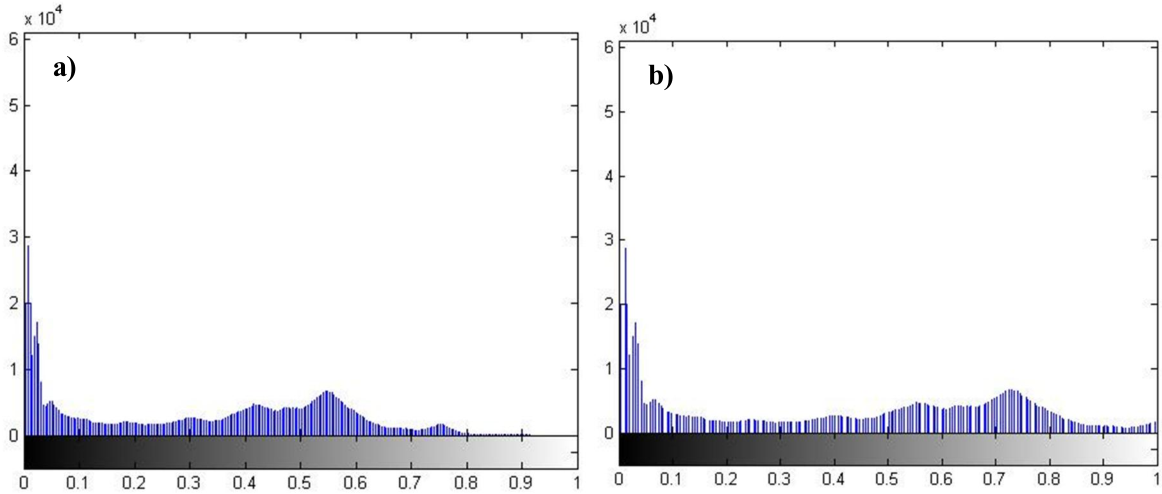

Figure 4.3 – Histogram of a mammographic image: a) before contrast stretching, and b) after linear contrast stretching.

Alternatively, a non-linear transformation is represented in equation 4.6, where k is a factor to rescale the output image to the range of the input image (Morrow, Paranjape, Rangayyan, & Desautels, 1992):

$$y = kx^p. \tag{4.6}$$

Other typical transformation is (Jähne, 2005):

$$f = \begin{cases} \alpha\, x, & 0 \le x < a \\ \beta(x-a) + \upsilon_a, & a \le x < b, \\ \gamma(x-b) + \upsilon_b, & b \le x < L \end{cases} \tag{4.7}$$

where L corresponds to the maximum gray value of the original image, the parameters a and b can be obtained through the analysis of the image histogram and the slopes α, β and γ are usually chosen greater than unity in the region of the stretch (Jähne, 2005).

This technique can remove the uniform background, but requires optimal transformation for each image (Cheng, Cai, Chen, Hu, & Lou, 2003), (Morrow, Paranjape, Rangayyan, & Desautels, 1992).

Yang (2006) proposed a modified contrast stretching algorithm, in which the image low-frequency information is processed by the conventional approach and the high-frequency information is processed by the log transformation. Thus, the details of the radiographic image are more enhanced when compared to the traditional algorithm.

4.1.4. Fixed-Neighborhood Statistical Enhancement

This technique, as opposed to the previous ones, is a local-based enhancement approach. For mammograms with no homogeneous background, these techniques may have improved performance. Fixed-Neighborhood Statistical Enhancement (FNSE) uses statistical properties in a pixel neighborhood to estimate the background and suppress it. Hence, it is possible to increase the contrast locally (Thangavel, Karnan, Sivakumar, & Mohideen, 2005).

For example, Narendra and Fitch (1981) use the global mean, M, local mean, μ, and local standard deviation, σ, to obtain the gray level transformation:

$$y = \alpha \frac{M}{\sigma} (x - \mu) + \mu, \qquad 0<\alpha<1 \tag{4.8}$$

where α is an empirically determined scaling factor. The determination of the local neighborhood dimensions is the critical step. However, a given neighborhood size and shape may not be equally effective in enhancing all areas of an image.

4.1.5. Adaptive Neighborhood Contrast Enhancement Technique

This technique, unlike the previous ones, adapts the size of the neighborhood to the local properties. Mammograms have ROI with some image features, which can vary widely in size and shape. With adaptive neighborhood, the details can be enhanced, without changing the remaining image and without significantly introducing artifacts (Thangavel, Karnan, Sivakumar, & Mohideen, 2005).

The adaptive neighborhood contrast enhancement (ANCE) algorithm has several steps. This technique is an automatic segmentation method which starts with the pixel to be processed, the seed. The nearest neighbors to the seed, usually 4-connected or 8-connected, are checked to verify if their gray level values are within a specified deviation from the seed gray level. The ones which meet the criterion are labeled as foreground, and the neighbors of those are checked to verify their inclusion. The algorithm stops when the foreground is surrounded by pixels that do not meet the criterion of inclusion, which are called background (Rangayyan, et al., 1997).

Region-based method can enhance more anatomical detail without significantly introducing artifacts and can identify calcifications more effectively in images of dense breasts where the contrast between calcifications and breast tissue is quite low (Cheng, Cai, Chen, Hu, & Lou, 2003).

The contrast value of each region can be calculated as:

$$C = \frac{f-b}{f+b}, \tag{4.9}$$

where f and b are the mean gray-level values of the foreground and background, respectively (Sivaramakrishna, Obuchowski, Chilcote, Cardenosa, & Powell, 2000).

Contrast can be increased by changing f or b. Replacing C with an increased contrast C', the new value of seed pixel in the contrast enhanced image is obtained (Rangayyan, Ayres, & Desautels, 2007):

$$f' = b\,\frac{1+C'}{1-C'}, \tag{4.10}$$

where f' is the new foreground value. The new contrast C' for the region can be calculated using an analytic function of C or an empirically determined relationship between C' and C, such as square root, exponential, and logarithm or even an empirically formed plot (Morrow, Paranjape, Rangayyan, & Desautels, 1992).

Morrow et al. (1992) developed this methodology in mammography images, using an empirically formed plot in order to correlate C and C'. More anatomical details were visible when compared with other enhancement techniques and no significant artifacts were introduced. Thus, the study concluded region-based methods can improve the visibility of microcalcifications clusters and some anatomic details.

Rangayyan et al. (1997) analyzed the effectiveness of this method, having a resultant increasing in the true positive cases. However, false positive cases were also increased.

4.1.6. Morphological Operators

The morphological base operator's correspond to erosion and dilation, which are inverse operators of each other. These operators decrease or increase the size of objects in binary images, respectively, being controlled by a structuring element (Gonzalez & Woods, 2002).

Erosion can be performed to eliminate irrelevant details, which are smaller than the structuring elements. The erosion of an object A by the structural element B corresponds to the mathematical expression:

$$A \ominus B = \left\{z | \left(\hat{B}\right)_Z \cap A^C \neq \emptyset\right\}, \quad \textbf{(4.11)}$$

where $\emptyset$ is the empty set. The erosion of A by B is the set of all the structuring elements' origin locations where the translated B has no overlap with the background of A (Gonzalez & Woods, 2002).

Dilation increase objects by the size of the structural element. The dilation of an object A by the structural element B corresponds mathematically to:

$$A \oplus B = \left\{z | \left(\hat{B}\right)_Z \cap A \neq \emptyset\right\}. \quad \textbf{(4.12)}$$

Hence, dilation of A by B is the set consisting of all the structuring element origin locations where the reflected and translated B overlaps at least some portions of A (Gonzalez & Woods, 2002).

Frequently, those operators are combined. The erosion of an object A by a structuring element B, followed by the dilation of the result by the same structuring element corresponds to an image opening:

$$A \circ B = (A \ominus B) \oplus B. \quad \textbf{(4.13)}$$

Image opening removes regions of an object that are smaller than the structuring element, smooth the edges of the objects and disrupts narrow connections.

The dilation of an object A, followed by the erosion by the same structuring element corresponds to an image closing:

$$A \cdot B = (A \oplus B) \ominus B. \quad \textbf{(4.14)}$$

Morphological closing smooths the object edges, joins narrow breaks, and fills holes smaller than the structural element.

4.1.7. Gradient Operators

Some usual gradient operators are unsharp masks and Sobel gradient (Thangavel, Karnan, Sivakumar, & Mohideen, 2005).

Gradient operators require the use of two masks: one to obtain the x-direction gradient and the second to obtain the y-direction gradient. The results are combined to obtain the orthogonal components of the vector quantity whose magnitude represents the strength of the gradient or edge at a point in the image and whose angle represents the gradient angle (Daponte & Fox, 1988).

a) Unsharp masking

A well-known convolution mask is the unsharp mask. When an image is blurred by some unknown phenomenon, each pixel is composed of its own true value plus the fractional components of its neighbors. This technique uses this concept to reduce the blur and improve the image through the reduction of low frequency information and amplification of high frequency detail (Cheng, Cai, Chen, Hu, & Lou, 2003).

The image resultant from the unsharp masking can be obtained by subtracting a low-pass filtered image (f_{lpf}) from the input image (f_{in}), which corresponds to a high-pass filtered image (f_{hpf}). This high-pass filtered image is weighted, $C(x,y)$, and added to the input image, equation 4.15 (Bae, Shamdasani, Managuli, & Kim, 2003). This operation allows the amplification of the details due to the high-pass filter, as reduces low-frequency information and amplifies high frequency details (Bae, Shamdasani, Managuli, & Kim, 2003), (Morrow, Paranjape, Rangayyan, & Desautels, 1992).

$$\begin{aligned} \boldsymbol{f_{out}(x,y)} &= \boldsymbol{f_{in}(x,y) + C(x,y)\left[f_{in}(x,y) - f_{lpf}(x,y)\right]} \\ &= \boldsymbol{f_{in}(x,y) + C(x,y) f_{hpf}(x,y)} \end{aligned} \quad \textbf{(4.15)}$$

In the case of standard unsharp filter, the weight of the high-pass filters is the same value to the entire image. When it adapts to the neighborhood of the pixels, corresponds to an adaptive unsharp filter (Ji, Sundareshan, & Roehrig, 1994).

An example of adaptive unsharp enhancement is represented in Figure 4.4.

It should be noted, that this process can changes dramatically the input image (Cheng, Cai, Chen, Hu, & Lou, 2003).

A study presented by Dhawan, Buelloni and Gordon (1986) used an optimal adaptive enhancement method and was able to emphasize the features in the image with little enhancement of the noise.

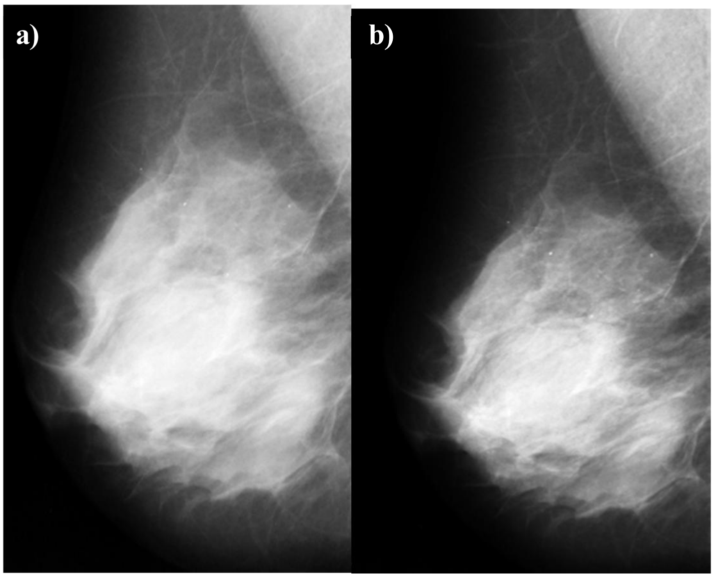

Figure 4.4 – Example of enhancement of mammography with unsharp masking: a) original image and b) image filtered using an adaptive unsharp filter.

Kim, Park, Song and Park (1997) developed an adaptive image enhancement method for mammographic images, based on the first derivative and the local statistics. This method has three steps, where the first one is to remove the artifacts that can be misread as microcalcifications. The second step is the computation of gradient images using first derivative operator, and the last step is the enhancement of important features of the mammogram adding adaptively weighted gradient images. Additionally, local statistics of the image are used for adaptive enhancement, enabling image details enhancement and noise suppression.

b) Sobel Operator

Daponte and Fox (1988) used Sobel gradient operators to enhance chest radiographs. However, these procedures change the appearance of the image too radically to be applicable in mammograms, where details in the image are essential for diagnosis.

The Sobel operator uses two kernels, $S_x i$ and $S_y i$, in the x and y direction, which are sequentially convolved with the original image matrix, similar to these ones:

$$S_x 1 = \begin{matrix} -1 & 0 & 1 \\ -2 & 0 & 2 \\ -1 & 0 & 1 \end{matrix} \; and \; S_y 1 = \begin{matrix} -1 & -2 & -1 \\ 0 & 0 & 0 \\ 1 & 2 & 1 \end{matrix} . \qquad \textbf{(4.16)}$$

The result is stored in the center or circled pixel and can be represented as a vector quantity with magnitude:

$$|y(mp,nq)| = |x(mp,nq) * S_x i| + |x(mp,nq) * S_y i|, \tag{4.17}$$

and angle:

$$arg\ [y(mp,nq)] = \arctan\left[\frac{x(mp,nq)*S_y}{x(mp,nq)*S_x}\right], \tag{4.18}$$

where *x(mp,np)* represents the original image, * represents the two-dimensional convolution and i and j are unit vectors in the x and y directions, respectively (Daponte & Fox, 1988).

4.1.8. Smoothing Spatial Filtering

Smoothing filters are used for noise reduction and blurring in order to remove small details from an image prior to large object extraction (Gonzalez & Woods, 2002).

However, this filter is not appropriated to identify breast lesions, and specifically microcalcifications, as they correspond to small details in the image, usually with sharp transitions. Nevertheless, they can be used combined with other enhanced methods.

a) Linear smooth filtering

A smooth linear filtering, also called average filter, corresponds to the average of the pixels contained in the neighborhood of the filter mask, and so to remove random noise from the image. The replacement of the value of every pixel in the image by the average of the gray level in the neighborhood results in reduced sharp transitions. This allows random noise removal, but also allows the blur of edges, both characterized by sharp transitions (Gonzalez & Woods, 2002).

The average filtering can also be weighted, when pixels are multiplied by different coefficients. Thus, some pixels have more weight than others as an effort to reduce the blur (Gonzalez & Woods, 2002).

b) Non-linear smooth filtering

Order-statistics filters are nonlinear spatial filters that are characterized by ranking the image pixels and then replacing the value of the center pixel with the value determined by the ranking result. Such methodology can be performed with median filters, which replace the value of a pixel by the median of the neighbors' gray level. They provide noise reduction with less blurring than linear smoothing filters of similar neighborhood size. This technique is performed by sorting the values of the pixel being analyzed and its neighbors determine their median and set that value for the analyzed pixel (Gonzalez & Woods, 2002).

4.1.9. Smoothing frequency filtering

Spatial frequency refers to the frequency of the variations in tone that appear in an image. Edges as well as other sharp transitions, such as noise, correspond to high frequency contents. The attenuation of these components can be achieved in the frequency domains in the image transform. The basic model for frequency domain corresponds to:

$$G(u,v) = H(u,v)\, F(u,v), \qquad \textbf{(4.19)}$$

where *F(u,v)* is the Fourier transform of the image and *H(u,v)* is the filter function. This filter attenuates the high frequency components of the image. As previously mentioned, these filters are not appropriated for mammogram enhancement, but can be used associated with other filtering (Gonzalez & Woods, 2002).

a) Gaussian filter

The Gaussian filtering of an image is given by:

$$H(u,v) = e^{-D^2(u,v)/2\sigma^2}, \qquad \textbf{(4.20)}$$

where *D(u,v)* is the distance of the limit frequency desired to remove, cut-off frequency, from the origin of the Fourier transform, and σ is a measure of the spread of the Gaussian function.

D(u,y) can be calculated with the information of the image size *M* x *N*:

$$D(u,v) = \left[\left(u - \frac{M}{2}\right)^2 + \left(v - \frac{N}{2}\right)^2\right]^{1/2}. \qquad \textbf{(4.21)}$$

This filter is then used to enhance the image, according to equation 4.19, and does not cuts as ideally pretended the high frequencies at the cut-off frequency, rather attenuates them. It can also intensify the low frequencies components while attenuates the high frequency ones.

An example of a Gaussian filtering is demonstrated in Figure 4.5 in the spatial domain and in the frequency domain (Gonzalez & Woods, 2002).

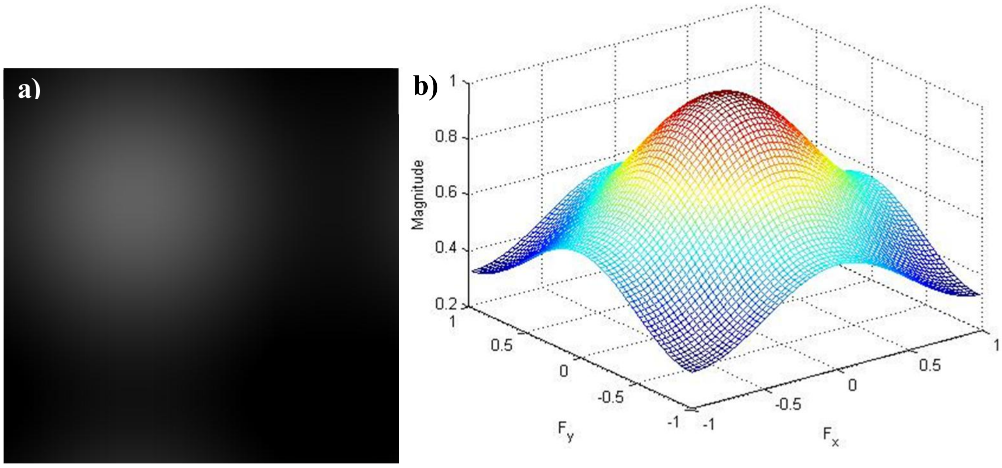

Figure 4.5 – Perspective plot of a Gaussian low-pass filter displayed:
a) in the spatial domain and b) in the frequency domain.

Tiu, Joen and Hsieh (2008) applied discrete wavelet transform and difference of Gaussian filter to enhance mammograms.

In (Band-pass Filtering Vs. Multiscale Dyadic Wavelet Transform for Contrast Enhancement of Digital Mammograms, 2005), a technique was presented where the mammogram is filtered using a Gaussian band-pass filter to enhance the structure of the breast while suppressing the noise and the slowly varying high density structure.

b) Butterworth Low-pass filter

Butterworth low-pass filter has the parameter order of filtering. For high order values, the Butterworth filter approaches the ideal low-pass filtering, which eliminates the high frequency components higher than the cut-off frequency. The transfer function of a Butterworth filter of order *n* is:

$$H(u,v) = \frac{1}{1+\left[\frac{D(u,v)}{D_O}\right]^{2n}}, \tag{4.22}$$

where $D(u,v)$ can be calculated through equation 4.21 and D_0 corresponds to the cut-off frequency (Gonzalez & Woods, 2002).

4.1.10. Sharpening frequency filtering

As previously mentioned, high frequency components are related to edges, noise and small objects. Image sharpening can be implemented in the frequency domain with a high-pass filter, which attenuates the low frequency components, as the opposite of the low-pass filtering. Thus, it attenuates the objects and the background which does not have sharp characteristics while enhances the edges and small objects. It also enhances the random noise associated to the image (Gonzalez & Woods, 2002).

The intended function of filters is the reverse operation of the low-pass filtering, thus the transfer function of the high-pass filters is:

$$H_{hp}\ (u,v) = 1 - H_{lp}(u,v), \tag{4.23}$$

where $H_{lp}(u,v)$ is the transfer function of the low-pass filter (Gonzalez & Woods, 2002).

4.1.11. Homomorphic Filter

An image can be expressed as a product of the amount of source illumination incident on the scene being viewed, which is called illumination, $i(x,y)$, and the amount of illumination reflected by the objects in the scene, which is called reflectance, $r(x,y)$, (Gonzalez & Woods, 2002):

$$f(x,y) = i(x,y)r(x,y), \tag{4.24}$$

The homomorphic filter key point is the separation of those two image components which can be done approximately in the frequency domain. High frequency components of the Fourier transform of the logarithm of the image are a rough approximation of the reflectance, while low-frequency components are rough approximations of the illumination. Those components are then operated separately. This requires the use of a filter function, $H(u,v)$, that affects differently those components. Usually this filter tends to decrease the contribution of the illumination, which is more associated to the noise of the image, and amplify the contribution of the reflectance. The result is dynamic range compression and contrast enhancement (Gonzalez & Woods, 2002).

Yoon and Ro (2002) used this technique to enhance the contrast of mammographic images, having improvement of the contrast in breast tumor images.

4.1.12. Wavelet

Wavelet transform is based on small waves of variable frequency and limited duration, which are denominate wavelets (Gonzalez & Woods, 2002). The advancement of wavelet theory enabled the application of image contrast enhancement, with promising results (Laine, Fan, & Yang, Wavelets for Contrast Enhancement of Digital Mammography, 1995).

A wavelet decomposition of an image divides the input image into several subbands containing features at different scales. The advantage is that small features like microcalcifications are dominant in one subband, whereas larger features like masses prevail in a different subband (Sivaramakrishna, Obuchowski, Chilcote, Cardenosa, & Powell, 2000).

Wavelets have been employed in mammographic image analysis.

Strickland et al. (1996) proposed a discrete wavelet transform with four dyadic and two additional interpolating scales to enhance microcalcifications, as these lesions provides spatial frequency features in mammograms. Individual microcalcifications were greatly enhanced allowing straightforward thresholding in order to segment them.

Laine et al. (1994) applied a wavelet-based enhancement methodology to accomplish mammographic feature analysis, utilizing redundant transformation and linear/nonlinear mapping functions with Laplacian or gradient wavelet coefficients.

Laine et al. (1995) implemented also other technique, using unsharp masking with a Gaussian low-pass filter included in a dyadic wavelet framework for mammography enhancement. Those multiresolution representations provided an adaptive mechanism for the local emphasis of features of importance to mammography.

a) Subband Coding

In the dyadic wavelet enhancement algorithm, a given image, *I,* is decomposed into a set of subbands through some analysis filters, *F*, being posteriorly reconstructed using synthesis filters, *G* (Gonzalez & Woods, 2002), (Sivaramakrishna, Obuchowski, Chilcote, Cardenosa, & Powell, 2000).

An L-level M-dimension decomposition and reconstruction of I is given by:

$$I = W_{LO}^{-1}[I_O^L] + \sum_{i=1}^{L}\sum_{j=1}^{M} W_{ij}^{-1}[I_j^L], \qquad \textbf{(4.25)}$$

where W denotes filtering I by F into subband images I_{ij}, whereas W^{-1} denotes filtering I_{ij} by G. The subband images I_{ij} can be separately enhanced before the reconstruction process (Sivaramakrishna, Obuchowski, Chilcote, Cardenosa, & Powell, 2000).

Sivaramakrishna, Obuchowski, Chikcote, Cardenosa & Powell (2000) used multiscale adaptive gain procedure to enhance each subband image, where the pixels with very low amplitude were suppressed and the ones higher of a certain threshold were enhanced, according to:

$$f(y) = a\left[sigm\big(c(y-b)\big) - sigm\big(-c(y+b)\big)\right], \qquad \textbf{(4.26)}$$

where:

$$a = \frac{1}{sigm(c(1-b)) - sigm(-c(1+b))}, \qquad \textbf{(4.27)}$$

with *0<b<1* and *sigm(y)* defined by:

$$sigm(y) = \frac{1}{a + e^{-y}}, \qquad \textbf{(4.28)}$$

where b and c control the threshold and rate of enhancement, respectively. The values were chosen as $b = 0.2$ and $c = 20$.

Laine, Schuler, Fan and Huda (1994) used this wavelet methodology to enhance mammographic images, with the purpose of masses detection. Their result indicated that wavelet enhancement was superior to algorithms of unsharp masking and adaptive histogram equalization.

b) Pyramid Reconstruction

Another multiresolution structure for representing images is an image pyramid. It corresponds to a collection of decreasing resolution images arranged in the shape of pyramid. The base of the pyramid contains a high resolution representation of the image, while the apex contains a low resolution (Gonzalez & Woods, 2002), Figure 4.6.

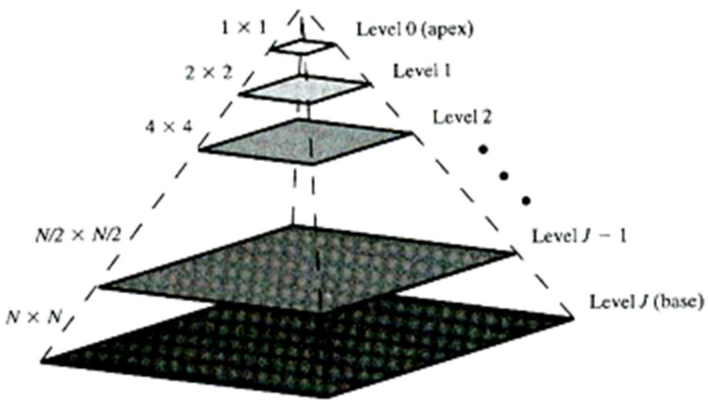

Figure 4.6 – Pyramidal Image Structure (from (Gonzalez & Woods, 2002)).

The base level of the image pyramid, which is denominated level J, has a size equal to $2^J x 2^J$, where $J=log_2N$ in a NxN image. The other levels, j levels with $0 \leq j<J$, have a size of $2^j x 2^j$. If the pyramid is fully built, it is composed of $J+1$ resolution levels; but most pyramids are truncated at P level, discarding the pyramid apex till the $J-(P+1)$ level. Each level in the pyramid is computed by filtering the input (averaging, low Gaussian filtering or no filtering) and down sampling the filtered result by a factor of 2. The quality of the approximation is dependent on the filter selected (Gonzalez & Woods, 2002).

The approximation is up sampled again with a factor of 2 in order to have the same resolution as the input image. The image resultant, prediction image, is then filtered. This filter is critical for the accuracy of the prediction image. The difference between the prediction image and the approximation is computed, which corresponds to the level j prediction residual, which is used to reconstruct progressively the original image (Gonzalez & Woods, 2002).

Li, Liu and Lo (1997) implemented this technique to enhance microcalcifications in digital mammograms. They reconstructed specific information, in this case, microcalcifications, by selecting specific sub images in a high frequency region and ignoring the sub images which represent the low-frequency background.

c) Haar Transform

A third image operation corresponds to the Haar Transform (Gonzalez & Woods, 2002). This transform (*T*) is separable and symmetric, and can be represented as:

$$T = HFH, \tag{4.29}$$

where F is a NxN matrix and H is a NxN transformation matrix, which contains the Haar basis functions, $h_k(z)$.To generate H, k which is an integer value, is defined as

$$k = 2^p + q - 1, \qquad 0 \leq \mathrm{p} \leq \mathrm{n} - 1 \tag{4.30}$$

where q=0 or q=1for p=0 and $1 \leq q \leq 2^p$ for $p \neq 0$. Thus the basic functions are:

$$h_0(z) = \frac{1}{\sqrt{N}}, \qquad z \in [0,1] \tag{4.31}$$

and

$$h_k(z) = h_k(z) = \frac{1}{\sqrt{N}} \begin{cases} 2^{p}/_{2} & \frac{q-1}{2^p} \leq z < \frac{q-0.5}{2^p} \\ -2^{p}/_{2} & \frac{q-1}{2^p} \leq z < \frac{q}{2^p} \\ 0 & otherwise, z \in [0,1] \end{cases} . \quad \textbf{(4.32)}$$

4.1.13. Enhancement Evaluation

There are different techniques to evaluate the enhancement of mammographic images. Some works use distinct mathematical parameters in order to perform the evaluation such as contrast, contrast improvement index (CII), background noise level (BNL), peak signal to noise ratio (PSNR), and the average signal to noise ratio (ASNR). Li, Liu and Lo (1997) used all those parameters in order to evaluate regions of interest containing microcalcifications in mammographic images.

The contrast of an object, as defined in (Morrow, Paranjape, Rangayyan, & Desautels, 1992), is given by equation 4.9. This parameter is a commonly used to evaluate image enhancement (Laine, Schuler, Fan, & Huda, 1994), (Laine, Fan, & Yang, 1995), (Li, Liu, & Lo, 1997), (Morrow, Paranjape, Rangayyan, & Desautels, 1992).

Contrast improvement index (Li, Liu, & Lo, 1997), (Laine, Schuler, Fan, & Huda, 1994), (Laine, Fan, & Yang, 1995), corresponds to a quantitative measure defined by the ratio of the contrast of the region of interest after enhancement ($C_{processed}$) and in the original image ($C_{original}$):

$$\boldsymbol{CII} = \frac{\boldsymbol{C_{processed}}}{\boldsymbol{C_{original}}} . \quad \textbf{(4.33)}$$

The background noise level (Li, Liu, & Lo, 1997) can be defined by:

$$BNL = \sqrt{\frac{1}{N}\sum_{i=1}^{N}(b_i - b)^2}, \quad \textbf{(4.34)}$$

where b_i is the gray-level value of each pixel, b to the mean background gray-level, and N is the total number of pixels in the surrounding background region.

Parameters that include the information of the background noise correspond to peak signal to noise ratio and average signal to noise ratio. Those parameters are important because the contrast does not include information about background noise variation, thus if the background has large variety and high noise level, the evaluation using contrast is unsuitable. As the study of microcalcifications includes variable background, as the breast tissue is not constant, the study of those two variables is also important (Li, Liu, & Lo, 1997).

PSNR can be defined as:

$$PSNR = \frac{p-b}{BNL}, \quad \textbf{(4.35)}$$

and ASNR can be defined as:

$$ASNR = \frac{f-b}{BNL}, \quad \textbf{(4.36)}$$

where p corresponds to the maximum gray level of the foreground, b to the mean background gray level, f to the mean foreground gray level (Li, Liu, & Lo, 1997).

4.2. Segmentation and Detection of Breast Cancer Lesions

Segmentation is the division of the input image into non-overlapping regions. Usually, it corresponds to the extraction of objects from the background. The segmentation can be done in order to obtain locations of suspicious areas to assist radiologists for diagnosis or to classify the abnormalities as benign or malignant (Cheng, Cai, Chen, Hu, & Lou, 2003).

A physician carefully scans the entire image and searches for features that could be associated with disease, usually concentrating on the region of suspected abnormality and examines its characteristics to decide if the region exhibits signs related to a particular disease. An automatic image analysis process has approximately the same steps (Rangayyan R. , 2005).

Segmentation is one of the most difficult tasks in image processing, and its accuracy is determinant to the success of any CAD system (Gonzalez & Woods, 2002). Segmentation algorithms are usually based on one of two properties of intensity value, which are discontinuity, based on abrupt changes in the image, as edges, and similarity, based on the partition of the image into regions according to some similarity criteria (Gonzalez & Woods, 2002).

Thus, depending on the nature of the images and the regions of interest, the segmentation methods can attempt to detect the edges of the ROIs, grow regions to approximate the ROIs, threshold if they are already distinguished from the background, between other methods. However, in some cases, a ROI may be composed of several disjoint component areas, for example, a tumor that has metastasized into neighboring regions and calcifications in a cluster. Edges that are detected may include disconnected parts that may have to be matched and joined (Rangayyan R. , 2005). Image segmentation can be divided in several according to a schematic classification, as represented in Figure 4.7.

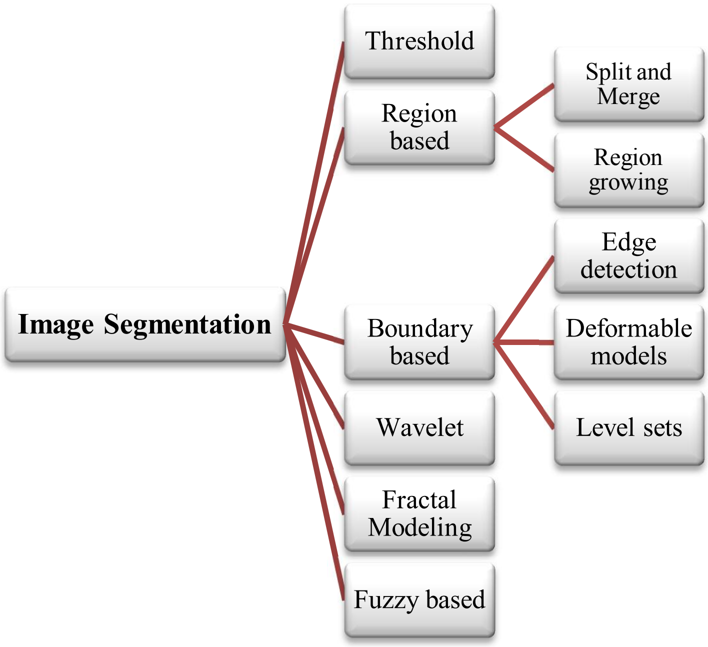

Figure 4.7 – Schematic classification of some image segmentation techniques.

4.2.1. Threshold

Threshold is one of the most basic image segmentation method (Gonzalez & Woods, 2002). From a grayscale image, threshold is generally used to create binary images.

An obvious method to separate bright objects, usually from the dark background, when the histogram has two dominant gray level modes, is selecting a threshold T which separates those modes. In this process, the different pixels are compared with a limit value, the threshold. If they are greater, they are assumed to belong to the foreground and if lower, they are assumed to belong to the background. In this case, the region of interest is assumed to be brighter than the background. However, different variants can be applied, e.g. a pixel can be labeled as foreground only if it is between two threshold values. Generally, the foreground pixels are set with the value of 1 (one), while the background pixels are set with the value 0 (zero) (Gonzalez & Woods, 2002), (Shapiro & Stockman, 2002):

$$\begin{cases} f(x,y) = 1 & if\ f(x,y) > T \\ f(x,y) = 0 & if\ f(x,y) < T \end{cases}. \qquad \textbf{(4.37)}$$

Multilevel threshold is necessary to introduce when the histogram has more than two dominant modes. In this case, an object is located in $T_1<f(x,y)<T_2$ and another object is at $f(x,y)>T_2$. The determination of the threshold values can be done with several different techniques. In this multilevel threshold approach, a usual method is the region growing technique (Gonzalez & Woods, 2002).

The threshold value corresponds to a critic parameter in this approach, which can be determined through several techniques, usually local statistics such as histograms, means and standard deviations. However, the histogram is not frequently bimodal due to the variations in shapes, sizes and intensities of microcalcifications; hence it is difficult to choose an adequate threshold (Cheng, Cai, Chen, Hu, & Lou, 2003).

There are other different statistical approaches, such as the one described by Karssemeijer and Brake (1996) that is based on statistical analysis of a map of pixel orientations. An important feature of the method is that the way in which an orientation of the image intensity map is determined at each pixel. If an increase of pixels pointing to a region is found, this region is marked as suspicious, especially if such an increase occurs in many directions. Around 90% of the malignant cases were detected at rate of one false positive *per* image.

There are several techniques of automatic threshold. Gonzalez et al.(2002) describes one automatic procedure which starts with the segmentation of the image with an estimate threshold T_0. This produces a group of pixels G_1 with gray levels inferior to T, and a group of pixels G_2 with gray levels higher than T. The average of the gray level of both groups is computed: μ_1 and μ_2, respectively for G_1 and G_2. A new threshold value is calculated as:

$$T = \frac{\mu_1 + \mu_2}{2}. \qquad \textbf{(4.38)}$$

The procedure is repeated iteratively until the difference between T_0 and T is inferior to a predefined value.

Another automatic threshold technique is the Otsu's method, whose procedure uses only the zero and the first cumulative moments of the gray level histogram of the image. The technique starts with the computation of the histogram and consequently of the probabilities of each intensity level. Dividing the pixels into two classes by a threshold, each class has a certain probability of occurrence, ω_0 and ω_1, a mean level μ_0 and μ_1 and a variance σ_0^2 and σ_1^2. Those parameters correspond to the zero and first order cumulative moments of the histograms, respectively. In order to evaluate the threshold chosen, some criteria are used to measure the class separability:

$$\begin{cases} \lambda = \frac{\sigma_B^2}{\sigma_W^2} \\ \kappa = \frac{\sigma_T^2}{\sigma_W^2}, \\ \eta = \frac{\sigma_B^2}{\sigma_T^2} \end{cases} \quad \textbf{(4.39)}$$

where:

$$\sigma_W^2 = \omega_0\sigma_0^2 + \omega_1\sigma_1^2, \quad \textbf{(4.40)}$$

$$\sigma_B^2 = \omega_0\omega_1(\mu_1 - \mu_0)^2(\mu_1 - \mu_0)^2, \quad \textbf{(4.41)}$$

$$\sigma_T^2 = \sum_{i=1}^{L}(i - \mu_T)^2\, p_i \sum_{i=1}^{L}(i - \mu_T)^2\, p_i, \quad \textbf{(4.42)}$$

and σ_W^2 corresponds to the intra-class variance, σ_B^2 corresponds to the between class variance, σ_T^2 is the total variance of gray levels, μ_T is the total mean of the global picture, p_i is the probability distribution of the different gray levels, and L the number of levels. The problem is then the maximization of the criterion objects given by equation 4.39, which requires the minimization of intra-class variance. Thus several thresholds are computed in order to meet this criterion.

Threshold can depend only on the gray level values which is denominated global threshold, can depend also on some local and on the spatial coordinates of each pixel, which is called dynamic or adaptive threshold.

In adaptive thresholding, the threshold is based on an expected bimodal intensity distribution in a selected size window that contains the sub-image to be segmented. The original image is divided into square sub-images. Each sub-image is overlapped by four other sub-images. The level histograms of the sub-images are smoothed by a median filter in order to remove local maxima and minima. Then, the resulting histogram is classified as either bimodal, if there is a valley at the histogram, or unimodal. Once all sub-images have been processed, each unimodal threshold is replaced by a value interpolated from neighboring sub-images (Cheng, Cai, Chen, Hu, & Lou, 2003).

Cheng, Lui and Freimanis (1998) used a threshold technique to segment microcalcifications, as the areas which containing microcalcifications are usually inhomogeneous and those variances are larger than those of tissue background regions. Thus, they used a threshold T to separate the microcalcifications from the breast tissues according to non-uniformity, using the local variance (σ^2) occurrence function:

$$h(q) = \sum_{q=0}^{V} \delta\left(\sigma_{xy}^2 - q\right), \quad \textbf{(4.43)}$$

$$\delta(t) = \begin{cases} 1 & if\ t = 0 \\ 0 & otherwise \end{cases}, \quad \textbf{(4.44)}$$

and determined by the minimum error thresholding criterion:

$$J(T) = \min_T \sum_g h(g) \cdot \varepsilon(g, T), \quad \textbf{(4.45)}$$

where T is the optimum threshold, *h(q)* the local variance occurrence function and $\varepsilon(g, T)$ is the Bayes Classifier.

4.2.2. Region based image processing

Region-based processing, which can also be denominated pixel-independent processing, adaptive neighborhood processing or object-oriented processing, is based on the knowledge that neighbor pixels in a region have similar values.

Region growing can be performed in two perspectives: image segmentation and then segment processing or overlapping regions for each pixel and process each of these regions independently. Usually, overlapping regions are employed to avoid noticeable edge artifacts (Morrow, Paranjape, Rangayyan, & Desautels, 1992).

Image processing procedures can then be applied on an image feature basis, rather than pixel by pixel (Morrow, Paranjape, Rangayyan, & Desautels, 1992).

a) Region Growing

A region based segmentation method is the region growing. The neighborhood pixels of a seed point are examined and the pixels with similar properties are grouped. Two variables need to be specified: the window size and the absolute difference in gray levels between the processed pixel and the seed pixel (Cheng, Cai, Chen, Hu, & Lou, 2003). If the average intensity of the grown region respects similarity criteria, the pixel is classified as a pixel of the microcalcification. Every pixel in the image is chosen successively as the seed pixel, repeating the overall process (Cheng, Cai, Chen, Hu, & Lou, 2003).

Alternatively, multiplicative tolerance level region growing, the similarity criterion is based on a relative difference:

$$\frac{f(m,n) - \mu_{R_c}}{\mu_{R_c}} \leq T, \qquad \textbf{(4.46)}$$

or

$$2\,\frac{|f(m,n) - \mu_{R_c}|}{f(m,n) + \mu_{R_c}} \leq T, \qquad \textbf{(4.47)}$$

where *f(m, n)* is the gray level of the pixel being analyzed and μ_{Rc} is the original seed pixel value or the mean gray level. The multiplicative tolerance level determines the maximum gray level deviation allowed within a region (Rangayyan R. , 2005).

Adaptive thresholding and region growing methods were compared by Kallergi et al. (1992), which indicated that adaptive thresholding is more stable, but more dependent on parameter selection.

Bankman et al. (1997) reported the use of a region-growing based algorithm for the segmentation of calcifications that do not require threshold or window selection. This method was compared to the multi-tolerance region-growing and to the active contour model, and the results indicated they have similar statistic performance, but the one developed is faster and does not require so computational effort.

b) Region Split and Merge

This method is similar to the region growing procedure: the image is subdivided into a set of regions, but the regions are merged and/or split in order to satisfy the *P* conditions of segmentation (Gonzalez & Woods, 2002).

The image is successively divided into smaller quadrant regions such that if *P(quadrant)=FALSE*, the quadrant is subdivided in subquadrants. This procedure is continued until no further changes are made, or a stop criterion is reached. The splitting technique may be represented as a quadtree, which is a tree whose nodes have four exactly descendants, Figure 4.8 (Rangayyan R. , 2005).

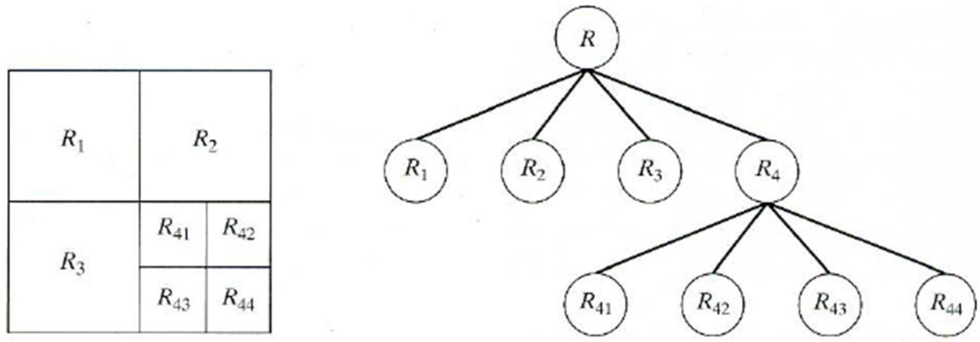

Figure 4.8 – Exemplification of region split and merge: a) partitioned image and b) corresponding quadtree (from (Gonzalez & Woods, 2002)).

Rangayyan et al. (1997) used a hand-selected region of interest containing a single mass to implement this technique in order to approximate its boundary using polygons.

4.2.3. Boundary based image processing

An edge is characterized by a quick change in the gray level in a particular direction, depending on the edge orientation. There are several techniques to segment objects related to edges such as edge detection, deformable models and level sets (Rangayyan R. , 2005).

a) Edge detection

Edge detection is a common segmentation method. It is based on the statement that usually pixel values change rapidly at the boundaries between regions. Many mathematical morphological operations such as erosion, opening and closing transformations can be used, and many operators were proposed, such as Roberts gradient, Sobel gradient and Prewitt gradient (Cheng, Cai, Chen, Hu, & Lou, 2003). One difficulty that can arise is the knowledge about the resolution of the mammogram that the morphological operation requires to determine the size and shape of the structure elements.

Edges, as previously mentioned, are characterized by quick changes in the gray level. Gradient operators measure the rate of change and so correspond to a basis for edge detection methods (Rangayyan R. , 2005).

The derivates in x and y-direction with reduced noise sensitivity incorporates averaging over multiple measurements:

$$f_y'(m,n) \approx 0.5\,[f(m+1,n) - f(m-1,n)]$$
$$f_x'(m,n) \approx 0.5\,[f(m,n+1) - f(m,n-1)]. \quad \textbf{(4.48)}$$

Some other operators are centered upon the pixel being analyzed. Prewitt operator is one of them, having a neighborhood of 3 pixels around the pixel in question. It has a vertical G_y and horizontal G_x derivatives (Rangayyan R. , 2005):

$$G_x = \begin{bmatrix} -1 & 0 & 1 \\ -1 & 0 & 1 \\ -1 & 0 & 1 \end{bmatrix}, \quad \textbf{(4.49)}$$

$$G_y = \begin{bmatrix} -1 & -1 & -1 \\ 0 & 0 & 0 \\ 1 & 1 & 1 \end{bmatrix}. \quad \textbf{(4.50)}$$

As a result of the Prewitt derivative size, equation 4.48, and to the scale factor in, the result of the Prewitt operator should be divided by 3x2xΔ, where Δ is the sampling interval in *x* and *y*. A vectorial form of gradient corresponds to:

$$G_f(m,n) = G_{fx}(m,n) + j\,G_{fy}(m,n), \quad \textbf{(4.51)}$$

where

$$G_{fx}(m,n) = (f * G_x(m,n)) \quad \textbf{(4.52)}$$

and

$$G_{fy}(m,n) = (f * G_y(m,n)). \quad \textbf{(4.53)}$$

The Sobel operators are similar to the Prewitt ones, but include higher weights for the pixels in the row or column of the pixel being processed:

$$G_x = \begin{bmatrix} -1 & 0 & 1 \\ -2 & 0 & 2 \\ -1 & 0 & 1 \end{bmatrix}, \quad \textbf{(4.54)}$$

$$G_y = \begin{bmatrix} -1 & -2 & -1 \\ 0 & 0 & 0 \\ 1 & 2 & 1 \end{bmatrix}. \quad \textbf{(4.55)}$$

Rotated versions of these operators can be used in order to detect diagonal edges (Rangayyan R. , 2005).

Roberts' operator (Rangayyan R. , 2005) uses a 2x2 neighborhood, with the upper-left element of the matrix is placed on the pixel in question. The operators are:

$$\begin{bmatrix} -1 & 0 \\ 0 & 1 \end{bmatrix} and \begin{bmatrix} 0 & -1 \\ 0 & 1 \end{bmatrix}. \quad \textbf{(4.56)}$$

Dengler, Behrens and Desaga (1993) presented a systematic method for the detection and segmentation of microcalcifications in mammograms. This technique applies a two stage algorithm to spot detection and shape extraction. The first step uses a weighted difference of Gaussian filter to the detection of spots noise invariant and size-specific. The second stage used a morphological filter to reproduce the shape of the spots.

b) Deformable Models

Active contours or "snakes" were introduced by Kass, Witkin and Terzopoulos (1988). This technique seeks for local minimum contours. Placing the contour near the desired image features, the snake essentially seeks for the points, taking a minimum energy measure of all possible points in the neighborhood. In general, the energy measure of a snake contains internal and external forces. The internal forces regulate the ability of the contour to stretch or bend at a specific point. The external forces attract the contour to specific image features.

Wirth and Stapinski (2004) explored the application of active contours to extract breast regions in mammograms. The method is based in the facts that breast-air interface is a very low gradient and may be obscured by noise and that uncompressed fat near the breast-air interface is a gradient, growing as the fat nears the center of the breast. Hence, this method includes noise removal to allow the snake to distinguish the breast contour and the noise. Snakes are designed to fill in gaps that occur in contours.

Right-to-left edge detection picks up the gradient of the breast as an edge when the breast is approaching from the left. As opposite, left-to-right edge detection does not identify the breast contour, but will pick up noise and other artifacts. A dual threshold would produce a difference in terms of the breast area detected. By taking this difference, it is possible to obtain an approximate location of the breast contour (Thangavel, Karnan, Sivakumar, & Mohideen, 2005).

There are several reasons why active contours are a good approach to breast region extraction. The principal is that the breast is a well-defined curve, hence is open to curve approximation characteristics of active contours. In addition, the background in most mammograms is a low intensity and low gradient region, which can be avoided by the active contour due to the search for a local minimum. However, it is necessary some pre-processing techniques to avoid situations such as medium intensity noise that may attract the active contour away from the breast region; the breast-air interface is typically a medium gradient, so energy functional based on edges needs preprocessing; the initial contour will have to be placed relatively close to the desired breast contour (Wirth & Stapinski, 2004).

Valverde, Guil and Muñoza (2004) presented an algorithm for the segmentation of vessels in mammograms. This technique is useful in order to eliminate vascular false positives during detection of microcalcifications in mammograms. However, the main problem corresponds to the high level of noise presence in mammograms. An initial theoretical analysis of edge detection is done to select the optimum edge detector and threshold value. Then, a local approach is performed, which corresponds to a segmentation process based on a snake with a new noise energy term to extract the vessel contour and remove particle noise that remained in the image.

c) Level-set methods

Level-set methods were introduced by Osher and Sethian (1988). These methods can also be seen as deformable models. The shape to be recovered is captured through the propagation of an interface represented by the zero level set of a smooth function (Gelas, Bernard, Friboulet, & Prost, 2007). Hence, the topological changes can be easily handled and the geometric properties of the contour can be implicitly calculated (Ma, Tavares, Jorge, & Mascarenhas, 2009). This approach is a numerical technique for computing and analyzing motion of interfaces, which may develop sharp corners, break apart, merge together and disappear due to significant topologic changes (Wang, Lim, Khoo, & Wang, 2007).

The evolution of the interface is determined by a time-dependent partial differential equation which corresponds to the Hamilton-Jacobi equation. The velocity terms reflect the image features, which characterizes the object to be segmented (Gelas, Bernard, Friboulet, & Prost, 2007). This method can be implemented in two different ways (Gelas, Bernard, Friboulet, & Prost, 2007): narrow-banding, where this method is only applied in narrow bands around the interface, having lower computational cost; reshaping, where the level-set function may develop steep or flat gradients due to the propagation, which yield inaccuracies in the numerical approximation.

This method has been commonly applied to structural shape and topology optimization problems (Wang, Lim, Khoo, & Wang, 2007).

4.2.4. Wavelet approaches

These techniques correspond to image filtering and analysis in the wavelet domain. They can be used to feature enhancement, segmentation and even classification. The mammograms can be examined in a low frequency level of the transform or in a high frequency in order to examine small structures, such as microcalcifications. Commonly, the wavelet transforms reconstructed the original image from transformed coefficients modified at each level by local and global nonlinear operators (Cheng, Cai, Chen, Hu, & Lou, 2003).

There are different approaches in the wavelet domain; some of them are here analyzed.

Multiresolution wavelet techniques can show in different levels distinct type of object. This allows the separation of small objects such as microcalcifications, which are included in one level, from large objects such as the background structures, which are included in a different level (Cheng, Cai, Chen, Hu, & Lou, 2003). The advantage of multistage wavelets is that they do not require a *priori* knowledge of the image or computation of local statistics inside the filter window.

Wavelet theory provides a powerful framework for multiresolution analysis, and it can be used for texture analysis. The discrete wavelet transform is used to map the regions of interest into a series of coefficients, constituting a multiscale representation of the ROIs. To obtain the features reflecting scale-dependent properties, a set of features can be extracted from each scale of the wavelet transform. The most frequently used features are energy, entropy, and norm of the coefficients (Thangavel, Karnan, Sivakumar, & Mohideen, 2005).

Strickland and Hahn (1996) proposed a two-stage method based on wavelet transforms for the detection and segmentation of microcalcifications. The detected spots, such as microcalcifications, are enhanced in the wavelet domain, before the computation of the inverse wavelet transform. A threshold procedure is done in order to segment the calcifications. A sensitivity of 91% was obtained.

Bruce and Adhami (1999) performed a multiresolution analysis, specifically the discrete wavelet transform modulus-maxima method to extract mammographic mass shape features. These shape features are used to classify masses as round, nodular, or stellate. These features were compared with traditional uniresolutional shape features in their ability to discriminate among shape classes. These features provided a means of evaluating the shapes at various scales. When utilizing a statistical classification system with Euclidean distance measures determining class membership, the use of multiresolution features significantly increased the classification rates. The classification system when using the multiresolution and uniresolution shape features resulted in classification rates of 83 and 72%, respectively.

Tree-structure wavelet transform is also used to obtain better microcalcification segmentation. Nonlinear multistage tree structured filter suppresses the noise and an edge detection and wavelet transform completed the segmentation. The morphology of the microcalcification and the spatial extent of the cluster were well preserved, which is essential for the later classification (Cheng, Cai, Chen, Hu, & Lou, 2003).

Heine et al. (1997) developed a method for identifying clinically normal tissue in mammograms that separates normal regions from potentially abnormal regions. Its first step is the decomposition of the image with a wavelet expansion, which contains a sum of independent images, each one with different levels of image detail. When there are calcifications, there is strong empirical evidence that only some of the image components are necessary for detecting the abnormality. The underlying statistic for each of the selected expansion components can be modeled with a simple parametric probability distribution function. This corresponds to a statistical test that allows the recognition of normal tissue regions. The distribution function depends on only one parameter, which has a statistical distribution and can be used to set detection error rates. Once the summary statistic is determined, spatial filters that are matched to resolution are applied independently to each selected expansion image. Regions of the image that correlate with the normal statistical model are discarded, producing an output image consisting only of suspicious areas.

The study presented by Wang and Karayiannis (1998) used an approach to detect microcalcifications which employs wavelet-based sub-band image decomposition. Usually, the microcalcifications appear in small clusters with relatively high intensity when compared with the neighbor pixels. These image features can be preserved by a detection system which uses a suitable image transform that can localize the signal characteristics in the original and the transform domain. As the microcalcifications correspond to high-frequency components of the image spectrum, detection of microcalcifications is achieved through the decomposition of the mammograms into different frequency sub-bands, suppressing the low-frequency sub-band, and, finally, reconstructing the mammogram from the sub-bands containing only high frequencies.

4.2.5. Fractal models

Fractals are defined in several different ways, where the most common is a pattern composed of repeated occurrences of a basic unit at multiple scales of detail in a certain order of generation (Rangayyan R. , 2005). These models have been usually used in texture analysis.

Mammographic parenchymal and ductal patterns in mammograms possess structures with high local self-similarity which is the basic property of fractals. Tissue patterns can be constructed by fractal models and can be identified in the original image, and the microcalcification information, which is not similar to the others structures can be enhanced (Sankar & Thomas, 2010), (Thangavel, Karnan, Sivakumar, & Mohideen, 2005). For example, Li, Liu and Lo (1997) proposed a fractal model of breast background tissues to enhance the presence of microcalcifications.

The limitation of fractal modeling is the time required for encoding. A modification of the conventional fractal coding was proposed by Sankar and Thomas (2010) to reduce the encoding time required in the fractal modeling of the mammogram. Hence, instead of searching for a matching domain in the entire domain pool of the image, three methods based on mean and variance, dynamic range of the image blocks, and mass center features are used.

4.2.6. Fuzzy Clustering

These approached apply fuzzy operators, properties or inference rules to handle the uncertainty inherent in the original image. Due to the variable shapes of microcalcifications, these methods approximate inferences (Cheng, Cai, Chen, Hu, & Lou, 2003), (Thangavel, Karnan, Sivakumar, & Mohideen, 2005). These approaches are very efficient to locate microcalcifications in the mammograms with various densities. In fact, microcalcifications can be accurately detected even in dense breast mammograms. Mammogram enhancement is also more adaptive and robust, and the contrast based on fuzzy homogeneity uses both local and global information, which allows to enhance the main feature while suppress the noise (Thangavel, Karnan, Sivakumar, & Mohideen, 2005).

There are different fuzzy approaches. Saha, Udupa, Conant, Chakraborty and Sullivan (2001) employed scale-based fuzzy connectivity methods to segment dense regions from fatty regions in mammograms. The segmented dense and fatty regions were quantified through the measurement of the respective area and total density, and the features were derived from these measures. The features were linearly correlated between the two projections: MLO and CC. The method was found to be robust in the segmentation of dense regions.

A novel approach to microcalcification detection based on fuzzy logic and scale space techniques was presented by Cheng, Wang and Shi (2004). First, the images are fuzzyfied through the fuzzy entropy principal and fuzzy set theory. The images are enhanced and then scale-space and Laplacian-of-Gaussian filter techniques are used to detect the sizes and locations of microcalcifications. The major advantage of the method is its ability to detect microcalcifications even in the mammograms of very dense breasts.

4.3. Classification

A great number of features and classification methods have already been developed to detect and classify the lesions as malignant or benign. If the features are adequate, will highlight the differences between the abnormal and normal tissue, and thus the classifier will be more robust.

In the following, some classification methods to detect mammographic lesions are introduced.

a) Artificial Neural Networks

The development of artificial neural networks (ANN) was inspired by the biological learning systems. In these systems, there is a very complex net of interconnected neurons which possess high information processing abilities of the biological neural systems due to highly parallel processes operations distributed over many neurons. Hence, ANN mimics the highly parallel computation based on distributed representation (Wang, Lederman, Tan, & Zheng, 2010).

Using a set of training data with feature vectors, the ANNs are trained iteratively to minimize the error (Wang, Lederman, Tan, & Zheng, 2010).

The neural network rule extraction algorithms have some general steps: selection and training of the network to attain the pre-specified accuracy requirement; removal of the redundant connections in the network through pruning, while maintaining its accuracy; discretization of the activation values of the pruned network by clustering; extraction of rules that describe the network outputs in terms of the discretized values; generation of the rules that describe the discretized hidden unit activation values in terms of the network inputs. Finally, the two sets of rules generated previously are merged to obtain a set of rules that relates the inputs and outputs of the network (Thangavel, Karnan, Sivakumar, & Mohideen, 2005).

b) Hybrid Neural Network Classification

A hybrid intelligent system to the identification of microcalcification clusters in digital mammograms was presented by Papadopoulos, Fotiadis and Likas (2002). The system has two components: a rule construction and a neural network sub-system. The rule construction includes the feature identification step and the selection of a threshold value for each feature. For every feature, several threshold values are examined in its range of value. For each threshold value is recorded the number of ROIs below and above the threshold value. The ratio of the number of ROIs that belong to a specific class (normal or pathological) over the total number of the ROIs that belong to the same class should be more than 6%.

c) K-Nearest Neighbors

This class of method classifies objects based on the closest training examples in the feature space. Thus, an object is classified according to the majority of its K-nearest neighbors. Hence, it is instance based learning.

For the K-Nearest Neighbors (KNN) is necessary to have a training set not too small, and a good discriminating distance. KNN performs well in multiclass simultaneous problem solving. The parameter K corresponds to the number of nearest neighbors considered to perform the classification. There is an optimal choice for this value that brings to the best performance of the classifier (Masala G. , 2006).

d) Support Vector Machines

Support Vector Machines (SVM) is a machine-learning method, based on the statistical learning theory and the principle of structural risk minimization, which aims to minimize the errors in the data set. Hence, it performs well when applied to data outside the training set. Wei, Yang and Nishikawa (2009) investigated an approach based on Support Vector Machines for detection of clusters of microcalcification in digital mammograms. Microcalcifications are detected as a supervised-learning problem and SVM is applied to develop the detection algorithm. SVM is used to detect at each location in the image whether a microcalcification is present or not. The ability of SVM to outperform several well-known methods developed for the widely studied problem of microcalcification detection suggests that SVM is a promising technique for object detection in a medical imaging application.

e) Relevant vector machine

Relevance vector machine (RVM) is another machine learning technique to detect microcalcifications in digital mammograms. RVM is based on Bayesian estimation theory. A distinctive feature of this theory is that it can yield a sparse decision function that is defined by only a very small number of so-called relevance vectors.

Wei, Yang and Nishikawa (2005) developed a supervised-learning method through the use of RVM as a classifier to determine at each location in the mammogram if a microcalcification is present or not. To increase the computation a two-stage classification network was developed, in which a computationally simple linear RVM classifier is applied first to quickly eliminate the overwhelming majority non-microcalcification pixels in a mammogram. Comparing with SVM it is reduced the computational complexity of the SVM while maintaining the detection accuracy.

f) Fuzzy approaches

The fuzzy binary decision tree procedure contains three steps: splitting nodes, determining terminal nodes, and assigning a class to the terminal nodes. A training data set is split into two independent sets, and a large tree is grown based on the first training set by splitting until all terminal nodes have pure class membership. Then a pruned sub-tree is selected by minimizing the second training set misclassification rate. The procedure is then iterated (Thangavel, Karnan, Sivakumar, & Mohideen, 2005).

There are several fuzzy approaches to classify features. For example, Seker, Odetayo, Petrovic and Naguib (2003)studied the fuzzy-nearest neighbor (FNN) classifier as a fuzzy logic method. This approach provided a certainty degree for prognostic decision and assessment of the markers. The overall results indicated that the FNN-based method yields the highest predictive accuracy, and that it has produced a more reliable prognostic marker model than the statistical and ANN methods.

On the other hand, Grohman and Dhawan (2001) described a convex-set based neuro-fuzzy algorithm for classification of difficult to diagnose instances of breast cancer. With its structural approach to feature, it offers rational advantages over the back propagation algorithm. The training procedure is completely automated-function and parameters are automatically computed from statistical distributions of the data. Two different approaches to construction of fuzzy membership functions were tested: sigmoidal decision surfaces (back propagation-like approach) and bell-shaped functions cluster-specific approach.

4.4. Analysis of bilateral asymmetry

An additional indicator of the presence of breast cancer is the bilateral asymmetry of the left and right breasts. This is defined by the presence of a greater volume or density of breast tissue without distinct mass or prominent ducts in one breast when compared with the other.

Miller and Astley (1994) proposed a technique to detect breast bilateral asymmetry trough anatomical features. The method was based on measures of shape, topology, and distribution of brightness in the fibroglandular disk. An accuracy of 74% was obtained. Another method for the detection of breast tumors by analyzing bilateral asymmetry through the measurement of brightness, roughness, and directionality was proposed by Lau and Bischof (1991), where a sensitivity of 92% was obtained with 4.9 false positives *per* mammogram.

Although all work that has been developed, more methods are desirable in this area to analyze asymmetry from multiple perspectives as can improve the detection robustness.

4.5. Summary

There is a substantial literature research regarding detection and classification of masses and calcifications. Commercial CAD systems have satisfactory effectiveness detecting masses and calcifications. However, certain areas of research in CAD of breast cancer still require attention. For example, only a small number of researchers focused on detecting architectural distortions in the absence of mass. And even fewer studies have been done in order to detect bilateral asymmetry. Hence, the development of new breast cancer computer-aided detection is an active research field, particularly regarding the detection of subtle abnormalities in mammograms.

Usually, CAD integrates common steps: image pre-processing, image enhancement, detection and classification of lesions. There are plenty dissimilar approaches to the different phases. These approaches can still be improved and new approaches or even distinct combination of techniques can be used in order to create better algorithms for more robust and efficient computer aided detection of breast tumors.

CHAPTER 5

IMPLEMENTATIONS, RESULTS AND DISCUSSION

This chapter presents a description about the different methodologies implemented, as well as exemplifications of their results and their evaluation. The techniques have been implemented in MATLAB® (version 7.11.0.584 – R2010b) in a computer with CPU T9550 with 2.66GHz and 3GB RAM memory.

All the mammographic images correspond to real cases obtained from mini MIAS Database (Suckling, 1994), which contains MLO views of both left and right breasts. Twenty real mammograms with clustered and single microcalcifications in fatty, fatty glandular and dense breasts were chosen from that dataset as testing images. The database identified also the location of breast lesions. The images in the database were digitized at a resolution of 50 µm *per* pixel with 1024×1024 pixel size and at 256 gray levels. The images are in the grayscale file format (.pgm).

5.1. Image Enhancement

Breast lesions such as masses and calcifications may be small and have low contrast when compared with the surrounding breast tissue, which difficult their detection. Enhancement techniques aim to improve contrast or visibility of those image features, as was described in section 4.1, improving the ability for the radiologist to perceive subtle lesions, leading to a more accurate diagnosis (Rangayyan, Ayres, & Desautels, 2007).

The enhancement techniques chosen correspond to some of the most commonly enhancement methodologies used on mammographic images as are the furthermost suitable to enhance the characteristics of such images.

In order to evaluate the enhancement, an area of interest including the ROI was extracted as exemplified in Figure 5.1. The choice of those ROI's was performed with the aid of a radiologist. The size of those areas was equal to 101x101 pixels in all the images. The regions were split in foreground, which corresponds to the pixels representing microcalcifications and background, which were the remaining pixels.

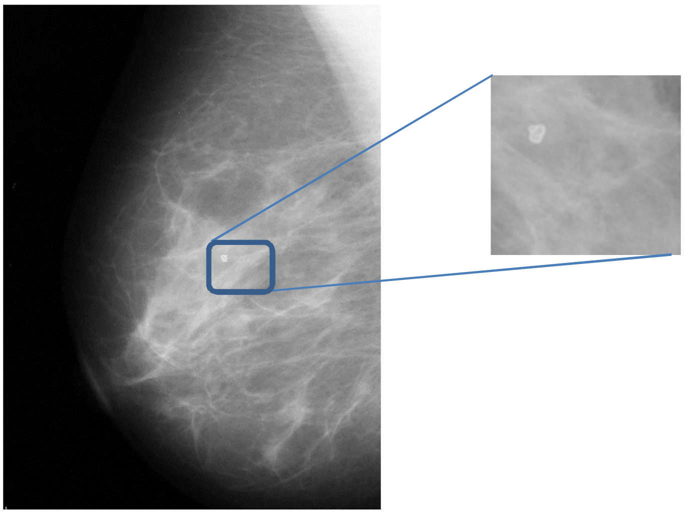

Figure 5.1 – Example of a mammographic image and a region of interest with a microcalcification.

The implementation of the enhancement techniques employed is described in the next section, as well as the corresponding result and discussion. Posteriorly, the techniques are evaluated using the parameters indicated in section 4.1.13. This evaluation is performed by implementing the methodologies in the twenty mammographic images set chosen from the mini-MIAS database.

5.1.1. Contrast-Limited Histogram Equalization

The first step of this technique, CLAHE, corresponds to the determination of the tiles of the input image. Increasing the number of tiles in the function, there is a higher image enhancement. However, when too high is computationally demanding and there is a distortion of the original image.

The algorithm was based on the one proposed in (Zuiderveld, 1994). The local neighborhood is usually a square tile centered at the pixel being processed. The square size is a crucial parameter: when too small, the method is too sensitive to local variations and is computationally expensive; when too large, there are limitations similar to the non-adaptive technique. Several two-element vector of positive integers specifying the number of tiles by row and column number of tiles were used in order to determine the vector with best image enhancement results (Baert, Reiser, Hricak, & Kanuth, 2010), (Pizer, et al., 1987), (Sivaramakrishna, Obuchowski, Chilcote, Cardenosa, & Powell, 2000).

From each of those tiles, a histogram is made, being clipped by a contrast enhancement limit, where higher numbers result in higher contrasts. Several experiments about this value were made, and the value with best result was equal to 0.01.

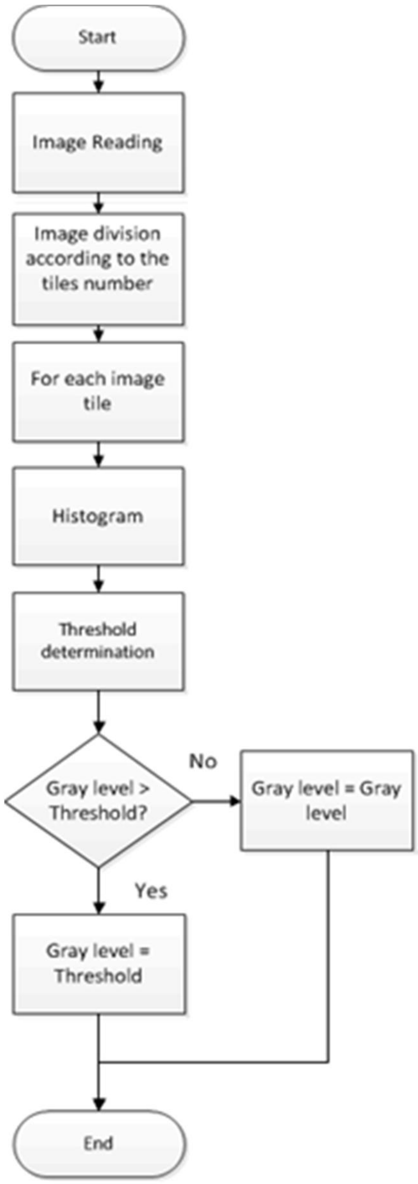

Figure 5.2. – Flow chart of contrast-limited adaptive histogram equalization.

The transformation function is created for this region through the matching of it histogram to a pre-specified one. The pre-specified histograms can have (1) linear distribution, where the gray levels tend to have a flat distribution along the entire span; (2) exponential distribution, where the gray levels tend to be distributed with higher frequency in the higher levels of gray, such as in the exponential curves; (3) Rayleigh distribution, which corresponds to a bell-shaped histogram, where the gray-levels tend to be distributed more in the middle values of gray. The gray level mappings were combined using bilinear interpolation in order to assemble the final enhanced image eliminating induced boundaries. The flow chart of this algorithm is represented in Figure 5.2.

Figure 5.3 shows the enhancement results of CLAHE on one real mammogram with different tile sizes and distribution. Different tiles were tested, however, only tiles 4x4 and 32x32 pixels are presented. In Figure 5.3b, each tile of 4x4 pixels was enhanced by matching a linear histogram distribution, demonstrating a clear enhancement of breast fibroglandular tissue and microcalcifications, whereas there is a slight attenuation of the breast background. The breast background is in this matter considered the breast area that does not correspond to fibroglandular tissue or breast lesions.

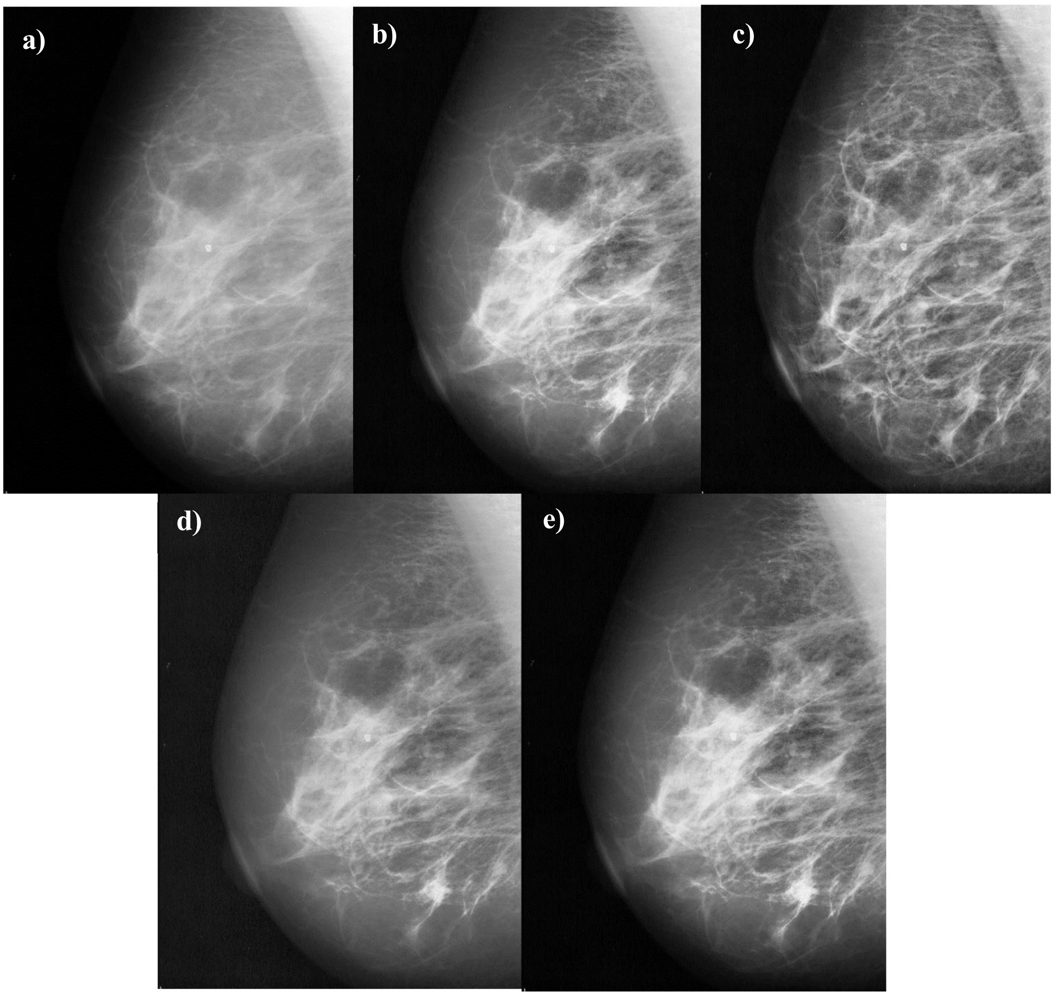

Figure 5.3 – Results of CLAHE: a) Original mammographic image; b) Image after CLAHE with tile of 4x4 pixels and uniform distribution; c) Image after CLAHE with tile of 32 x32 pixels and uniform distribution; d) Image after CLAHE with tile of 4x4 pixels and bell-shaped distribution; e) Image after CLAHE with tile of 4x4 pixels and exponential distribution.

The contrast enhancement limit was set equal to 0.01 as higher values result in image distortion, which precludes the further detection of regions of interest.

Changing the tile size to 32x32 pixels, Figure 5.3c and Table 5.1, also with linear distribution, the breast fibroglandular tissue and small lesions were enhanced, and the breast background was softened. However, there was an increase of noise in the image.

When the histogram was matched to an exponential distribution, Figure 5.3e, occurred, as expected, an intense enhancement of the brighter regions, breast fibroglandular tissue and microcalcifications, whereas there was a softening of the darker areas, which correspond to the background of the breast. Rayleigh histogram distribution, Figure 5.3d, enhanced with higher intensity the gray areas, as it matches to a bell-shape histogram distribution.

In order to evaluate quantitatively the enhancement results of this algorithm, some parameters were used: CII, BNL, PSNR and ASNR, Table 5.1.

Table 5.1 – Evaluation parameters (CII, BNL, PSNR and ASNR) of CLAHE.

		Original image	**Linear distribution, Tile 32x32**	**Linear distribution, Tile 4x4**	**Rayleigh Distribution, Tile 4x4**	**Exponential distribution, Tile 4x4**
	ROI example	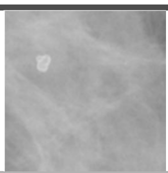	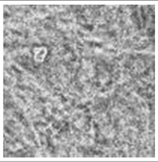	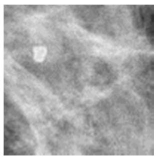	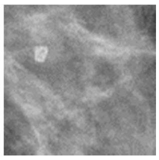	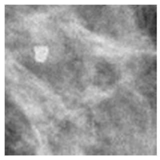
CII	μ	1	1.111	1.128	1.393	1.509
	σ	1	0.147	0.126	0.156	0.054
BNL	μ	0.082	0.123	0.115	0.116	0.230
	σ	0.049	0.018	0.034	0.025	0.033
PSNR	μ	5.472	3.204	3.505	3.797	2.134
	σ	3.588	0.438	1.366	2.136	1.525
ASNR	μ	3.892	1.572	2.833	3.018	1.983
	σ	2.478	0.368	0.969	1.247	1.054

The result with best performance, considering CII, corresponds to the tile of 4x4 pixels, where the exponential distribution had highest value. As the BNL corresponds to the background noise level, as lower this value is the best. However, the lower BNL value corresponded to the original image, when compared with the enhanced ones, since the enhancement algorithms usually also enhance the fibroglandular tissue, which is frequently surrounding the microcalcifications, being considered as noise when BNL is calculated. However, the enhanced images with inferior BNL corresponded to the methodology performed with tile of 4x4 pixels and linear and bell-shape distribution. The PSNR and ASNR values were also inferior to the ones in the original image. Considering only the enhanced images, the highest value corresponds to the methodology performed with tile of 4x4 pixels and linear and bell-shape distribution. Consequently, the noise level is an important factor, as it may influence the segmentation process.

This algorithm is not computationally demanding, with an average of 0.4 seconds to perform the algorithm in a 1024x1024 pixel mammography.

Concluding, this algorithm improved the contrast of the microcalcifications; however, introduced some noise to the image due to the enhancement of the fibroglandular tissue surrounding the microcalcifications. When compared the different parameters of the algorithm, the enhancement results in terms of CII, BNL, PSNR, ASNR and even due to a visual analysis, corresponded to the one with tile of 4x4 pixels and linear or bell-shaped distribution.

5.1.2. Contrast Stretching

The intensity values of the input image *I* were mapped into new values, where the lowest image intensity (low_{in}) was saturated at 1% of the lower values (low_{out}) and where the highest image intensity ($high_{in}$) was saturated at 1% of the higher values ($high_{out}$) of image intensity. The remainder intensities were adjusted in the interval [0, 1], according to:

$$J = low_{out} + (high_{out} - low_{out}).* \left(\frac{(I - low_{in})}{high_{in} - low_{in}}\right)^{gamma}. \qquad \textbf{(5.1)}$$

In this equation, *gamma* specifies the shape of the curve which describes the relationship between *I* and *J* values:

- *gamma* <1 – mapping weighted toward higher output values;
- *gamma* = 1 – linear mapping;
- *gamma* >1 – mapping weighted toward lower output values.

The mapping of the new values was performed linearly (*gamma*=1) and non-linearly (*gamma*=0.2 and *gamma*=2).

The flow-chart of the algorithm is depicted in Figure 5.4.

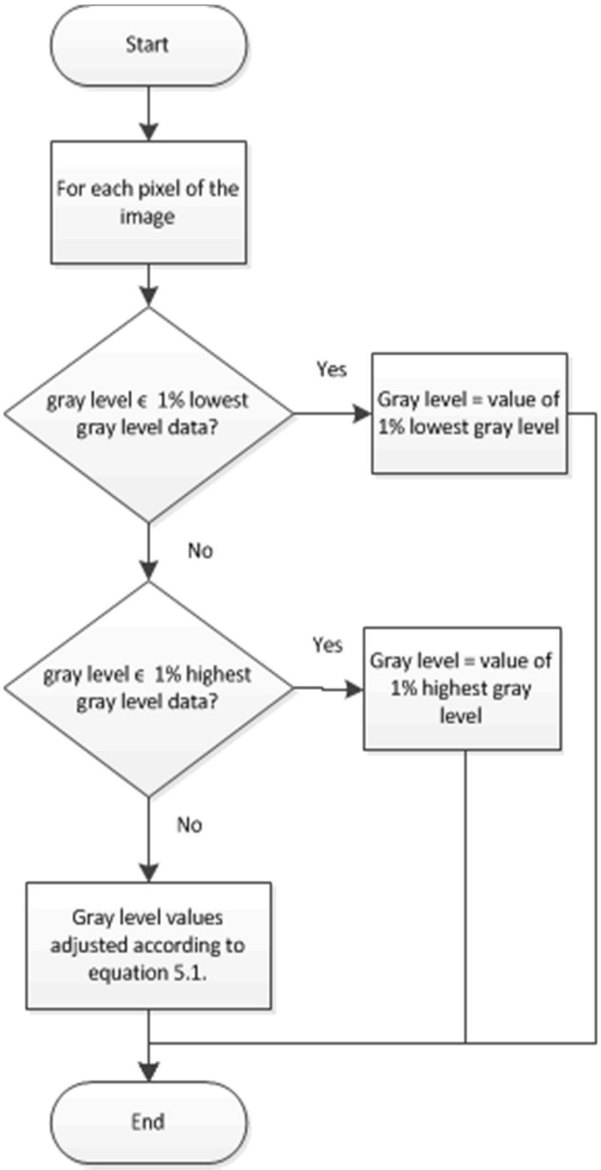

Figure 5.4 – Flow chart of the contrast stretching algorithm.

Figure 5.5 shows the histograms that resulted from the enhancement of real mammograms with contrast stretching with different intensity mapping. Comparing Figure 5.5a and b it is possible to verify that the gray level intensities are distributed linearly along the entire span of the histogram, enhancing the image, as can be observed in Figure 5.6b and on the region of interest represented in Table 5.2.

Non-linear contrast stretching with *gamma* equal to 2, Figure 5.5c and Figure 5.6c, distributed the gray value intensities along the entire span, but with more intensity in the area with gray values inferior to 0.5, darkening the image. On the other hand, non-linear contrast stretching with *gamma* of equation 5.1 equal to 0.2, Figure 5.5d and Figure 5.6d, distributed the gray values above 0.5, lightening the image.

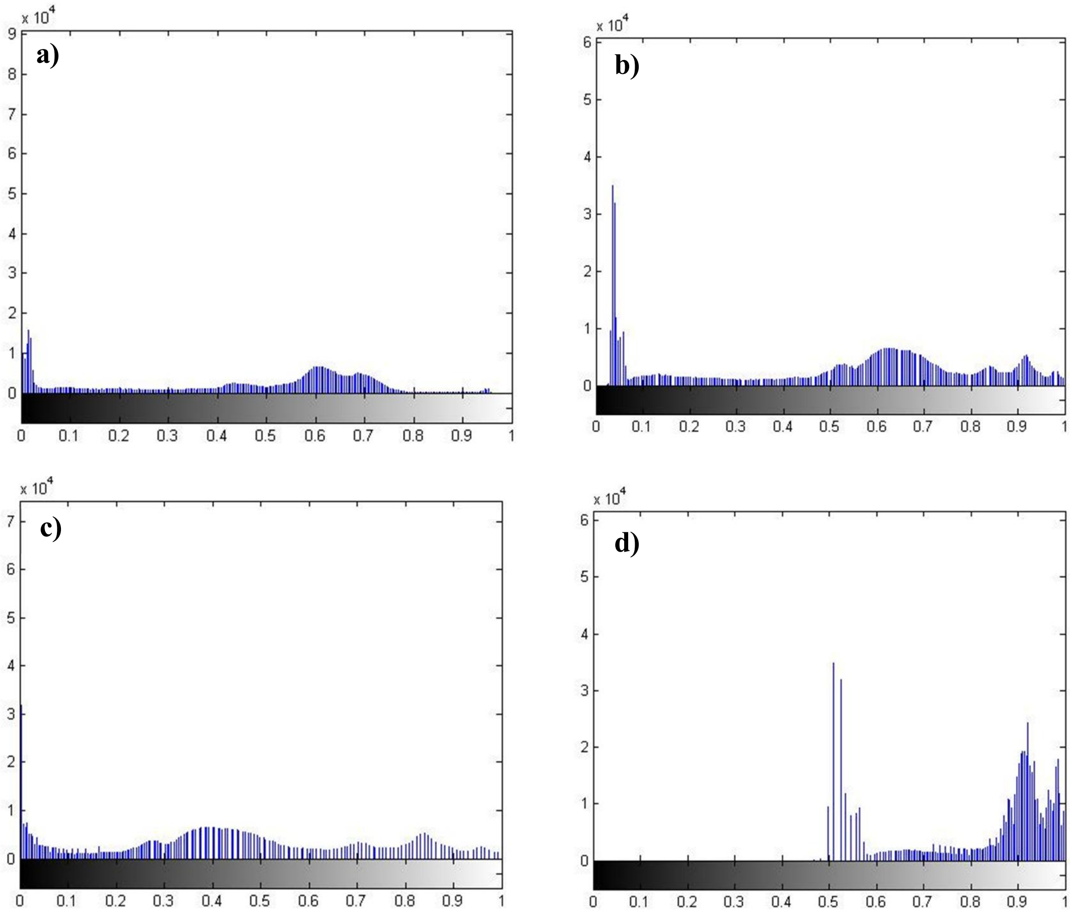

Figure 5.5 – Results of contrast stretching technique: a) histogram of the original image; b) histogram after linear contrast stretching (*gamma*=1); c) histogram after non-linear contrast stretching (*gamma*=2), d) histogram after non-linear contrast stretching (*gamma*=0.2).

Comparing quantitatively the performance of this algorithm, Table 5.2, it is possible to verify that CII had the best performance for contrast stretching with linear distribution, but having with very similar results with non-linear distribution, *gamma* equal to 2. BNL was inferior for the original image due to the reasons previously indicated for CLAHE. Nevertheless, the enhancement techniques with lower BNL corresponded to contrast stretching with *gamma* equal to 1 and *gamma* equal to 2.

Non-linear contrast stretching with *gamma* equal to 2 had higher mean value of PSNR and ASNR when compared to the original image. However, the values of standard distribution of this parameter were very high, which indicates that this technique differs greatly for different mammographic images. Thus, the value of *gamma* with best results varies in the different mammographic images.

This algorithm is not computationally demanding, spending 0.3 on average to perform the technique on a 1024x1024 mammography.

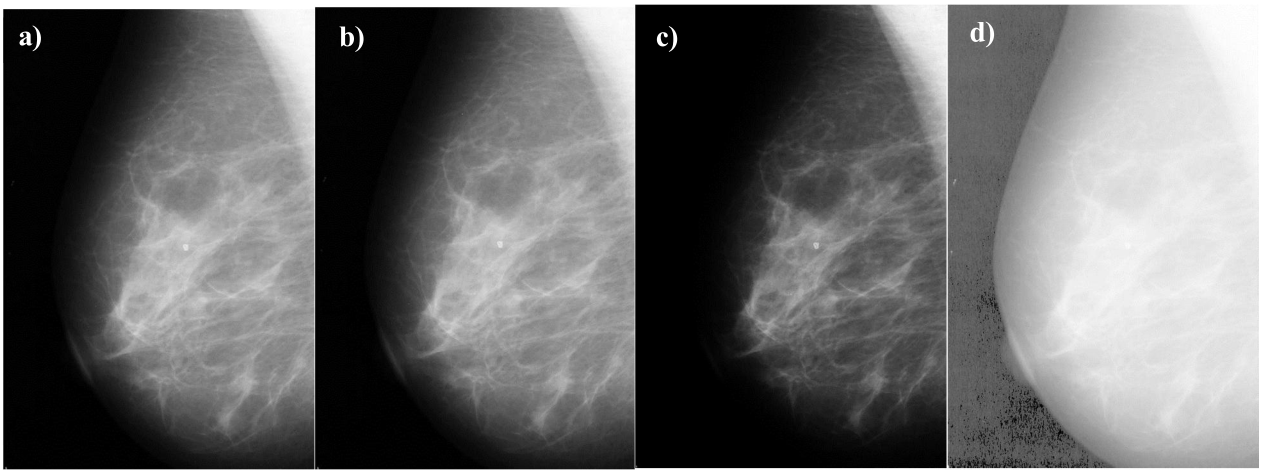

Figure 5.6 – Results of contrast stretching technique: a) Original image; b) Image after linear contrast stretching (*gamma*=1); c) Image after non-linear contrast stretching (*gamma*=2), d) Image after non-linear contrast stretching (*gamma*=0.2).

Table 5.2 – Evaluation parameters (CII, BNL, PSNR and ASNR) of contrast stretching technique.

		Original image	Linear distribution	Non-Linear distribution, *gamma*=2	Non-Linear distribution, *gamma*=0.2
ROI example		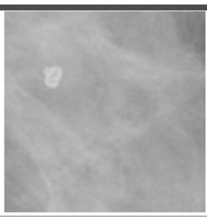	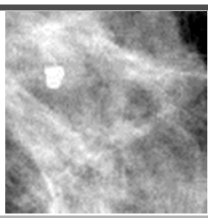	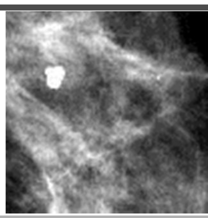	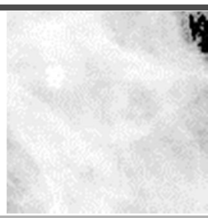
CII	μ	1	2.485	2.472	1.449
	σ	1	0.265	0.312	0.674
BNL	μ	0.082	0.209	0.206	0.132
	σ	0.049	0.058	0.079	0.014
PSNR	μ	5.472	2.958	5.963	1.276
	σ	3.588	2.478	8.733	0.642
ASNR	μ	3.892	2.691	4.903	1.219
	σ	2.478	1.900	5.650	0.554

Concluding, this algorithm improved the microcalcifications contrast. When compared with the original image, the peak and average signal to noise ratio were increased for the non-linear contrast stretching, *gamma* equal to 2. The linear contrast stretching introduced some noise into the image due to the slight enhancement of the fibroglandular tissue surrounding the microcalcifications. The nonlinear contrast stretching, *gamma* equal to 2 has, in general, a good enhancement performance in terms of the numerical evaluation, but, as evidenced in the standard deviation, it has an inconstant reduction of noise.

5.1.3. Adaptive Neighborhood Contrast Enhancement

Adaptive neighborhood contrast enhancement, as previously mentioned in section 4.1.5, adapts the size of the neighborhood to the local properties, which allows the enhancement of image details.

The first step of the implemented algorithm ANCE corresponds to the determination of the extent of the adaptive neighborhood of each pixel, which was performed with a region growing procedure applied to the non-black pixels (usually the background in mammographic images). The region growing procedure used was based on (Kroon, 2010). Hence, through this method is obtained a foreground and a background region for each pixel.

The contrast value of each region was calculated using equation 4.9. The contrast C was replaced by the C', which was obtained by the calculus of different parameters: square root and a look-up table based on (Morrow, Paranjape, Rangayyan, & Desautels, 1992):

$$C' = \begin{cases} 0.475\,C & 0 \leq C < 0.1 \\ 2.2\,C - 0{,}0425 & 0.1 \leq C < 0.15 \\ 1.6\,C - 0{,}12 & 0.15 \leq C < 0.275. \\ 1.0462\,C - 0{,}1223 & 0.275 \leq C < 0.375 \\ C & C \geq 0.375 \end{cases} \qquad \textbf{(5.2)}$$

Several different techniques were used and tested in calculating C', such as logarithm and exponential of C; however, without good enhancing results.

The value of the new foreground pixels was obtained according to:

$$f' = b\,\frac{1+C\prime}{1-C\prime} \qquad \textbf{(5.3)}$$

The flow chart of the implemented algorithm is represented in Figure 5.7.

This technique is computationally very expensive, spending about 1700 seconds to perform the algorithm on a 101x101 pixel mammography. This algorithm was implemented based on the global steps of the ANCE algorithm indicated in (Morrow, Paranjape, Rangayyan, & Desautels, 1992).

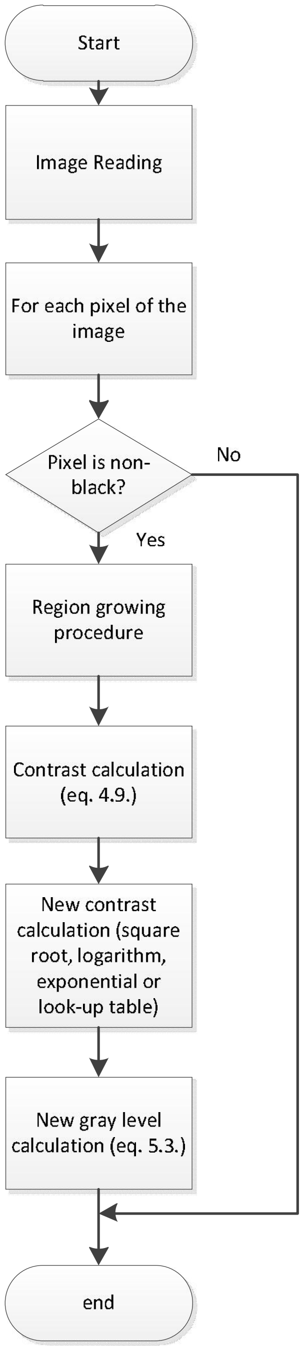

Figure 5.7 – Flow chart of the implemented ANCE algorithm.

Table 5.3 indicates the results and evaluating parameters of the enhancement after the ANCE algorithm on the region of interest. Accordingly, it is possible to verify that there was a slight increase in the contrast when compared with the original image in both techniques, having highest increasing with the square root calculation of C'. From BNL results, it is possible to realize that this methodology decreased the background noise ratio in both techniques to calculate C'. However, PSNR and ASNR also decreased when compared with the original image due to the similar values between the foreground gray level (maximum and average, respectively) and the mean background gray level. Nevertheless, the standard deviation of these results is high, indicating that this methodology has variable performance in different mammographic images.

Table 5.3 – Evaluation parameters (CII, BNL, PSNR and ASNR) of the implemented techniques of adaptive neighborhood contrast enhancement: square root, exponential, logarithm and a pre-specified function of the contrast of the original image.

		Original image	$C' = \sqrt{C}$	$C' = f(C)$
ROI example		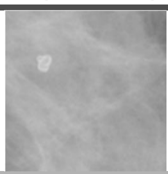	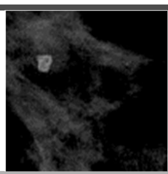	
CII	μ	1	1.550	1.060
	σ	1	0.709	1.115
BNL	μ	0.082	0.009	0.065
	σ	0.049	0.000	0.001
PSNR	μ	5.472	1.376	1.330
	σ	3.588	3.183	1.572
ASNR	μ	3.892	0.052	0.547
	σ	2.478	1.644	0.866

In conclusion, this algorithm improved, in general, the microcalcifications contrast. PSNR and ASNR were also reduced for both C' calculations when compared with the original image. However, the required computational time is a disadvantage of this technique.

5.1.4. Unsharp masking

Unsharp masking is used to sharpen images, by the use of a mask convolved with the original image, amplifying high frequency components.

The shape of the unsharp mask is controlled by the parameter α, which influences the weight of the mask. The mask is built according to (The MathWorks, Inc. , 2011):

$$\frac{1}{\alpha+1}\begin{bmatrix} -\alpha & \alpha-1 & -\alpha \\ \alpha-1 & \alpha+5 & \alpha-1 \\ -\alpha & \alpha-1 & -\alpha \end{bmatrix}. \qquad \textbf{(5.4)}$$

Figure 5.8 shows an example of the used of unsharp filtering on a real mammographic image.

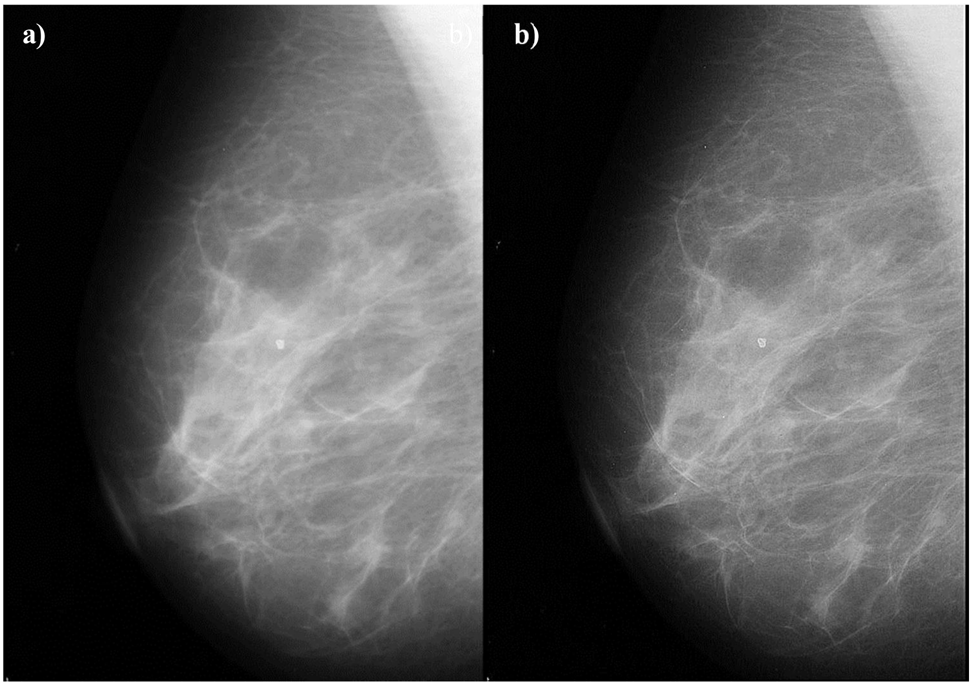

Figure 5.8 – Result of unsharp filtering: a) Original Image; b) Image after unsharp filtering with α=0.2.

Table 5.4 – Evaluation parameters (CII, BNL, PSNR and ASNR) of unsharp filtering with different α values.

		Original image	Unsharp filtering α=0.2	Unsharp filtering α =0.5	Unsharp filtering α =0.9
	ROI example	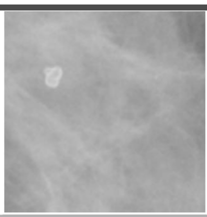	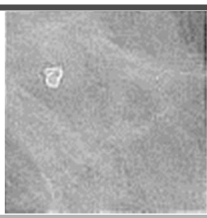	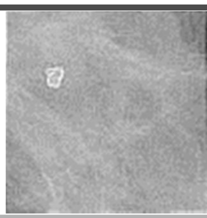	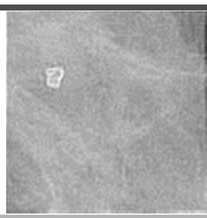
CII	μ	1	1.269	1.253	1.245
	σ	1	0.039	0.004	0.035
BNL	μ	0.082	0.099	0.097	0.097
	σ	0.049	0.057	0.057	0.058
PSNR	μ	5.472	6.768	6,659	6,599
	σ	3.588	4.434	4,312	4,311
ASNR	μ	3.892	3.887	3,947	3,976
	σ	2.478	2.279	2,351	2,390

Through the analysis of the data in Table 5.4, it is possible to verify that increasing the value of α, the contrast of the enhanced image decreased slightly. However, the background noise level, PSNR and ASNR also decreased. As α decreased, less sharpening was accomplished, because the mask had less weight, which reduced the noise influence but also reduced the image contrast.

The result of unsharp enhancement possessed a ringing artifact, mainly in the enhancement results with higher sharpening. This artifact corresponded to a white band near the edge, as can be observed in the ROI of Table 5.4, which corresponded to additional noise provided to the image that may affect further segmentation results.

As the results from this enhancement method have similar numerical values, the unsharp masking used in later algorithms for comparison was considered to have α value equal to 0.2, since it corresponds to a higher sharpening of the image.

5.1.5. Adaptive Unsharp masking

The adaptive unsharp masking filter was obtained by adding a weighted high-pass filtered image to the input image, $f_{in}(x,y)$, (Bae, Shamdasani, Managuli, & Kim, 2003):

$$f_{out}(x,y) = f_{in}(x,y) + C(x,y)f_{hpf}(x,y), \tag{5.5}$$

where $C(x,y)$ corresponds to the weight of the high-pass filtered image and $f_{hpf}(x,y)$ corresponds to the high-pass filtered image.

The gain of the high-pass filter is controlled based on local image characteristics. Initially, a Sobel filter is applied on the image, emphasizing the contour of objects and the high frequency isolated patterns, which can be object details or noisy regions. As anatomical objects tend to change the pixel values smoothly compared to spike-like noise, they do not produce very large gradients with the Sobel operator. This step is followed by a maximum gradient filtering, which corresponds to a dilation of the image with a 3x3 neighborhood in order to obtain the highest gradient values of the contour. Additionally, a median filter with a neighborhood of 3x3 pixels is applied to smooth the result from the previous procedures and to reduce the influence of noise. The result of these operations is the emphasis gain of each pixel, $C(x,y)$, which is linearly proportional to the maximum gradient to enhance image details.

Simultaneously, the high-pass filter of the image is calculated, which in this case corresponded to a Butterworth high-pass filter of order 2.

This high-pass filter was weighted through the multiplication of the emphasis gain, previously calculated. The result image corresponds to the addition of the original image to this weighted high-pass filter, as described in equation 5.5.

The algorithm developed for this adaptive unsharp masking was based on an adaptation of the description of (Bae, Shamdasani, Managuli, & Kim, 2003).

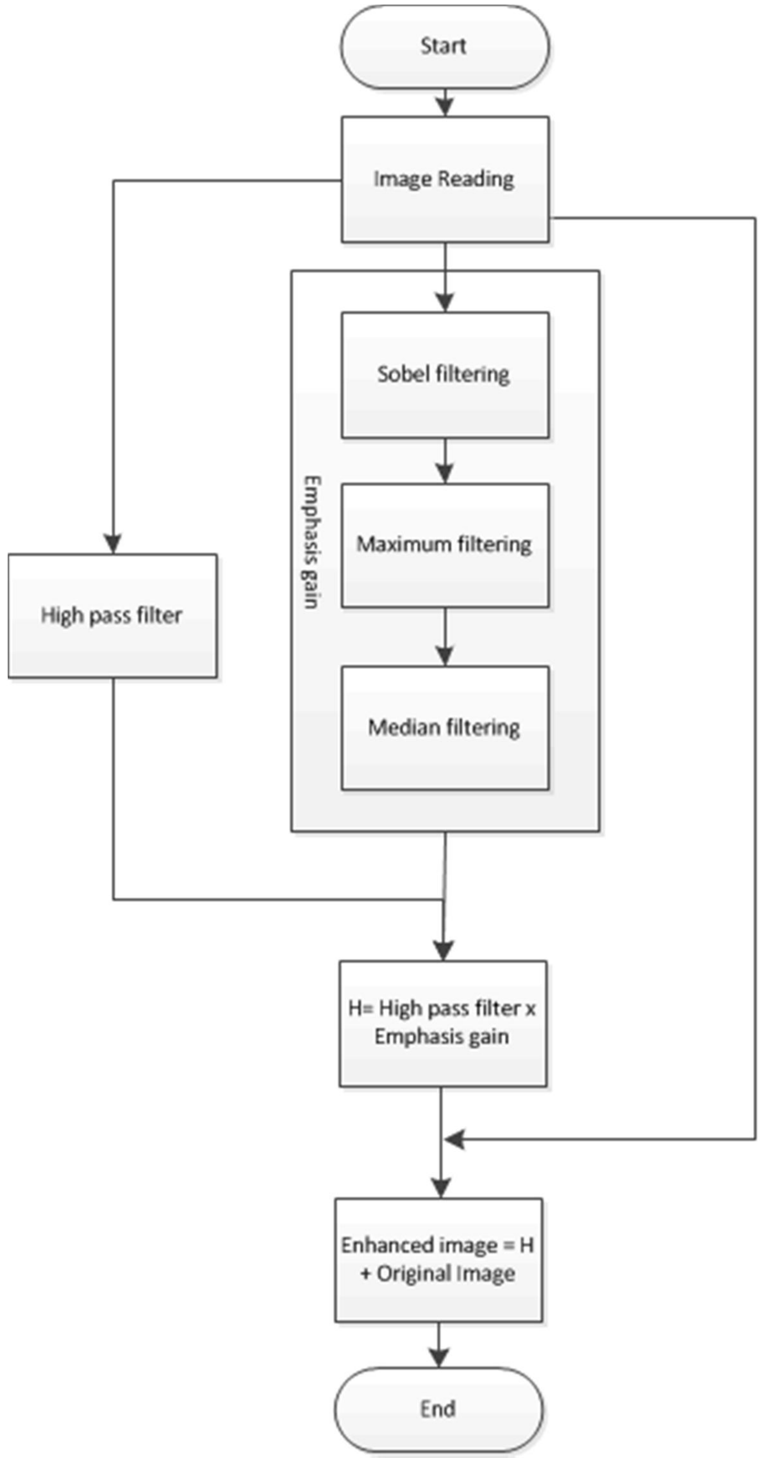

Figure 5.9 – Diagram of the implemented adaptive unsharp filtering.

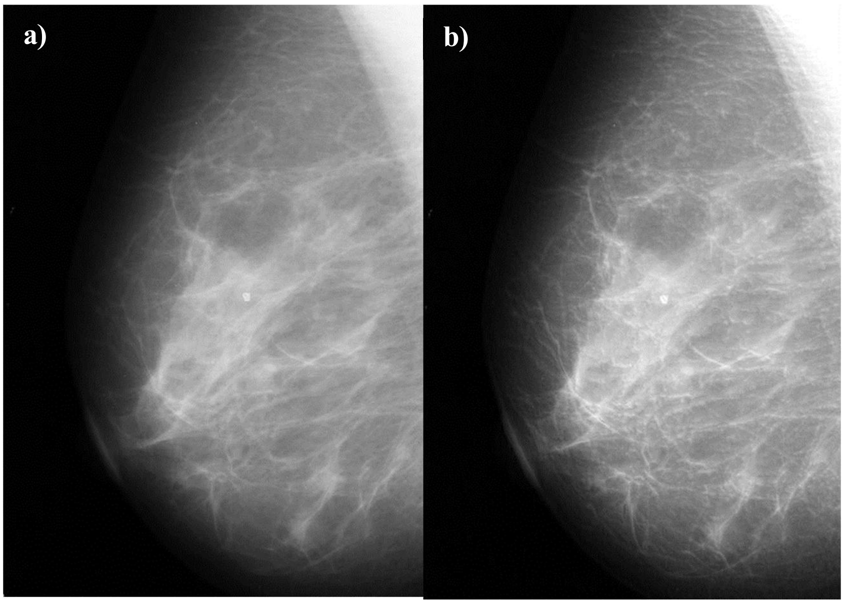

Figure 5.10 – Result of adaptive unsharp filtering: a) Original Image; b) Image after adaptive unsharp filtering.

From Figure 5.8 and Figure 5.10, it is possible to visually verify that unsharp masking and adaptive unsharp masking enhanced primarily the gray level correspondent to the mammographic lesions and some breast tissue with sharp changes in the image.

Table 5.5 – Evaluation parameters (CII, BNL, PSNR and ASNR) of the techniques of unsharp filtering and adaptive unsharp filtering.

		Original image	Unsharp filtering (α=0.2)	Adaptive Unsharp filtering
ROI example		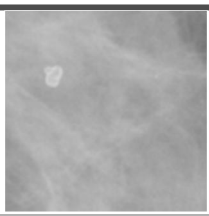	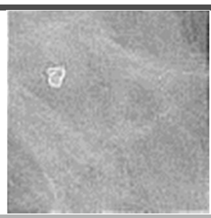	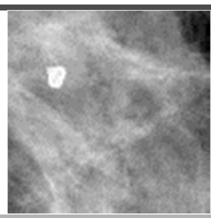
CII	μ	1	1.269	3.287
	σ	1	0.039	1.965
BNL	μ	0.082	0.099	0.153
	σ	0.049	0.057	0.058
PSNR	μ	5.472	6.768	5.748
	σ	3.588	4.434	3.702
ASNR	μ	3.892	3.887	4.000
	σ	2.478	2.279	2.508

Table 5.5 indicates the evaluation parameters of unsharp and adaptive unsharp techniques. Both increased the contrast when compared with the original image, but adaptive unsharp filtering with visible higher increase. The background noise level was slightly higher than the original image for the reasons previously described; however, in the case of unsharp filtering the difference between the original and the enhanced images was minimal. PSNR and ASNR were higher when compared with the original image for both techniques. Adaptive unsharp masking has no ringing artifact unlike the unsharp masking.

The unsharp filtering had a computational duration of about 0.2 seconds, whereas the adaptive unsharp filtering had a computational duration of about 0.3 seconds, in both cases, on a 1024x1024 pixels mammographic image.

Concluding, both unsharp techniques had similar results. Adaptive unsharp masking have a higher contrast increasing but with additional noise enhancement.

5.1.6. Homomorphic Filter

This filter is developed in the frequency domain. The first step of the algorithm corresponds to the determination of the image logarithm, being followed by the Discrete Fourier Transform of it result. A filter is applied to this frequency domain of the image, which allows the enhancement of the high frequency values and a decrement of the low frequency values. The filter used is given as:

$$H = 0.9\left(1 - e^{\frac{2\left(i-\frac{r}{2}\right)^2 + 2\left(j-\frac{c}{2}\right)^2}{10}}\right), \qquad \textbf{(5.6)}$$

where r and c corresponds to the number of rows and columns of the image, respectively, while i and j corresponds to number of the row and column of each image pixel. The inverse Discrete Fourier Transform and exponential functions are performed in order to restore the image domain, Figure 5.11.

The filter H used was adapted from the one proposed by Praveen Kumar (2009) in order to provide higher enhancement of microcalcifications and breast lesions.

Figure 5.11 – Homomorphic filtering approach for image enhancement (adapted from (Gonzalez & Woods, 2002)).

Figure 5.12 shows the result from the enhancement of real mammograms with the homomorphic filtering implemented.

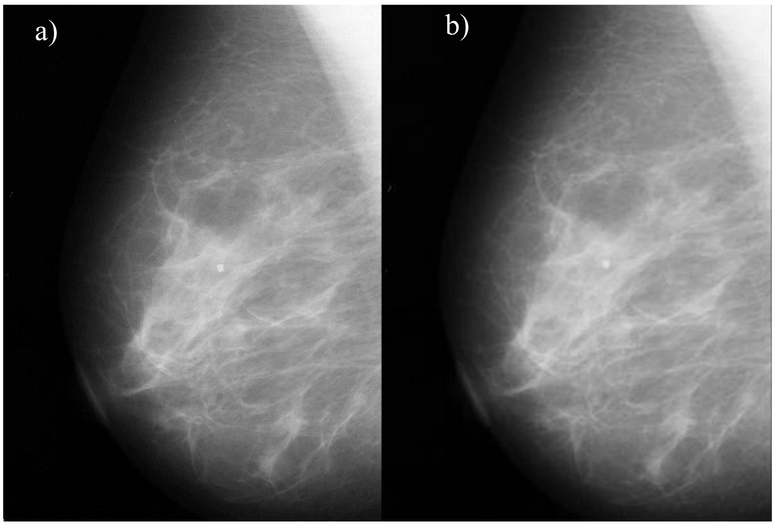

Figure 5.12 – Result of homomorphic filtering: a) Original Image; b) Image after homomorphic filtering.

Table 5.6 – Evaluation parameters (CII, BNL, PSNR and ASNR) of the homomorphic filtering.

		Original image	Homomorphic filtering
	ROI example	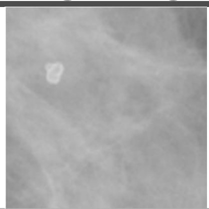	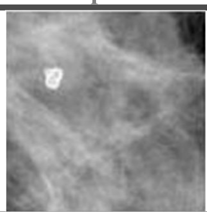
CII	μ	1	0.575
	σ	1	0.433
BNL	μ	0.082	0.002
	σ	0.049	0.002
PSNR	μ	5.472	4.970
	σ	3.588	3.233
ASNR	μ	3.892	3.615
	σ	2.478	2.286

In general, contrast was slightly decreased when compared with the original image (Table 5.6). The background noise level was notoriously decreased when compared with the original image. However, the peak and average signal to noise ratio were slightly inferior to the ones of the original image.

This algorithm had a computational demanding of about 11 seconds when applied on a mammographic image of 1024 x 1024 pixels.

5.1.7. Median Filtering

Median filtering corresponds to a nonlinear smoothing filter, as previously cited in section 4.1.8 b), which is used to reduce random noise. This smoothing filtering in particular was tested as it allows further edge preservation, when compared with the others smoothing filtering. (Gonzalez & Woods, 2002).

This filtering ranks the image pixels in a certain neighbor of a central pixel and replaces the value of this by the median of the neighborhood. Several neighborhood sizes were tested, as represented in Table 5.7

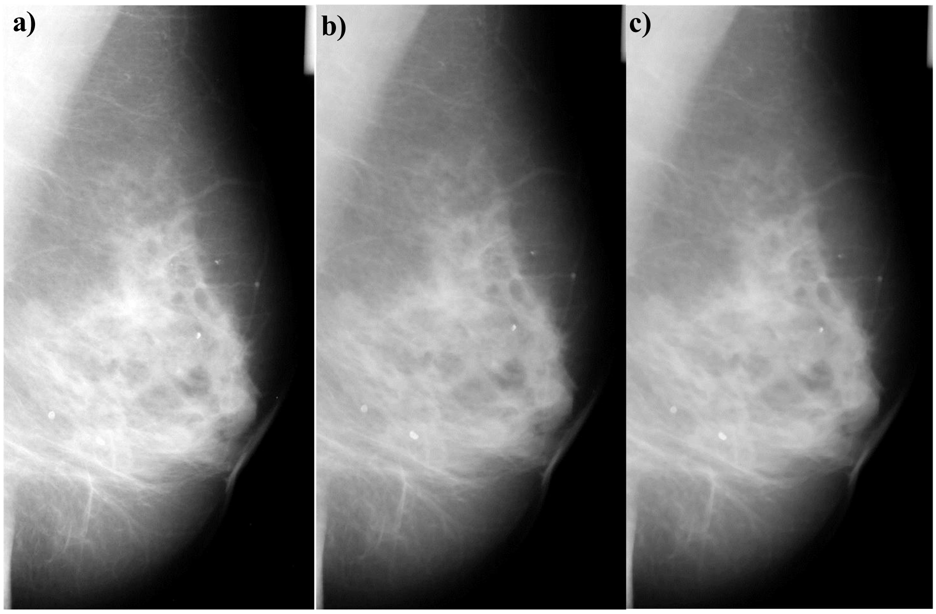

Figure 5.13 – Median filtering approach for image enhancement.
a) Original image, b) Median filter with 3x3 neighborhood,
c) Median filter with 5x5 neighborhood.

Figure 5.13 demonstrates the result from the median enhancement. Table 5.7 indicates, as expected, that the contrast was inferior to the original image, decreasing as the neighborhood size is increased. The background noise level was similar to the original image, whereas the PSNR and ASNR were inferior to the one of the original image, increasing as the neighborhood increases. Thus, the information of the image signal is even further masked with the enhancement. With the neighborhood increasing, the image had further blur, however decreasing the sharpness of the image details, as microcalcifications. This fact allowed the decreasing of noise, but a reduction of image contrast.

This algorithm had a computational expense of about 0.36 seconds of implementation in a mammographic image of 1024 x 1024 pixels.

Table 5.7 – Evaluation parameters (CII, BNL, PSNR and ASNR) of the median filtering.

		Original image	Median filtering with 3x3 neighborhood	Median filtering with 5x5 neighborhood
ROI example		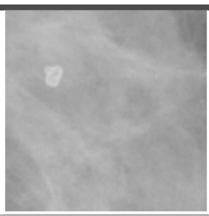	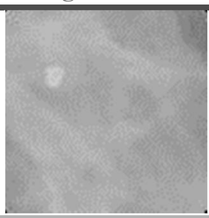	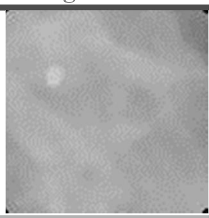
CII	μ	1	0.905	0.863
	σ	1	0.029	0.016
BNL	μ	0.082	0.082927	0.082
	σ	0.049	0.048573	0.047
PSNR	μ	5.472	4.941	4.249
	σ	3.588	3.384	2.952
ASNR	μ	3.892	3.503	2.863
	σ	2.478	2.350	2.033

Concluding, this filter reduces the contrast information and the noise level is not reduced. Thus, as expected, this algorithm does not provide any improvement to the detection of breast lesions in the mammographic images.

5.1.8. Comparison

The best results of each enhancement technique implemented are analyzed in this section, Figure 5.14 and Table 5.8.

Analyzing Figure 5.14, it is possible to verify that in general, the microcalcifications of the enhanced mammograms are visibly more distinguishable when compared with the original image. The overall shape of the mammogram and especially of the regions of interest were preserved, thus this requirement of image enhancement was achieved by all methodologies.

From the analysis on the data in Table 5.8, it is possible to verify that in all the enhancement techniques, the contrast was enhanced when compared with the original image, except for the homomorphic filtering and median filtering. The technique with higher CII corresponds to adaptive unsharp marking enhancement, followed by the contrast stretching results.

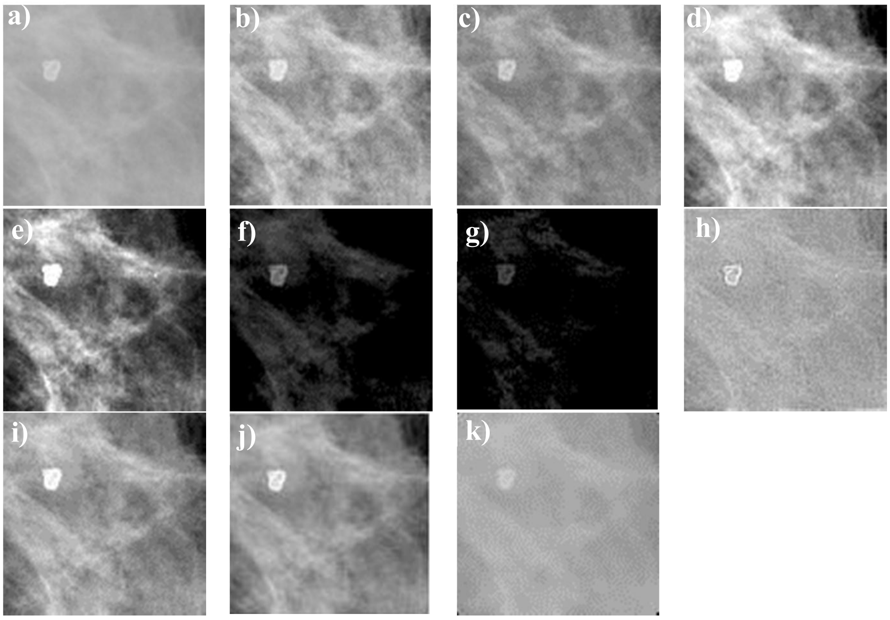

Figure 5.14 – Examples of regions of interest with a microcalcification enhanced with several techniques: a) original image; b) CLAHE with a linear distribution and a tile 4x4, c) CLAHE with Rayleigh distribution and a 4x4 tile, d) contrast stretching with linear distribution, e) contrast stretching with non-linear distribution and *gamma*=2, f) ANCE with $\boldsymbol{C'} = \sqrt{\boldsymbol{C}}$, g) ANCE with *C'=f(C)*, h) unsharp filtering, i) adaptive unsharp filtering, j) homomorphic filtering, k) median filtering with 33x neighborhood.

Table 5.8 – Evaluation parameters (CII, BNL, PSNR and ANSR) of the implemented enhancement techniques.

		Original image	**CLAHE (linear)**	**CLAHE (Rayleigh)**	**Contrast stretching (linear)**	**Contrast stretching (non-linear)**	**ANCE ($C' = \sqrt{C}$)**	**ANCE ($C' = f(C)$)**	**Unsharp filtering (σ=0.2)**	**Adaptive Unsharp filtering**	**Homomorphic filtering**	**Median filtering (3x3 neighborhood)**
CII	μ	1	1.128	1.393	2.485	2.472	1.550	1.060	1.269	3.287	0.575	0.905
	σ	1	0.126	0.156	0.265	0.312	0.709	1.115	0.039	1.965	0.433	0.029
BNL	μ	0.082	0.115	0.116	0.209	0.206	0.009	0.065	0.099	0.153	0.002	0.08293
	σ	0.049	0.034	0.025	0.058	0.079	0.000	0.001	0.057	0.058	0.002	0.04857
PSNR	μ	5.472	3.505	3.797	2.958	5.963	1.376	1.330	6.768	5.748	4.970	4.941
	σ	3.588	1.366	2.136	2.478	8.733	3.183	1.572	4.434	3.702	3.233	3.384
ASNR	μ	3.892	2.833	3.018	2.691	4.903	0.052	0.547	3.887	4.000	3.615	3.503
	σ	2.478	0.969	1.247	1.900	5.650	1.644	0.866	2.279	2.508	2.286	2.350

The background noise level was inferior to the original image in the ANCE method and homomorphic filtering and had a similar value in median filtering. However this parameter had a higher value in all the other techniques implemented. This may be due to the enhancement of some breast tissue, existent surround the breast lesions. Those structures correspond to the background of the breast lesions, regarding the BNL calculation and any enhancement in the background increases the background noise level. In the case of unsharp masking, another motive to this high value in the BNL corresponds to the ringing artifact, which is a fake signal near the edge transition, appearing as a white band.

The PSNR and ASNR were only higher than the original image in unsharp and adaptive unsharp filtering and for the non-linear contrast stretching. Nevertheless, the enhancement of some breast tissue may also difficult the segmentation techniques, as it may disguise the microcalcification enhancement.

Thus, a trade-off between the enhancing breast lesions contrast and avoiding excessive noise needs to be performed in order to obtain a further correct segmentation.

The results obtained are consistent with the ones that have been reported in several papers, such in (Chan, Vyborny, MacMahon, Metz, Doi, & Sickles, 1987) in which the application of the unsharp masking for digital mammography was investigated, and was verified that the method proved increased the noise causing some artifacts in the images.

The study described in (Sivaramakrishna, Obuchowski, Chilcote, Cardenosa, & Powell, 2000) compared the performance of several contrast enhancement algorithms: adaptive unsharp masking, contrast-limited adaptive histogram equalization, adaptive neighborhood contrast enhancement, and wavelet-based enhancement. The authors concluded that appropriate image enhancement improves the visibility of microcalcifications. In a majority of the cases with microcalcifications, the ANCE algorithm provided the most-preferred images. This is consistent with the results obtained in our test, in which it was possible to observe that this technique did not introduce additional noise, and even removed some of the original noise. However, the computational demanding of this technique is too high, which precludes the test of this enhancement technique with the segmentation operations that are further described. Morrow et al. (1992) also described effectiveness of region based contrast enhancement in posterior detection of calcifications in the mammogram, enhancing the detection accuracy even in dense breast tissue.

A lesion in dense breasts, which corresponds to bright area in mammography, is one of the most common causes for non-detection of breast lesions. Despite not represented in the numerical or in the visual results provided in this thesis, adaptive unsharp filtering and CLAHE enhancing allowed, in general, the reduction of bright areas in the breast, enabling a further identification of possible breast lesion in those dense breasts. Thus, the enhancement of dense breasts is a very important step in an image detection system, as it may reduce undetected microcalcifications. Undetected microcalcifications in dense breast are responsible for several not detected breast cancers.

Concluding, the enhancement algorithms presented, in general, increases the contrast ratio when compared with the original image but increased the background noise level and decreased the signal to noise ratio. The algorithms implemented and tested with best relations between CII, BNL, PSNR, ASNR, and consequently providing enhancing image contrast for the best visualization, corresponds to CLAHE with linear and the Rayleigh distribution, linear contrast stretching and non–linear contrast stretching with *gamma* equal to 2, unsharp filtering, adaptive unsharp filtering and ANCE. Some of those algorithms had very similar results. For testing the enhancement influence in segmentation algorithms, some algorithms of had to be chosen: CLAHE with Rayleigh distribution, linear contrast stretching and adaptive unsharp filtering. This choice was performed in order to have one algorithm of each technique with the best results. ANCE algorithm was excluded due to it computational expense, being impractical for posterior studies of image segmentation.

5.2. Segmentation

The step which commonly follows the image enhancement is image segmentation. Segmentation, for the context of this work, corresponds to the division of the original image into segments. This division is a crucial requisite in further image analysis tasks (Rangayyan R. , 2005).

A radiologist may recognize structural components of a breast tissue in a mammogram by just observing it. However, a computational analysis of the same image requires algorithmic analysis of its pixels before conclude about the structural components of the breast tissue represented (Rangayyan R. , 2005).

Image segmentation techniques, as mentioned in section 4.2, include thresholding techniques, edge based methods and region based methods. The segmentation techniques can be combined and performed together, being denominated hybrid techniques (Rangayyan R. , 2005).

The implemented algorithms of image segmentation and their results are described and analyzed in this section. The numeric evaluation of the segmentation results was performed according to some of the parameters specified in section 3.2.1.

For the aim of this work, detections are considered as true positive if occurs superimposing by more than 1 (one) pixel of the detection object with an existent microcalcification in the mammogram. False positive detections correspond to detections higher than 1 (one) pixel in the breast area which did not superimpose an existent microcalcification. False negative is the absence of detection of existent microcalcifications in the mammogram. True negative corresponds to the remaining pixels in the breast area which were not classified and didn't correspond to existent microcalcifications.

The parameters of sensitivity, specificity, accuracy, precision and F-measure were calculated with the FP, FN, TP, TN values according to equations 3.1, 3.2, 3.3, 3.4 and 3.5, respectively. Degree of overlap was also calculated, which corresponds to the ratio between the intersection and the union of the detected true positive microcalcifications with the existent microcalcifications.

Those parameters were calculated based on the implementation of the following techniques in twenty mammographic images chosen from the mini-MIAS database.

5.2.1. Adaptive Threshold

Thresholding methods, as previously clarified in section 4.2.1, are based upon the assumption that pixels whose values lie within a defined range belong to the same class. The applied algorithm was based on the one proposed in (Wellner, 1993) and corresponds to an adaptive threshold that calculates a moving average of pixels along the image. The image is scanned as it were a single row of pixels composed of all the rows in the image lined up next to each other. The sum of the values of the last s pixels at point n is calculated through:

$$f_s = \sum_{i=0}^{s-1} p_n - 1. \tag{5.7}$$

When the value of the pixel being analyzed, p_n, is considerably lower than the median or the Gaussian of the filtered image is set black (one). In all the remaining cases, it is set white (zero):

$$T\ (n) = \begin{cases} 1 & p_n < \frac{f_s\ \times (100-t)}{100\ s} \\ 0 & otherwise \end{cases}. \quad \textbf{(5.8)}$$

The value of t expresses the percentage relative to the local average gray level below the local threshold is set. $f_s(n)$ corresponds to the sum of the values of the last s pixels at point n:

$$f_s\ (n) = \sum_{i=0}^{s-1} p_{n-i}. \quad \textbf{(5.9)}$$

The results of this segmentation were intersected with the breast area of the image in order to avoid artifact due to mammographic digitalization. The breast section detection was developed with non-linear contrast stretching, with *gamma*=0.3 from equation 5.1, followed by a median filtering of a 3x3 neighborhood in order to smooth the breast region to ease the segmentation operations. The highest sized object was then select, whereas the remaining objects were discarded. This allowed the preservation of the shape and size of the breast.

The flow chart of the breast section algorithm is represented in Figure 5.15, and the flow chart of the entire adaptive threshold technique implemented is represented in Figure 5.16.

The segmentation algorithm was tested with and without enhancement. The enhancement techniques tested, as previously mentioned, were: contrast stretching equalization, adaptive unsharp masking and contrast-limited adaptive histogram enhancement.

Figure 5.17 represents a result of the application of the adaptive thresholding to a real mammographic image for all the tested cases.

The efficiency of any segmentation algorithm is very dependent on its parameters set. Several t values and window size, s, were tested, as represented in Table 5.9. It was also chosen if the value of the pixel being analyzed was compared with the median or with the Gaussian filtered image.

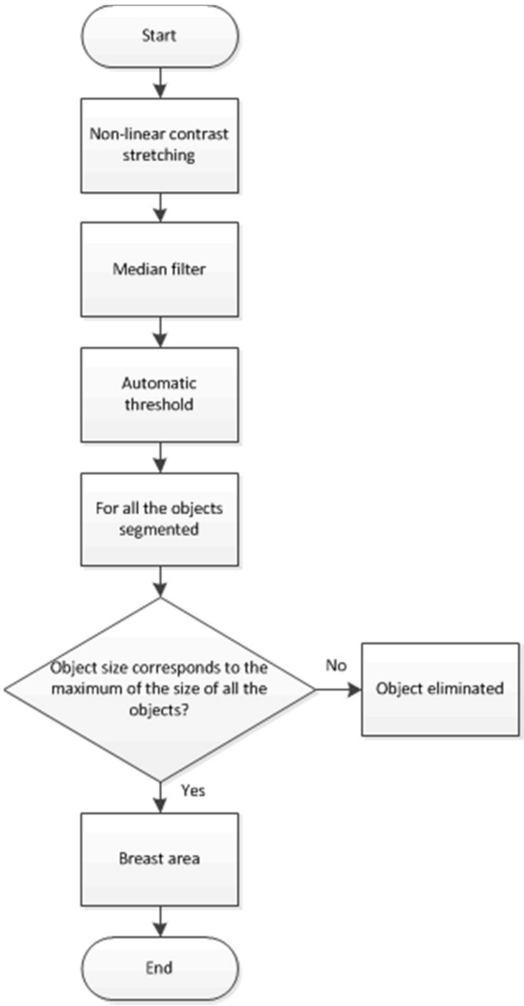

Figure 5.15 – Flow chart of the breast section detection algorithm developed.

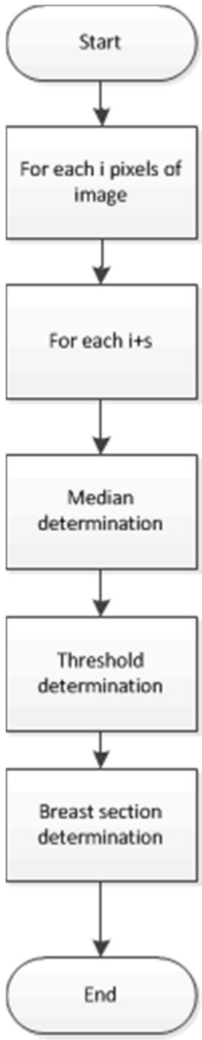

Figure 5.16 – Flow chart of the adaptive threshold technique.

For high window size, the algorithm will approximate the adaptive threshold to a regular threshold, as it will compare with a higher region of the image. However, if the window size is too small, the algorithm will not have enough pixels' information to adapt adequately to the regions. For a window of 10x10 pixels size, the number of microcalcifications detections is inferior to the one of 15x15 pixels, which is on the other hand inferior to the ones for 18x18 pixels. The number of TP is increased, whereas the FN is decreased and the values of FP are also increased. For higher values of this percentage, exemplified with 25x25 pixels, the number of TP are not significantly increased, or the FN significantly decreased. Still, the number of FP detections is highly increased. Therefore, while the sensitivity is increased, the specificity, accuracy and precision are decreased. As accuracy corresponds to the global performance of the algorithm and precision to the fraction of relevant detections and suffered a decrease, a balance had to be performed between the existence of true positive detections and higher percentage of false positive detections. Thus, the value chosen for this window size was 15x15 pixels, as it also corresponds to the value with highest F-measure, the balance between precision and sensitivity.

A similar situation occurred when this algorithm was performed with the comparison of the threshold with the Gaussian filtered image, instead of the median. Thus, despite the sensibility be increased, the other evaluation parameters were further decreased.

Consequently, the experiments were then performed with comparison of the threshold with the median filtered image.

Table 5.9 – Evaluation parameters of the adaptive thresholding technique for the different parameters.

	Median, window size=10, t=18	**Median, window size 15, t=18**	**Median Window size=25, t=18**	**Gaussian window size=15, t=18**	**Median window size=15, t=10**	**Median window size=15, t=14**
FP	86	152	301	570	797	289
FN	40	29	24	20	9	17
TP	41	50	46	49	63	61
TN	7695947	7721430	7684229	7142418	7533301	7676098
Sensitivity	0.506	0.633	0.657	0.710	0.875	0.782
Specificity	0.999	0.999	0.999	0.999	0.999	0.999
Accuracy	0.999	0.999	0.999	0.999	0.999	0.999
Precision	0.323	0.248	0.133	0.079	0.0733	0.174
F-measure	0.394	0.3559	0.221	0.142	0.135	0.285
Degree Overlap	0.156	0.224	0.147	0.004	0.119	0.121

When the threshold had a value too high, some microcalcifications were not detected, whereas when the threshold had a value too low, as represented in Table 5.9 with *t* equal to 14, excessive false positives were detected. Hence, a similar balance had to be achieved, and the best value found for of this parameter was equal to 18.

As a result, the algorithm with the parameters set detected the majority of microcalcifications existent in the mammograms; nonetheless, it had some false positive detections in the regions with similar gray level value to the breast lesions.

The algorithm with the set parameters was tested with image enhancement techniques in order to evaluate the influence of this operation in the segmentation of the breast images, Figure 5.17.

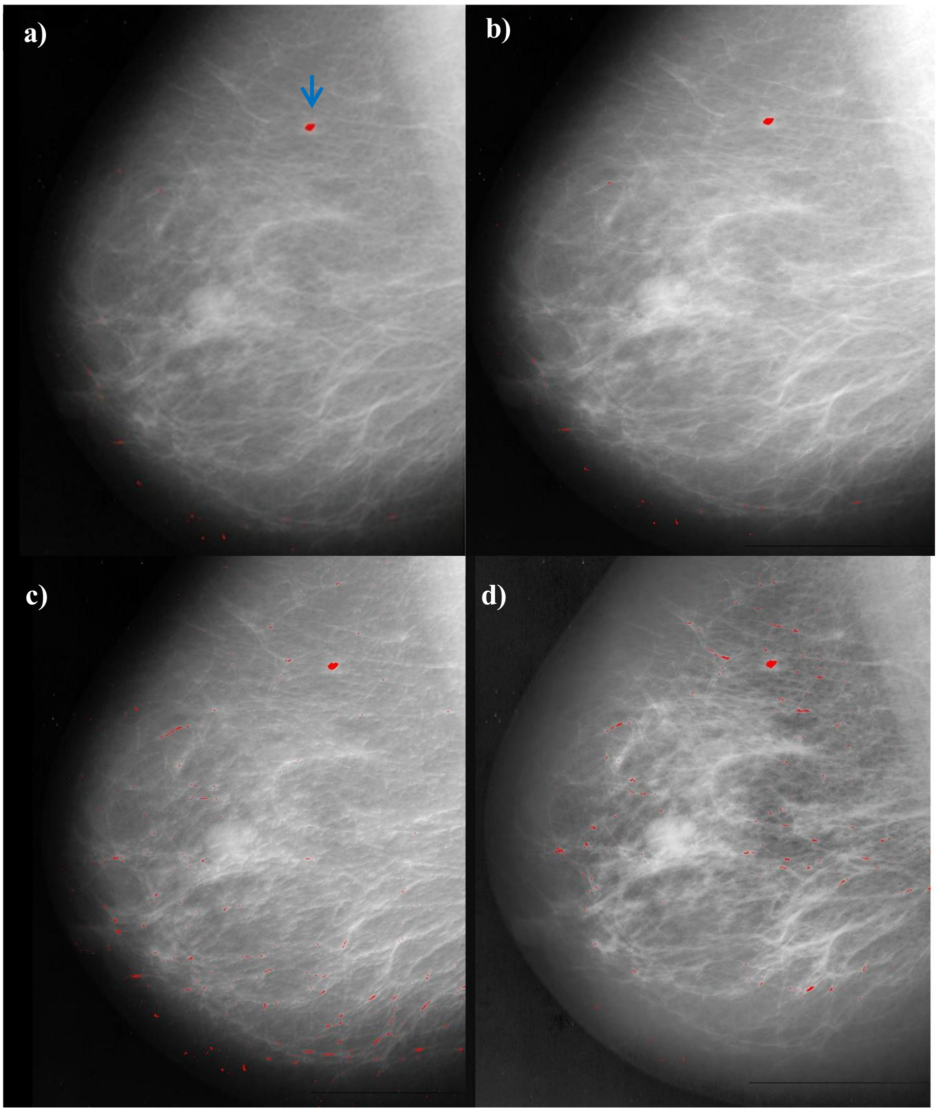

Figure 5.17 - Result of an adaptive threshold on a mammographic image: a) no previously image enhancement, b) previously linear contrast stretching, c) previously adaptive unsharp, d) previously CLAHE with Rayleigh distribution (The red dots indicate the regions detected. The blue arrow indicates the local of the real microcalcification in the mammogram, exemplified only in the first image).

It should be noticed that in some cases the TP maintained the value, whereas the FN varied. This occurred because the algorithm of segmentation can detect a microcalcification where there is a cluster of microcalcifications. In this case, all the microcalcifications in the cluster are considered detected. The opposite can also be true: a higher sized calcification can be detected twice by the segmentation algorithm, indicating the presence of two microcalcifications when only one is present.

Table 5.10 – Evaluation parameters of the implemented adaptive thresholding technique.

	No enhancement	After contrat stretching	After Adaptive Unsharp	After CLAHE
FP	152	253	900	713
FN	29	27	13	13
TP	50	50	64	62
TN	7721430	7688739	7495738	7827772
Sensitivity	0.633	0.649	0.831	0.827
Specificity	0.999	0.999	0.999	0.999
Accuracy	0.999	0.999	0.999	0.999
Precision	0.248	0.165	0.066	0.082
F-measure	0.356	0.263	0.123	0.146
Degree Overlap	0.177	0.182	0.124	0.158

After contrast stretching, Table 5.10, the number of false positives increased to more 100 FP detections, while the FN decreased only by 2 microcalcifications. As the fibroglandular tissue was also enhanced, as mentioned in section 5.1.2, the PSNR enhanced, allowing the introduction of more positive incorrect detections, while few additional microcalcifications were detected. The degree of overlap of the detected microcalcifications and the real ones was slightly increased. After adaptive unsharp filtering, 14 additional microcalcifications were correctly detected. However, there was a vast increase of the number of false positive detections, induced due to an adaptive enhancement of the high frequency patterns which corresponded not only to the microcalcification, but also to the remaining breast tissue enhancement. There was also a significant decrease of the region of overlap. CLAHE did not detect the same number of microcalcifications in the images as the adaptive unsharp filtering, whereas the FP was about 1.25 times inferior. This allowed a similar sensitivity, with a higher specificity, accuracy and F-measure. The degree of overlap had a value between the results of no enhancement and after unsharp filtering. These results occurred due to the Rayleigh histogram distribution of CLAHE, which enhanced with higher intensity the gray areas, where the microcalcifications gray level were located, while stretched the remaining gray levels, separating them.

The majority of the not detected microcalcifications corresponded to microcalcifications in dense breasts or to small sized microcalcifications.

In CAD terms, the most important feature corresponds to the correct detection of the microcalcifications, as it reduces the possibility of the absence of notice of the microcalcification and thus the detection of possible breast disease associated. However, a too high level of FP reduces the lack of confidence of the radiologist on the CAD system. Thus, in order to reduce the FP detections and increase the F-measure, morphological operations were performed following the adaptive threshold.

5.2.2. Adaptive Threshold and Morphological Operations

Adaptive threshold by itself implies very false positive detection. The implementation of morphological operations posteriorly to adaptive threshold may reduce those false positive (Nesbitt, Aghdasi, Ward, & Morgan-Parkes, 1995).

The adaptive threshold technique used was the one previously mentioned in section 925.2.1.

The result of this operation was then eroded in parallel with structural elements 3x3 rotated in 90º each, S_1, S_2, S_3 and S_4:

$$S_1 = \begin{bmatrix} 0 & 1 & 0 \\ 1 & 1 & 0 \\ 0 & 0 & 0 \end{bmatrix}, \quad S_2 = \begin{bmatrix} 0 & 1 & 0 \\ 0 & 1 & 1 \\ 0 & 0 & 0 \end{bmatrix}, \quad S_3 = \begin{bmatrix} 0 & 0 & 0 \\ 0 & 1 & 1 \\ 0 & 1 & 0 \end{bmatrix}, \quad S_4 = \begin{bmatrix} 0 & 0 & 0 \\ 1 & 1 & 0 \\ 0 & 1 & 0 \end{bmatrix}. \quad \textbf{(5.10)}$$

The structure of those elements was suggested by (Nesbitt, Aghdasi, Ward, & Morgan-Parkes, 1995). This process allowed the removal of small objects which may correspond to artifacts in the segmented image.

The whole process is presented in Figure 5.18 as a flow chart.

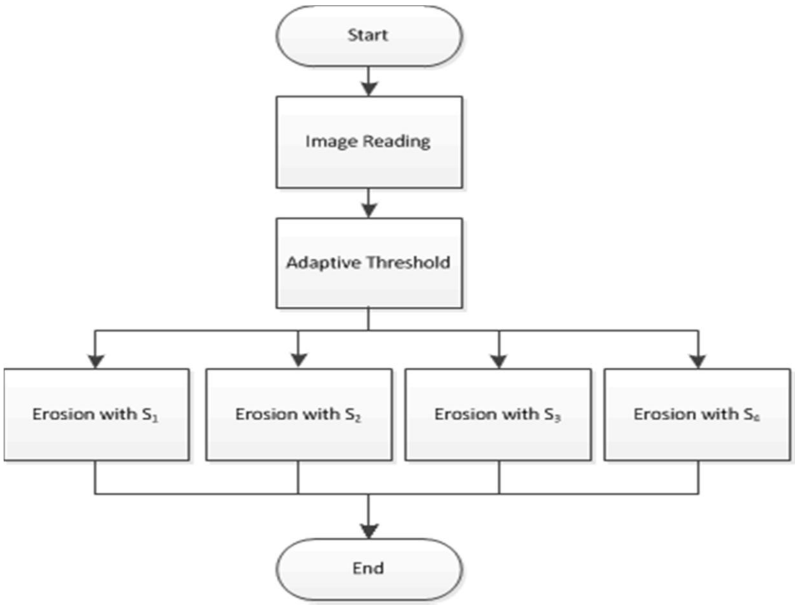

Figure 5.18 – Flowchart of the implemented algorithm of adaptive threshold and morphological operators.

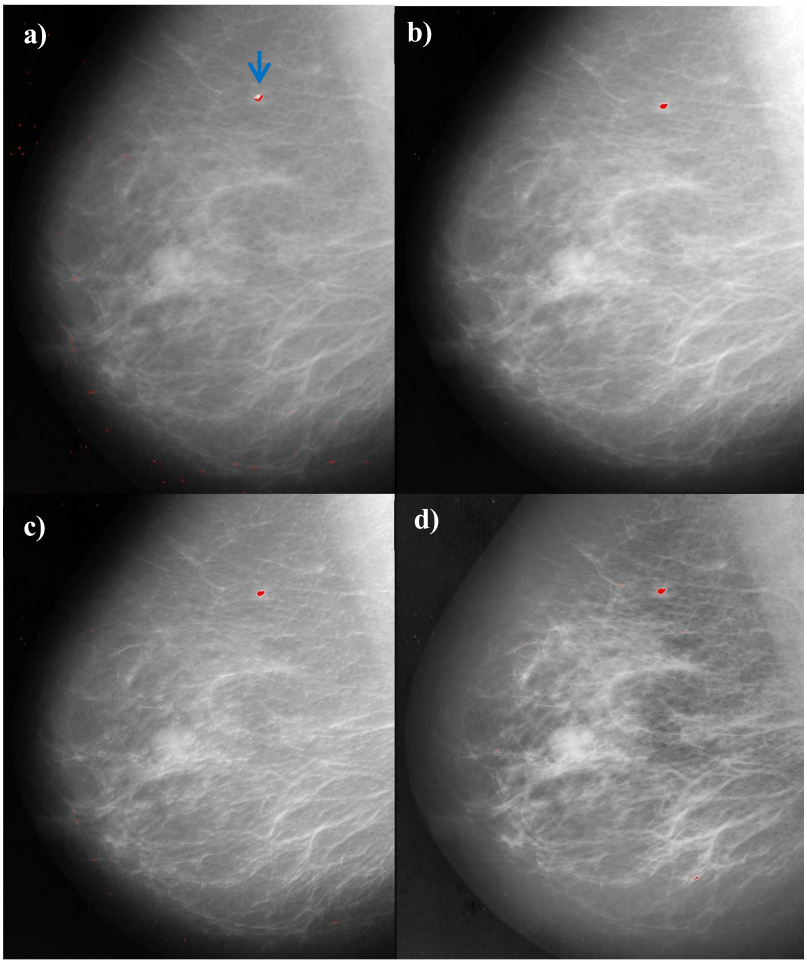

Figure 5.19 – Result of adaptive threshold on a mammographic image with posterior morphological operations: a) no previously image enhancement; b) –d) segmentation after enhancement: b) linear contrast stretching, c) adaptive unsharp filtering, d) CLAHE with Rayleigh distribution. (The red dots indicate the region detected with the algorithm, while the blue arrow, represented only in a), indicates the local of the real microcalcification in the mammogram).

Table 5.11 – Evaluation parameters of adaptive thresholding and morphological operators.

	No enhancement	**After contrast stretching**	**After Adaptive Unsharp**	**After CLAHE**
FP	42	43	68	31
FN	51	52	48	37
TP	26	25	29	41
TN	7762108	7766251	7782347	8020535
Sensitivity	0.338	0.325	0.377	0.526
Specificity	0.999	0.999	0.999	0.999
Accuracy	0.999	0.999	0.999	0.999
Precision	0.383	0.368	0.299	0.569
F-measure	0.359	0.345	0.333	0.547
Degree Overlap	0.103	0.106	0.113	0.145

The implemented algorithm, when compared with the adaptive threshold alone, reduced notoriously the FP detection, not only for the mammograms with no enhancement, but also for all the enhancement techniques implemented. This occurred due to the erosion of the segmented objects resultant from the previous algorithm with the structural elements represented, aiming the elimination of small objects with less than 3 pixels of size as an effort to reduce the false positive rate.

Unfortunately, this erosion also deleted some objects that corresponded to real microcalcifications, with a consequence decreasing of the TP detections and a reduced sensitivity. Nonetheless, occurred a noticeable increase in the specificity, accuracy, precision and F-measure.

Different enhancement methods prior to the image segmentation were tested. Contrast stretching induced few improvements in the detection of microcalcifications and no increase in the FP detection when compared with no image enhancement.

Adaptive unsharp enhancement allowed a slight reduction of the non-detected microcalcifications resulting in an increase in the detection of non-existent microcalcifications, causing a slight increase in the sensitivity and a slight decrease in the specificity, accuracy, precision and F-measure.

CLAHE reduced the FP detections, when compared with the other enhancement techniques, with the non-enhancement and with the no existence of morphological operations, as occurred in the previous section. The number of non-detected microcalcifications was reduced, compared both with the other enhancements and no enhancement. Thus the sensitivity, specificity, accuracy, precision and F-measure were higher with this previous enhancement. However, the sensitivity was lower when compared with the segmentation with no posterior morphological operations. Thus CLAHE enhancement provides a better segmentation with this algorithm when compared with no enhancement.

Higher structural elements implied more reduction of the false positive detections of microcalcifications, while reducing also the detection of existent microcalcifications.

5.2.3. Threshold and Difference of Gaussians

In order to improve the detection of microcalcifications in the mammographic images, other method was implemented. It has some similarities with the one proposed in (Näppi & Dean, 2000), nevertheless the parameters and connection between the procedures were newly developed. This technique is initialized with an adaptive threshold, whose procedure is similar to the one described in section 5.2.1. As a parallel method, the original image is filtered using Gaussians filters. Thus, the image is subtracted from itself filtered with a 15 x 15 low-pass Gaussian filter, G_1. This allows the detection of the high frequency components of the image, characterized by image sharp changes, operating as a high-pass filter. This result is then filtered with a 5 x 5 high-pass Gaussian filter, G_2, which allows obtaining the sharpener edges, which probably contain calcifications. Different values of mask size and standard deviation of both filters were experimented, as indicated in Table 5.12. The result of this procedure is then threshold based on statistics of the image (average of the image, μ, image standard deviation, σ, and image maximum value, *max*), according to:

$$T = \begin{cases} \mu + 4\sigma & if\ 4\,\sigma > 0.2\ (\max - \mu) \\ \mu + 0.2(max - \sigma) & otherwise \end{cases} \quad . \qquad \textbf{(5.11)}$$

The final image is computed from the intersection of this procedure and the adaptive threshold result, as represented in the flowchart of Figure 5.20.

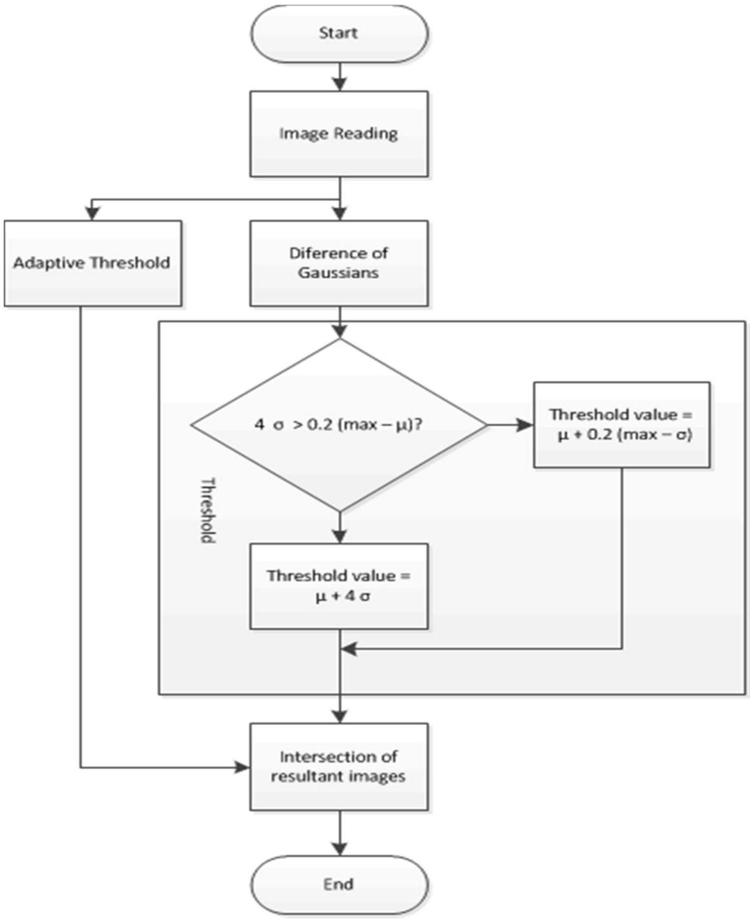

Figure 5.20 – Flow chart of the algorithm implemented of threshold and difference of Gaussians.

Table 5.12 – Evaluation parameters of threshold and difference of Gaussians.

	G_1: 10x10, σ_1=0.7 *G2:* 5x 5, σ_2=0.5	*G_1:*15x15, σ_1=0.7 *G2:* 5x 5, σ_2=0.5	*G_1:* 20x20, σ_1=0.7 *G2:* 5x 5, σ_2=0.5	*G_1:*15x15, σ_1=0.5 *G2:* 5x 5, σ_2=0.7	*G1:15x15, σ1=0.9 G2: 5x 5, σ2=0.5*	*G_1:*15x15, σ_1=0.7 *G2:* 5x 5, σ_2=0.9
FP	45	41	45	40	54	80
FN	33	26	33	34	26	30
TP	44	51	44	43	51	47
TN	7762299	7762353	7762732	7762536	7761974	7761035
Sensitivity	0.571	0.662	0.571	0.558	0.662	0.610
Specificity	0.999	0.999	0.999	0.999	0.999	0.999
Accuracy	0.999	0.999	0.999	0.999	0.999	0.999
Precision	0.494	0.554	0.495	0.518	0.4857	0.371
F-measure	0.530	0.604	0.530	0.538	0.560	0.461
Degree overlap	0.086	0.116	0.086	0.105	0.126	0.176

From Table 5.12, it is possible to verify that decreasing the mask size of the first Gaussian filter applied, exemplified for a 10x10 Gaussian filter, the FP detections were higher and the TP detections were inferior, implying inferior sensitivity, specificity, accuracy, precision and F-measure. For a value superior to 15x15 Gaussian filter, the same occurred and the identical values were obtained.

The standard deviation of the Gaussian filter changes the influence that the distance of each coefficient has on the central pixel. Higher values blur the edges in the image, whereas, lower values implies a higher blur of the image. As this filtered image is subtracted from the input image, it implies the passage of the highest image frequency components, while higher standard deviations imply more blur in the low-pass filtered. Consequently, in the subtracted image occurs a higher enhancement of image details with medium frequency, as higher frequency components were attenuated.

Hence, a low standard deviation implies fewer microcalcification detections, whereas high values imply higher percentage of microcalcification and false positive detections, as can be verified from Table 5.12. The value with higher sensibility and specificity and consequently F-measure, corresponded in our experiments to a standard deviation equal to 0.7.

Both Gaussian filters were used, since the subtraction of one image with high frequency enhancement from the other preserves spatial information that lies between the ranges of frequencies of the filters. Filters with σ_1 higher than 0.7 decreased the detection of microcalcifications as it interferes in the frequency of the microcalcification. Filter with σ_1 inferior to that value increased the detection of false positive detections as it allows the enhancement of more frequencies. However, there are other structures besides microcalcifications with similar frequencies, which allow the existence of false positive detections. Some microcalcifications have also different frequencies from the usual range due to a similar background, for example, which difficult its detection.

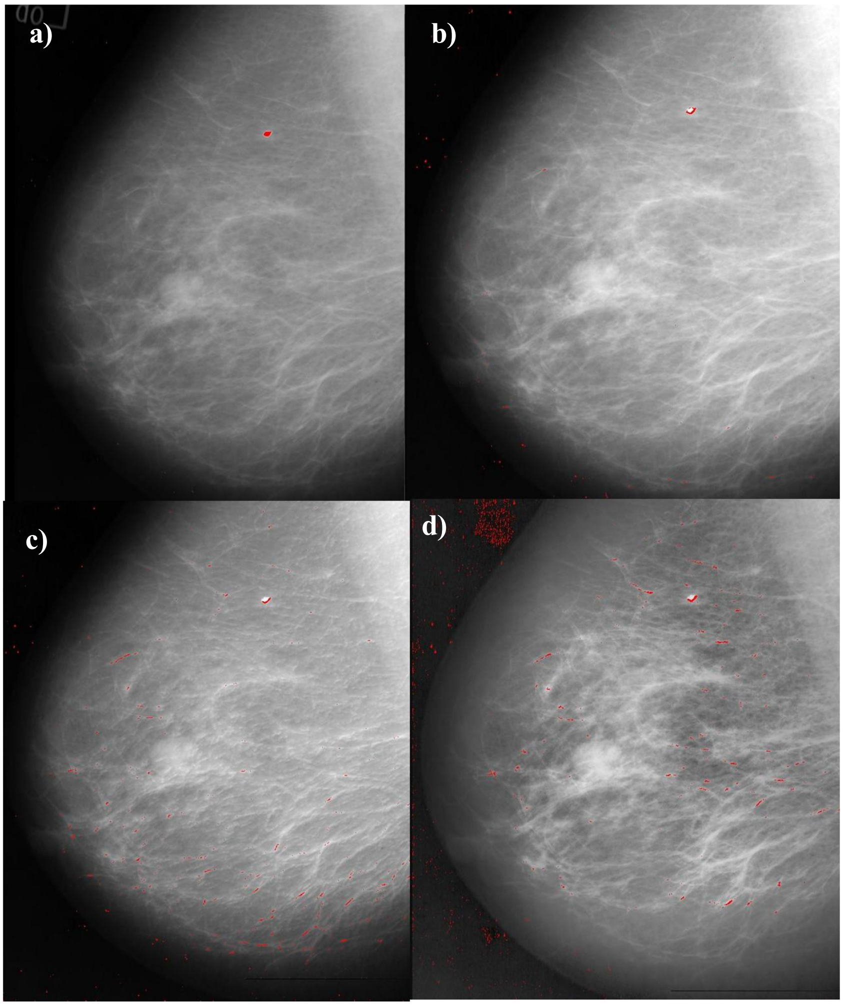

Figure 5.21 – Result of the algorithm of threshold and difference of Gaussians on a mammographic image: a) no previously image enhancement; b) –d) segmentation after enhancement using: b) linear contrast stretching, c) adaptive unsharp filtering, d) CLAHE with Rayleigh distribution. (The red dots indicate the region detected by the algorithm, while the blue arrow, represented only in a), indicates the local of the real microcalcification in the mammogram).

Figure 5.21 and Table 5.13 indicates the results from the implementation of the algorithm with previous image enhancement. Contrast stretching prior to segmentation increased the false negative rate when compared with no enhancement, while maintaining the false positive, as it distributes the gray level values, which approximates the gray level values of fibroglandular breast tissue from the microcalcifications, difficulting the detection.

Adaptive unsharp filtering allowed the detection of more existent microcalcifications in the mammogram. However, it also increased by two times the detection of non-existent microcalcifications. As this algorithm enhances the sharp variations in the image, not only microcalcifications were enhanced, but also some additional breast tissue, which introduced the false positive detections.

Table 5.13 – Evaluation parameters of thresholding and difference of Gaussians with previous enhancement. The Gaussian filter has the following parameters: G_{1}: 15x15, σ_1=0.7 and G_2: 5x 5, σ_2=0.5.

	No enhancement	After contrast stretching	After Adaptive Unsharp	After CLAHE
FP	41	41	109	233
FN	26	30	22	14
TP	51	49	56	62
TN	7762353	7762353	7782958	8030283
Sensitivity	0.662	0.620	0.718	0.816
Specificity	0.999	0.999	0.999	0.999
Accuracy	0.999	0.999	0.999	0.999
Precision	0.554	0.544	0.339	0.210
F-measure	0.604	0.580	0.461	0.334
Degree overlap	0.116	0.091	0.071	0.114

Contrast stretching increased even further the detection of real microcalcifications; however, with the disadvantage of a considerable higher number of detections of inexistent microcalcifications in the mammogram. Thus, while the sensitivity of the algorithm was increased, the precision and accuracy were decreased.

No enhancement of the images corresponded to the algorithm with higher values of specificity, accuracy, precision and F-measure, being the third in terms of sensitivity due to fewer true positive detections, but less false positive detections. Consequently, in this algorithm, the best detection corresponds to the one with no previous enhancement.

5.2.4. Region Growing of selected areas

Region based methods are defined on the knowledge that neighboring pixels within a region have similar values. Region growing is a procedure that, as the name implies, groups pixels into regions. This method starts with a seed pixel and grows a region by appending spatially connected neighboring pixels that meet a certain homogeneity criterion (Rangayyan R. , 2005).

The application of a region growing algorithm for all the pixels in the image corresponds to a very demanding computationally methodology. Commonly, the region growing algorithm is performed examining the neighborhood of the seeds that are interactively set by the users. However, this approach is not an autonomous solution. Thus, an alternative corresponds to application of region growing to pre-segmented areas in order to obtain the correct shape and dimensions of the breast lesions.

Therefore, the implemented technique of region based segmentation has several steps. The first corresponds to threshold the image adaptively, with the same parameters as specified in section 5.2.1. The result of this adaptive threshold is intersected with the area correspondent to the breast in the mammography, as depicted by Figure 5.15, so that detected objects outside this region are eliminated.

The region growing algorithm is then executed, considering as seed the middle of the detected objects. The region growing algorithm applied was based on the one proposed in (Kroon D. , 2008), where the region is iteratively grown through the comparison of the unallocated neighbor pixels to the region using as criterion of similarity the difference between the pixel's intensity value and the region's intensity mean. The pixels are considered belonging to the region if this difference is inferior to 0.01. This value was set after several experiments. As lower the threshold, stricter is the criterion of similarity. This process ends when the intensity between the surrounding pixels and the region mean is higher than the threshold.

The flowchart of the implemented region based algorithm is represented in Figure 5.22 and the results are presented in Figure 5.23 and Table 5.14.

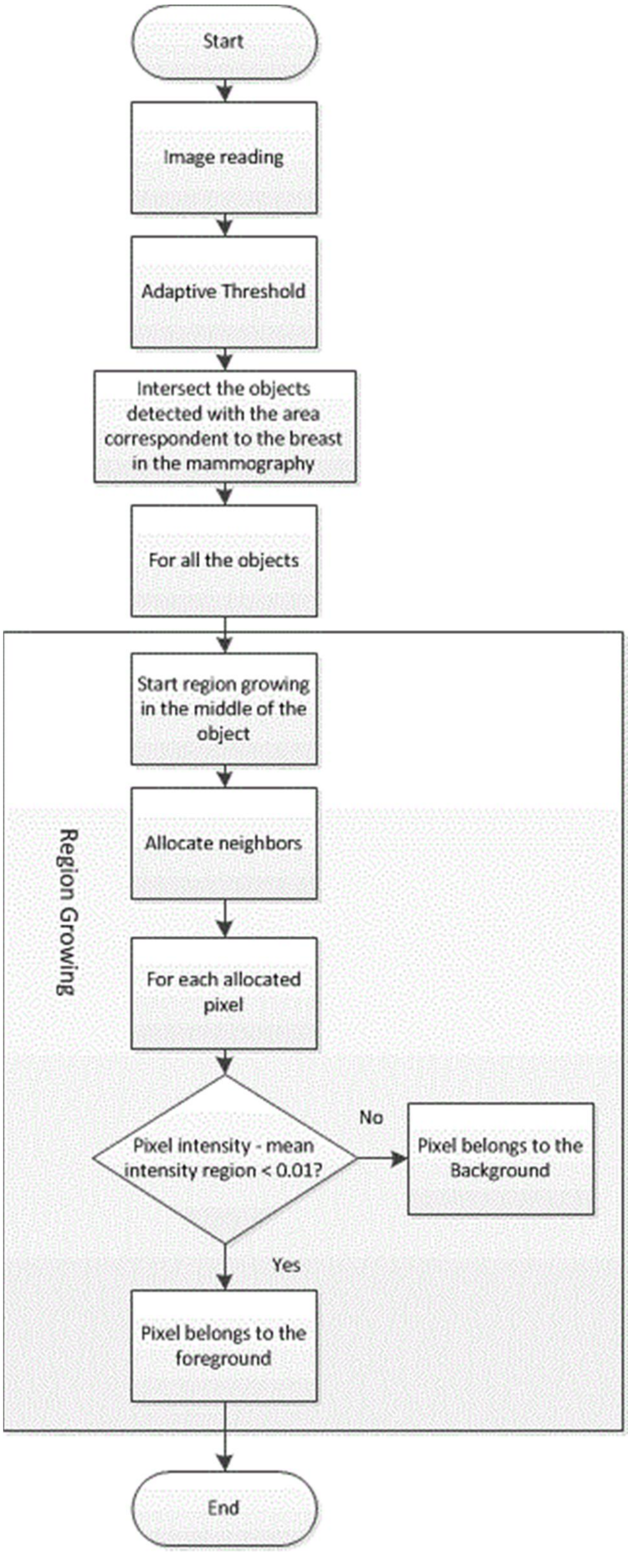

Figure 5.22 – Flowchart of region based segmentation algorithm.

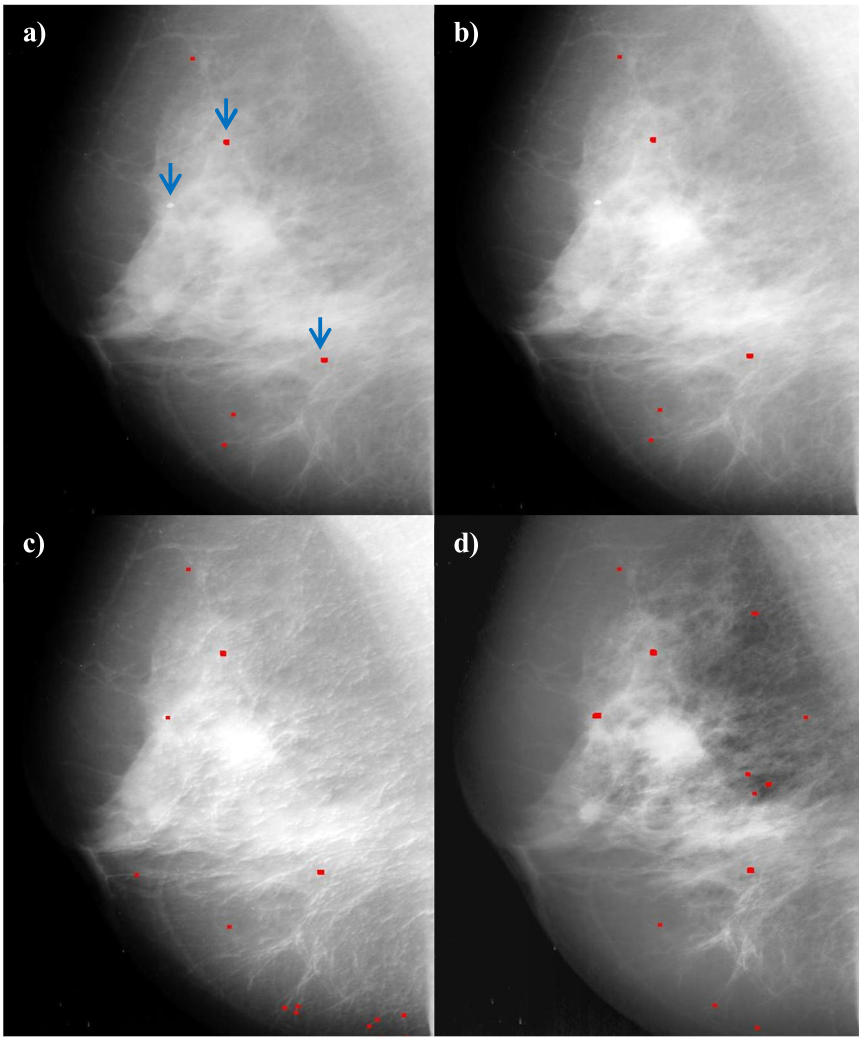

Figure 5.23 – Result of the region growing of selected areas algorithm: a) no previously image enhancement; b) –d) segmentation after enhancement: b) linear contrast stretching, c) adaptive unsharp filtering, d) CLAHE with Rayleigh distribution. (The red dots indicate the region detected by the algorithm, while the blue arrows, indicated only in the first image, provide the location of the real microcalcifications).

Table 5.14 – Evaluation parameters of the implemented region growing based technique.

	No enhancement	After contrast stretching	After Adaptive Unsharp	After CLAHE
FP	195	216	359	400
FN	22	27	16	11
TP	53	48	58	60
TN	7758483	7758869	7775952	8024136
Sensitivity	0.707	0.646	0.783	0.845
Specificity	0.999	0.999	0.999	0.999
Accuracy	0.999	0.999	0.999	0.999
Precision	0.218	0.182	0.139	0.130
F-measure	0.327	0.283	0.236	0.226
Degree overlap	0.389	0.334	0.286	0.335

This implementation provided a sensitivity of 70%. However, this algorithm is very dependent on the initial objects segmented which will be subject of the region-growing procedure.

Contrast stretching prior to region growing based detection, Table 5.14, reduced the detection of real microcalcifications, whereas slightly decreased the FP detections. Thus sensitivity, precision and F-measure were inferior to the results with no enhancement. Adaptive unsharp and CLAHE filtering, despite increasing the FP detections when compared with no enhancement, reduced the non-detection of existent microcalcifications. This fact enabled the increasing of sensitivity, but also allowed the decreasing in specificity, accuracy, precision and F-measure. The degree of overlap of the detected microcalcifications with the existent microcalcifications had a similar value for the results with no enhancement, and for the results with previous adaptive unsharp filtering and CLAHE. Consequently, the best performance of the algorithm has no initial image enhancement.

5.2.5. Edge detection

Edge based techniques are founded on the property that, generally, pixel values changes rapidly at the edges between regions. Thus, these methods detect intensity discontinuities on the edges between objects and their backgrounds using a gradient operator. High values of the output correspond to a possible edge. However, it can also correspond to noise also, as it has, as well, a quick change of gray values, difficulting the edge based detections.

Some edge detection methods were tested: Prewitt, Sobel and Roberts, whose results are indicated in Table 5.15. The edges were detected for all the methods in both horizontal and vertical directions in the image. The edges were then intersected with the breast area as depicted in Figure 5.15, in order to remove eventual artifacts due to the mammographic digitalization. Posteriorly, the edges detected were filled with the use of an algorithm based on morphological reconstruction (Soille, 1999).

Prewitt and Sobel operators find horizontal and vertical edges in an image by getting a higher response in the respective direction, returning the maximum gradients, i.e. above an automatic threshold. The values in the 3x3 masks are correlated with the corresponding pixels' values in the input image. The main difference between Sobel and Prewitt is in the weighting of the middle row/column, vertical and horizontal kernels, respectively. Sobel uses a weighting of 2/-2, whereas Prewitt makes use of 1/-1, which results in higher smoothing as there is given more importance to the central pixel. Roberts' operator has a mask of 2x2 and approximates the gradient of the image through discrete differentiation achieved by the computation of the sum of the squares of the differences between diagonally adjacent pixels, as explained in section 4.2.3.

From Table 5.15, it is possible to verify that Prewitt and Sobel had similar results when applied to detecting the microcalcifications. However, Sobel operator had a higher grade of FP detection, decreasing the accuracy and F-measure. Prewitt operator had inferior detection of TP, but also a very inferior grade of FP detection, implying in a higher value of accuracy and F-measure. Roberts' operator had inferior TP detection, but also very inferior FN detection, which leaded to a superior precision and F-measure.

Due to these results Prewitt's and Roberts' operators were chosen to evaluate the influence of the enhancement in the segmentation, despite Roberts' having a better balance between FP and TP.

Table 5.15 – Evaluation parameters of the edge detection methods.

	Prewitt	Sobel	Roberts
FP	146	178	44
FN	11	10	20
TP	52	53	45
TN	7748205	7746445	7755056
Sensitivity	0.825	0.841	0.692
Specificity	0.999	0.999	0.999
Accuracy	0.999	0.999	0.999
Precision	0.263	0.229	0.506
F-measure	0.398	0.361	0.584
Degree Overlap	0.272	0.264	0.410

Table 5.16 – Evaluation parameters of the Prewitt's edge detector.

	No enhancement	After contrat stretching	After Adaptive Unsharp	After CLAHE
FP	146	127	698	1515
FN	11	19	6	6
TP	52	46	56	53
TN	7748205	7747974	7738784	7939943
Sensitivity	0.83	0.708	0.903	0.898
Specificity	0.999	0.999	0.999	0.999
Accuracy	0.999	0.999	0.999	0.999
Precision	0.263	0.266	0.074	0.033
F-measure	0.398	0.387	0.137	0.065
Degree overlap	0.272	0.251	0.179	0.121

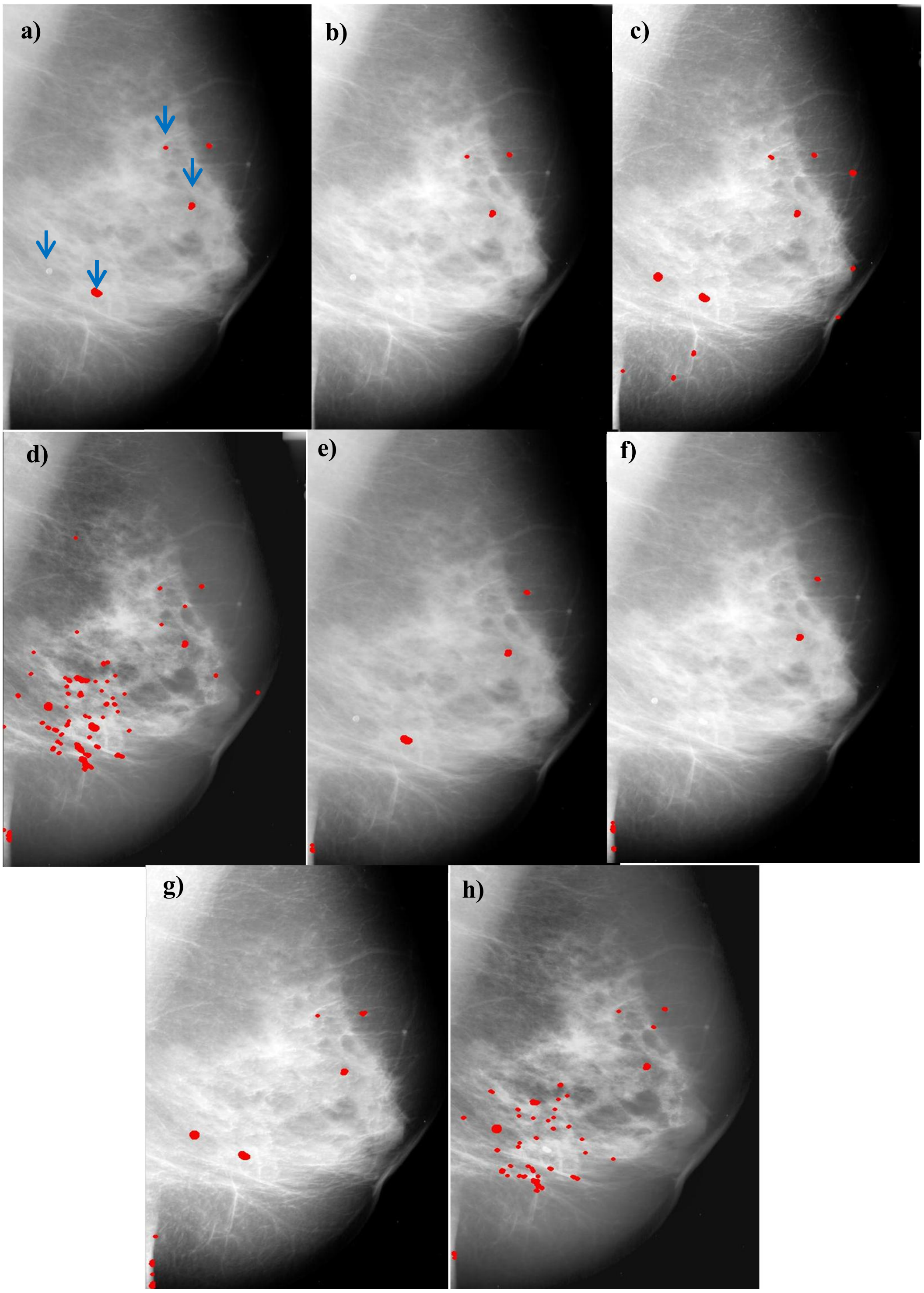

Figure 5.24 – Result of the Prewitt's and Roberts' edge detector on a mammographic image. Prewitt: a) no previously image enhancement; b) –d) segmentation after enhancement using: b) linear contrast stretching, c) adaptive unsharp filtering, d) CLAHE with Rayleigh distribution. Roberts: e) no previously image enhancement; f) –h) segmentation after enhancement using: f) linear contrast stretching, g) adaptive unsharp filtering, h) CLAHE with Rayleigh distribution. (The red dots indicate the region detected with the algorithm, while the blue arrows indicate the location of the real microcalcifications).

Table 5.17 – Evaluation parameters of Roberts' edge detector.

	No enhancement	After contrat stretching	After Adaptive Unsharp	After CLAHE
FP	44	37	270	859
FN	20	23	16	14
TP	45	41	51	48
TN	7755056	7384214	7764421	7978625
Sensitivity	0.692	0.641	0.761	0.774
Specificity	0.999	0.999	0.999	0.999
Accuracy	0.999	0.999	0.999	0.999
Precision	0.506	0.526	0.159	0.053
F-measure	0.584	0.577	0.263	0.099
Degree overlap	0.410	0.367	0.244	0.127

The influence that the enhancement algorithms have on Prewitt's and Robert's segmentation is similar. Contrast stretching prior to the edge based segmentation, as it stretches the gray level values through the entire span of the histogram, approximates the gray level values of fibroglandular breast tissue from the microcalcifications. This results in a decreasing of the variation of the gray level between the object and it neighbor background, which difficult the detection of microcalcifications with the edge-based method. Thus more existent microcalcifications were not detected in both methods, while more FP detections occurred.

Adaptive unsharp masking, on the contrary, allowed a sharpening of the edge regions and consequently of the regions with quick gray level variations, as microcalcifications. This led to a more efficient detection, which can be confirmed from Table 5.16 and Table 5.17, where the FN was reduced and consequently a higher sensitivity of the method was obtained. However, the image sharpening also affects others regions, beyond microcalcifications, with quick variation of gray levels such as noise and some breast structures. This increased the FP detections, implying lower specificity, accuracy, precision and F-measure.

CLAHE provided a similar result when compared with no previous enhancement. However, it had with a notoriously higher percentage of FP detections, providing inferior sensitivity, specificity, accuracy, precision and f-measure. As this enhancement provides a bell-shape distribution, the gray level difference between the microcalcifications and it neighbor background is reduced, reducing the efficiency of the edge-based segmentation method.

Consequently, balancing the sensitivity and the precision obtained, no image enhancement provides a better F-measure value in both cases. However, contrast stretching only slightly reduces this value, as it results are similar to the no enhancement. This occurs for both Prewitt and Roberts' experiments.

5.2.6. Active contour of selected areas

Active contours or "snakes" corresponds to a technique of image segmentation which seeks for local minimum contours. Usually it requires rough coordinates describing the contour of the object. Thus, an initial segmentation of the image is required in order to provide the initial active contour. A similar preprocessing technique to the implemented in the region growing algorithm is applied. Thus, the image is segmented with an adaptive threshold with the same parameters specified in section 5.2.1. The result is intersected with the area correspondent to the breast in the mammography, as described in Figure 5.15. In order to obtain the contour of the objects, a dilation of the objects with a disk structuring element of 2x2 pixels is subtracted to the objects dilated with a disk structuring element of 1x1 pixels. Having those contours, the snake seeks for points which take a minimum energy measure of all the points in the neighborhood. This active contour implementation was based on the one implemented by (Kroon D. , 2008).

The internal energy controls the contour ability to stretch or bend at a specific point. The external forces attract the contour to specific image features (Kass, Witkin, & Terzopoulos, 1988). Thus, the energy functional of a snake can be represented as:

$$E^{*}_{snake} = \int_0^1 E_{int}\,(v(s)) + E_{image}\,(v(s)) + E_{ext}\,(v(s)), \qquad \textbf{(5.12)}$$

where E_{int} represents the internal energy of the snake, E_{image} origins the image forces acting on the curve and E_{ext} represents the external constraint forces (Kass, Witkin, & Terzopoulos, 1988) and *v(s)* the set of points of the snake contour. E_{ext} guides the snake towards away from particular features.

The internal spline energy can be written as:

$$E_{int} = \frac{\alpha(s)|v_s(s)|^2 + \beta(s)\,|v_s(s)|^2}{2} \qquad \textbf{(5.13)}$$

where the first order term, controlled by *α(s),* make the snake function as a membrane, whereas the second order term, controlled by *β(s)*, make the snake act as a thin plate (Kass, Witkin, & Terzopoulos, 1988). High values of *α(s)* increase the internal energy of the snake due to higher stretching, whereas low values of $\alpha(s)$ make the energy function unaffected to the amount of stretch. High values of $\beta(s)$ increase the internal energy of the snake due to the development of more curves, whereas low values of $\beta(s)$ make the energy function unaffected to curves in the snake. Low values of $\alpha(s)$ and $\beta(s)$ place fewer constraints on the size and shape of the snake.

The total image energy, E_{image}, presents three different energy functionals, attracting the snake to lines, edges and terminations (Kass, Witkin, & Terzopoulos, 1988):

$$E_{image} = w_{line}E_{line} + w_{edge}E_{edge} + w_{term}E_{term} \,. \quad \textbf{(5.14)}$$

Adjusting the weight of those energy functionals, a wide range of snakes can be created. Line functional, E_{line}, can correspond to the image intensity. Depending on the w_{line}, the snake is attracted to dark lines or to light lines (Kass, Witkin, & Terzopoulos, 1988):

$$E_{line} = I(x,y) \,. \quad \textbf{(5.15)}$$

Edge functional, E_{edge}, corresponds to the gradient of the image, where the snake is attracted to contour with large image gradients (Kass, Witkin, & Terzopoulos, 1988):

$$E_{edge} = -|\nabla I(x,y)|^{2}. \quad \textbf{(5.16)}$$

The terminations of line segments and corners can be found using a curvature of level lines in a slightly smoothed image. Considering $C(x,y)$ a slightly smoothed image, $\theta = \tan^{-1}\frac{C_y}{C_x}$ corresponds to the gradient angle, $n = (\cos\theta, \sin\theta)$ and $n_{\perp} = (-\sin\theta, \cos\theta)$ are unit vectors along the gradient direction and perpendicular to the gradient direction, respectively. The curvature of the level contours can be represented as:

$$E_{term} = \frac{\partial\theta}{\partial n_{\perp}} = \frac{\partial^2 C/\partial n_{\perp}^2}{\partial C/\partial n}. \quad \textbf{(5.17)}$$

The snake algorithm employed was the one presented in (Kroon, 2010).

Several values for the parameters above specified were tested: w_{line} was set as 0.02 in order to be attracted to white lines, as the microcalcifications; w_{edge} was set as 14 in order to be very attracted to edges, and consequently sharp transitions; w_{term} was set as 0.0001 in order to do not be much attracted to end points; $\alpha(s)$ was set as 2 and $\beta(s)$ set as 0.2 in order to the snake function act more as a membrane than as a thin plate.

Table 5.18 – Evaluation parameters of active contour algorithm.

	No enhancement	After contrast stretching	After Adaptive Unsharp	After CLAHE
FP	195	189	393	307
FN	36	39	58	53
TP	34	32	15	19
TN	7731288	7733874	7744722	7986017
Sensitivity	0.486	0.451	0.205	0.264
Specificity	0.999	0.999	0.999	0.999
Accuracy	0.999	0.999	0.999	0.999
Precision	0.148	0.145	0.037	0.058
F-measure	0.227	0.219	0.062	0.095
Degree overlap	0.057	0.042	0.019	0.026

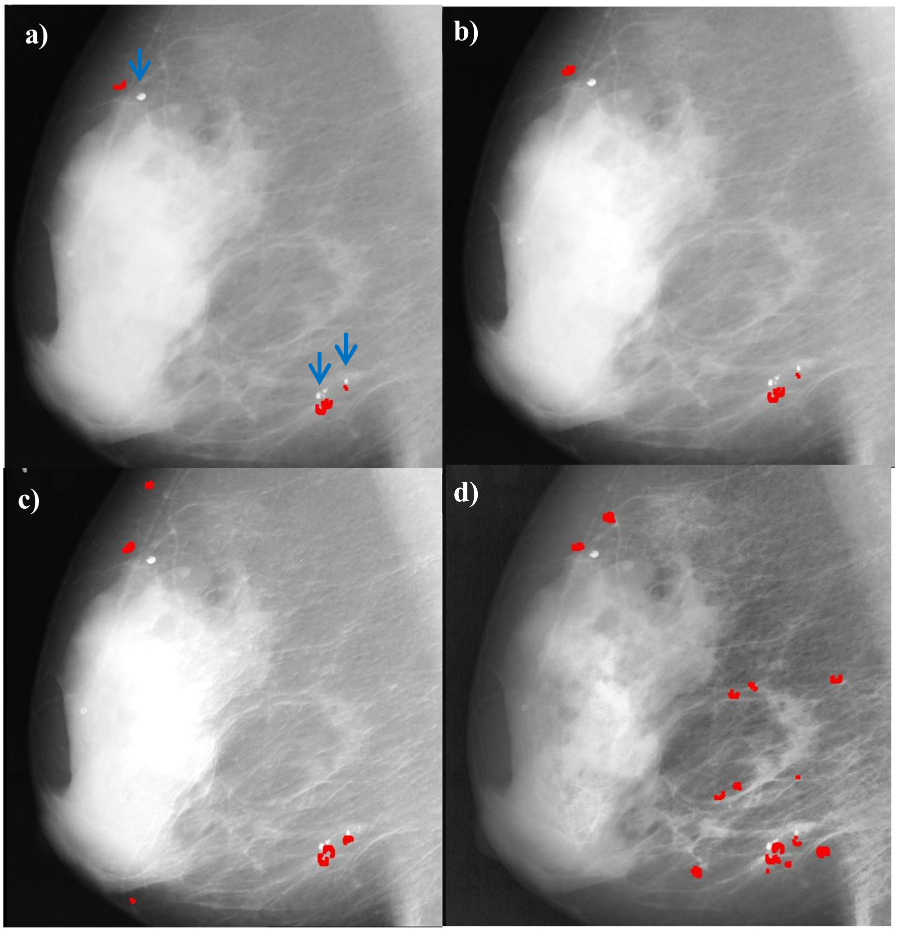

Figure 5.25 – Result of active contour algorithm on a mammographic image: a) no previously image enhancement; b) –d) segmentation after enhancement using: b) linear contrast stretching, c) adaptive unsharp filtering, d) CLAHE with Rayleigh distribution. (The red dots indicate the region detected by the algorithm, while the blue arrows indicate the real microcalcifications).

Table 5.18 and Figure 5.25 provide exemplifying results obtained from the segmentation algorithm using active contours with and without previous image enhancement.

The algorithm provided only sensitivity of 49% and with a high value of FP detections also due to the initial increase in the threshold. However, it is very dependent on the initial objects segmented which are subject of the active contour algorithms.

Several combinations of the different parameters of the active contour algorithm were experimented and the ones presented corresponded to the best result. However, an ideal combination may have not been experimented, which leads to the absent of an ideal result of the implementation of this algorithm.

Comparing the enhancement influence in this technique, contrast stretching slightly reduced the detection of real microcalcifications and slightly decreased the FP detections. Thus sensitivity, precision and F-measure were inferior to the one with no enhancement. Adaptive unsharp and CLAHE filtering had similar results, and decreased the FP detections when compared with no enhancement reducing the non-detection of existent microcalcifications. Thus, no previous enhancement provides a higher balance between sensitivity and specificity.

5.2.7. Comparison of Segmentation Techniques

In the context of mammographic imaging, false negatives have much more importance than false positive detections, as physicists may accept operating with some false positive detections, but do not want to miss malignant lesions (Bothorel, Bouchon, & Muller, 1997). Thus, in all the comparisons made, more importance was given to the specificity of the algorithm.

As sensitivity corresponds to the fraction of the true positive cases over the real positive cases, highest values of sensitivity imply minimal false negative detection. The algorithm with the highest sensitivity corresponded to the edge algorithms (Sobel, Prewitt, and Roberts), followed by region growing, threshold and difference of Gaussians and adaptive threshold. The remaining algorithms had very low degrees of sensitivity. In the case of the threshold and morphological operations, this reduced sensitivity was due to the attempt to reducing the FP detections, which also reduced the TP detection. Snake algorithm did not have a good performance, as it detected few real microcalcifications and had a considerable amount of FP detections. This algorithm is not usually used to detect small objects such as microcalcifications, but to detect higher areas, such as the breast or even to detect blood vessels (Thangavel, Karnan, Sivakumar, & Mohideen, 2005), (Valverde, Guil, & Muñoza, 2004), (Wirth & Stapinski, 2004).

Region based and active contour of selected areas have results that are very dependent on the preprocessing techniques which result in the segmented objects which are provided to the algorithms. Thus, the purpose of those algorithms would correspond to obtain a higher correspondence of the detected objects and the real microcalcifications.

Table 5.19 – Comparison of the evaluation parameters of the segmentation algorithms.

	Adaptive Threshold	Adaptive Threshold & Morphologic Operators	Threshold & Difference of Gaussians	Region Growing	Prewitt	Sobel	Roberts	Snake
FP	152	42	41	195	146	178	44	195
FN	29	51	26	22	11	10	20	36
TP	50	26	51	53	52	53	45	34
TN	7721430	7762108	7762353	7758483	7748205	7746445	7755056	7731288
Sensitivity	0.633	0.338	0.662	0.707	0.825	0.841	0.692	0.486
Specificity	0.99	0.999	0.999	0.999	0.999	0.999	0.999	0.999
Accuracy	0.999	0.999	0.999	0.999	0.999	0.999	0.999	0.999
Precision	0.247	0.382	0.554	0.218	0.263	0.229	0.506	0.148
F-measure	0.356	0.359	0.604	0.327	0.398	0.361	0.584	0.227
Degree overlap	0.177	0.103	0.116	0.389	0.272	0.264	0.410	0.057

Other parameters of evaluation corresponds to specificity of the test, which is the fraction of the true negative cases over the real negative case, where higher values of specificity imply minimal false positive detection. Accuracy measures the global performance of the algorithm about the correct decisions.

The TN values and consequently the specificity and accuracy values were high, as the calculation of the TN corresponds to the detection of all the pixels which are contained in the breast area and do not correspond to TN, FN and FP. Since the classification of the segmented objects was not performed, the calculation of this parameter could not be done with it result. Thus, these values could not be compared with other studies with different TN calculation.

F-measure corresponds to a harmonic mean of precision and sensitivity, thus it provides a balance between those two parameters and, consequently, balances the existence of TP with the FP. So, it indicates whether is preferable to have a higher percentage of TP and a much higher FP percentage or if missing some microcalcifications detection is balanced with a lower FP.

Highest values of precision and F-measure corresponded to the threshold and difference of Gaussians and Roberts' edge operator. The morphological operators, despite a lower TP detection rate, had a high reduction of FP and consequently the F-measure when compared with the adaptive threshold alone is similar. The F-measure in general had a low value due to the high values of false positives. As the majority of segmentation techniques for mammography, the results had a high false positive rate. However, the values obtained could be reduced with the implementation of hybrid methods, as occurred in the majority of the segmentation techniques implemented for mammography. The existence of a classification procedure also may improve the reduction of this value.

The procedures with higher degree of overlap of the segmented image and the real microcalcifications correspond to the region growing methods and edge based segmentation with Roberts' operator. Region growing of selected areas is previously provided with an initial segmentation with rough contour of the microcalcification and intends to provide a more accurate contour of the object. Thus, this procedure is expected to have higher value of degree of overlap. The edge based algorithm, as it was performed with filling operations, allowed a higher degree of overlap. As the other techniques aim to detect the pixels based merely on the gray-level values, reduced degree of overlap was obtained. Features extracted from objects with higher degree of overlap are more realistic and allow a further better classification. Thus, improvements related with higher percentage of overlap are fairly important.

Region growing despite having fewer precision when compared with adaptive threshold, it preprocessing method has sensitivity and degree of overlap, which justifies it implementation and it use for image segmentation.

Adaptive threshold methods had easy implementation; on the other hand, have high FP results and low TP. Pixel separation cannot be accurate in this method. Similar occurs for adaptive threshold and morphological operations; however this method decreases the TP detections while decreases the FP detection. Threshold and difference of Gaussians allowed better detections than the previous methods. Region growing algorithm is time consuming and the result depends greatly on finding suitable seeds. Edge detection is used to find the exact edges of the regions in the mammogram. However, it is time consuming. Snake algorithm did not provide good results and is time consuming and are very dependent on finding suitable initial active contour. The results are sensitive to noise, as proved by the reduced TP with the enhancement methods adaptive unsharp and CLAHE with higher PSNR than the contrast stretching.

As a consequence of the results described, Roberts' edge operator, region growing in selected areas and threshold and difference of Gaussians are considered the segmentation algorithms with best results.

The enhancement algorithms of adaptive unsharp filtering and CLAHE tested with the segmentation methodologies generally increased the TP rate, but increased greatly the FP detections, as introducing additional noise. The contrast stretching enhancement had similar results to the ones with no enhancement, but normally reducing the TP rate. The smoothing filters, although not shown, were tested and the results indicated, as expected, an inferior detection of microcalcifications due to the image blur and consequently reduced the information of image details which difficult the image detection. However, the enhancement techniques had good results in some specific situations, such as higher breast density.

Careful observation was conducted to understand why several microcalcifications were not systematically detected. As observed, those FN were due to dense breasts or to the reduced size of the microcalcifications. Dense breasts implies that breast tissue overlaps the breast lesions, difficulting it detection. Small sized microcalcifications are of difficult detection as they may be considered by the computer as image noise or even an image artifact. The mammographic images chosen to evaluate the implemented algorithms had breasts from different densities, including dense breasts, so consequently, some microcalcifications were of very difficult detection, which reduced the values of sensitivity, specificity, accuracy and the remaining evaluating parameters of all the experiments performed in this dissertation.

It is vital to detect and analyze the detection of microcalcifications in mammograms with various densities (Cheng, Lui, & Freimanis, 1998). Lesions in dense breasts are one of the most common causes for non-detection of breast lesions. Image enhancement is important in those situations, as it may allow a better visualization of breast lesions.

Adaptive unsharp filtering and CLAHE enhancing allowed the reduction of bright areas in the breast, allowing a further identification of possible breast lesions.

Although the achieved performance was satisfactory for some of the segmentation algorithms evaluated, further studies should be carried out for a more precise detection of microcalcifications, aiming the elimination of falsely detected objects.

The majority of the papers describing algorithms implementation for microcalcification detection have hybrid algorithms and not only one segmentation method alone. This allows obtaining of the advantages of the several segmentation algorithms and thus the reduction of the false positive detections and the increasing of true positive detections. Moreover, the implementation of a further classification method may provide the sensitivity and accuracy increasing.

As the images obtained from the database result from the digitalization of mammographic images, some artifacts from digitalization, as well as some information about the exam indicated in the mammographic film may be present in the image. Thus, in order to have segmentation of the breast lesions, which are only present in the breast area, the majority of the algorithms were intersected with the breast region.

5.2.8. Feature extraction

Additionally, some features were extracted from the segmented images in order to perform a further classification. To classify objects for the computational analysis is necessary the existence of robust features.

There is a diversity of features that could be extracted from the segmented objects. The features that were adopted in the present work are: area, perimeter, compactness, diameter, thinness, minimum aspect ratio (MAR), average gray level, average grey level of the background and contrast. These parameters were based on the studies of microcalcification detection of Deshpande et al. (2005) and Woods et al. (1992). Several different features were extracted from the images. The implemented algorithms for feature extractions are presented below.

The area, A, in the object corresponds to the count of ones, n, in the segmented image (Deshpande, Narote, Udupi, & Inamdar, 2005).

The perimeter of a region, P, corresponds to the pixels that belong to the object but are neighbors from the background. The algorithm of the perimeter was computed by subtracting a 1-pixel dilated object from the original segmented object. The perimeter corresponds to the counts of the 1's (ones) resulting from the previous proceeding.

The compactness (Zhang, Qian, Sankar, Song, & Clark, 2001), *C*, is a measure of shape, which indicates how an object is compact, and was determined as:

$$C = \frac{P^2}{4\pi A}. \qquad \textbf{(5.18)}$$

The diameter, D_y, of the object was determined through the count of the distinct rows of the object. The same was performed for the columns, D_x.

Thinness (Deshpande, Narote, Udupi, & Inamdar, 2005) is a measure of contour complexity versus enclosed area. It can be described by T_a and T_b, defined by:

$$T_a = (p^2 / A - 4\pi), \qquad \textbf{(5.19)}$$

$$T_b = D_y / A. \qquad \textbf{(5.20)}$$

Minimum aspect ratio (MAR) (Deshpande, Narote, Udupi, & Inamdar, 2005) corresponds to the ratio of diameter in both directions:

$$MAR = \frac{D_y}{D_x}. \qquad \textbf{(5.21)}$$

The average gray level implies the determination of this parameter for the objects and for the background. The background gray level was considered the neighborhood of 2 pixels surrounding the objects. The difference from the object dilated with a 2 pixels structuring object from the original object was performed in order to determine the region of the neighborhood. Afterwards, the average of the gray levels of the correspondent region in the grayscale image was determined. The computation of the average gray level of the object was performed similarly to the former operation.

Contrast, as previously introduced by equation 4.9, is determined by the ratio of the difference between average gray level of the object and the background, and the sum of the average gray level of the object and the background.

From those features extracted, a dataset was created with the information of each objected detected and it classification (TP or FP) according to the parameters previously defined.

Preliminary studies with the classification method K-Nearest Neighbor, from the PR-Tools of MATLAB® were performed in order to determine whether this classification can reduce the FP detections, while maintaining the TP. The results obtained were promising as they allowed the FP decrease, but also with a slight decrease in the TP. Further work is in progress to establish a more accurate evaluation of this classification and to determine the best parameters which provide less TP misdetection.

To classify the microcalcifications according to the malignancy, feature selection could have been performed in order to obtain the most accurate classification. As a future perspective, several different parameters could be obtained and be used to have a more accurate classification.

5.3. Summary

In this chapter is described the implementation, results and segmentation of several algorithms. The image enhancement techniques implemented corresponded to CLAHE, contrast stretching, unsharp and adaptive unsharp filtering, ANCE, homomorphic filtering and median filtering. Those enhancement techniques were evaluated based on the parameters CII, BNL, PSNR and ASNR. From this analysis was concluded that the majority of the enhancement algorithms increase the contrast improvement index, but also increase the noise level of the image. The adaptive methods had, in general, better enhancement performance.

Some image enhancement techniques were also implemented and evaluated: adaptive threshold, adaptive threshold and morphological operators, threshold and difference of Gaussians, region growing of selected areas, edge based segmentation and active contours of selected areas. The effect of the image enhancement techniques on the results of the mammographic microcalcifications segmentation techniques was also analyzed, where in general the enhancement algorithms increased the detection of FP and slightly increased the detection of TP. However, the enhancement, mainly of adaptive unsharp filtering and CLAHE, allowed the detection of microcalcifications in dense breasts, which corresponds to difficult microcalcification detections. The segmentation technique edge detectors and regions growing of selected areas had higher sensitivity, while edge detection Roberts' and threshold and difference of Gaussians had higher accuracy, precision and F-measure. Roberts' operator and region growing of selected areas allowed a higher degree of overlap of the segmented objects with the real existent microcalcifications. Consequently, Roberts' edge operator, region growing in selected areas and threshold followed by difference of Gaussians correspond to the segmentation algorithms with best results.

Additionally, some features were extracted from the segmented objects: area, perimeter, compactness, diameter, thinness, minimum aspect ratio (MAR), average gray level, average grey level of the background and contrast. This extraction allowed the creation of a dataset. Preliminary classification about the presence or not of microcalcifications indicates that it may reduce highly the FP detections.

CHAPTER 6

CONCLUSIONS AND FUTURE PERSPECTIVES

CAD is an important tool for early breast cancer detection. Over the past 20 years, a significant amount of work has been done in this area. Therefore, this dissertation aimed to analyze automatic enhancement and segmentation of microcalcifications in mammographic images.

Automatic detection of microcalcifications corresponds to a difficult task due to several reasons: the objects of interest can be very small; can have different sizes and shapes; the regions of interest may have low contrast; the density of some breast may hide some lesions, and calcifications can be present against a background with very differences in intensity and contrast. (Cheng, Lui, & Freimanis, 1998). Still, the sensibility of existent segmentation methods is already high.

In this dissertation, a research about the breast anatomy and pathologies was performed, as well as an examination about the physics behind the acquisition of the mammographic images. A study about the usual methodologies to process and analyze mammographic images was also achieved. Posteriorly, some image enhancement techniques were implemented such as CLAHE, contrast stretching, unsharp and adaptive unsharp filtering, ANCE, homomorphic filtering and median filtering. Those enhancement techniques were evaluated based on some parameters: CII, BNL, PSNR and ASNR, where was concluded that the majority of the enhancement algorithms increase the contrast improvement index, but also increases the noise level of the image. The adaptive methods had, in general, better enhancement performance.

Several image enhancement techniques were also implemented and evaluated. The segmentation algorithms were: adaptive threshold, adaptive threshold and morphological operators, adaptive threshold and difference of Gaussians, region growing of selected areas, edge based segmentation and active contours of selected areas. The effect of the image enhancement techniques on the results of the mammographic microcalcifications segmentation techniques was also analyzed. Overall the enhancement algorithms increased the detection of existent microcalcifications, while highly increased the false positive detections. Nevertheless, the image enhancement allowed the detection of microcalcifications in dense breasts. The segmentation technique edge detectors and regions growing of selected areas had higher sensitivity, while edge detection Roberts's and threshold and difference of Gaussians had higher accuracy, precision and F-measure. Roberts' edge operator and region growing of selected areas allowed a higher degree of overlap of the segmented objects with the real existent microcalcifications, important characteristic for feature extraction. Thus, Roberts' edge operator, region growing in selected areas and threshold and difference of Gaussians correspond to the segmentation algorithms with best results. A dataset was additionally created with the features extracted from the segmented objects and preliminary classification studies were performed.

Thus, the objectives proposed for this dissertation were met and even exceeded.

Although the achieved performance was satisfactory for some of the segmentation algorithms evaluated, further studies should be carried out for a more precise detection of microcalcifications, aiming the elimination of falsely detected objects, for the detection of subtle signs and for the detection of breast lesions in dense breasts. The enhancement methods are mainly important in those situations. Algorithms such as unsharp masking can unhide some breast lesions and thus enable the radiologist to perform a more accurate diagnosis. Several different techniques could be performed in order to reduce the false positive detection such as the implementation of hybrid methods, as occurred in the majority of the segmentation techniques implemented for mammography or even the implementation of a classification to define if the object detected corresponds or not to a microcalcification.

Further work is in progress to establish the utility of these techniques by ROC curves. Additional experiments will be performed in a higher number of mammographic images obtained from the database. Additional features could also be extracted from the segmented objects such as the location of the microcalcification in the breast or texture information. Further studies could also compare the different classification methods, as well as additional segmentation and enhancement techniques.

The study of the contralateral breast and the other perspectives of the mammography may also reduce those false negative rates and provide some additional information about the malignity of the lesion. The information of presence of masses, bilateral asymmetry, architectural distortion, breast shape should also be provided in order to enable a more efficient and early detection of breast cancer.

Although important progress has been done over the last years, much work still needs to be done to develop more efficient CAD systems. CAD systems should lead to early detection of breast cancer and consequently to improved prognosis for those affected by the disease.

REFERENCES

Band-pass Filtering Vs. Multiscale Dyadic Wavelet Transform for Contrast Enhancement of Digital Mammograms. (2005). *AAPM 47th Annual Meeting.* Washington.

Akay, M. (2006). *Wiley Encyclopedia of Biomedical Engineering* (1st ed.). Wiley Interscince.

Arnau, O. (2007). *Automatic mass segmentation in mammographic images.* Universitat de Girona, Department of Electronics, Computer Science and Automatic Control, Girona.

Astley, S. (2003). Computer-aided detection for screening mammography. *International Congress Series, 1256*, pp. 927-932.

Autier, P., Boniol, M., LaVecchia, C., Vatten, L., Gavin, A., Héry, C., et al. (2010). Disparities in breast cancer mortality trends between 30 European countries: retrospective trend analysis of WHO mortality database. *BMJ 2010*, 341:c3630.

Bae, U., Shamdasani, V., Managuli, R., & Kim, Y. (2003, June). Fast Adaptive Unsharp Masking with Programmable Mediaprocessors. *Journal of Digital Imaging, 16, No. 2*, 230-239.

Baert, A., Reiser, M., Hricak, H., & Kanuth, M. (2010). *Digital Mammography.* Springer.

Baker, J., Rosen, E., Lo, J., Gimenez, E., Walsh, R., & Soo, M. (2003). Computer-Aided Detection (CAD) in Screening Mammography: Sensitivity of Commercial CAD Systems for Detecting Architectural Distortion. *AJR Am J Roentgenol., 181, No 4.*

Bankman, I., Nizialek, T., Simon, I., Gatewood, O., Weinberg, I., & Brody, W. (1997). Segmentation algorithms for detecting microcalcifications in mammograms. *IEEE Trans Inf Technol Biomed.*

Bastos, J., Barros, H., & Lunet, N. (2007). Evolução da Mortalidade por Cancro da Mama em Portugal. *Acta Med Port, 20*, pp. 139-144.

Bird, R., Wallace, T., & Yankaskas, B. (1992, Sep.). Analysis of cancers missed at screening mammography. *Radiology*, pp. 613-617.

Blanks, R., Wallis, M., & Moss, S. (1998). A comparison of cancer detection rates achieved by breast cancer screening programmes by number of readers, for one and two view mammography: results from the UK National Health Service breast screening programme. *J Med Screen, 5*, pp. 195-201.

Bothorel, S., Bouchon, B., & Muller, S. (1997, November - December). A fuzzy logic based approach for semiological analysis of microcalcifications in mammographic images. *International Journal of Intelligent Systems, 12*(11-12), 819–848.

Bronzino, J. (2000). *The Biomedical Engineering Handbook* (2nd ed., Vol. 1). U.S.: CRC Press.

Bruce, L. M., & Adhami, R. R. (1999, Dec.). Classifying Mammographic Mass Shapes Using the Wavelet Transform Modulus-Maxima Method. *IEEE Trans. Medical Imaging, 18, No.12*, pp. 1170-1177.

Burhenne, L., Wood, S., D'Orsi, C., Feig, S., Kopans, D., O'Shaughnessy, K., et al. (2000). Potential Contribution of Computer-aided Detection to the Sensitivity of Screening Mammography. *Radiology, 215*, pp. 554-562.

CADx. (2003). *http://cadxmed.com/.* Retrieved Jan. 16, 2011, from http://cadxmed.com/

Chagas, F., Rodrigues, D., Tavares, J., Reis, A., Miranda, D., & Duarte, R. (2007). An Application of Hough Transform to Identify Breast Cancer in Images. *VIPimage.*

Chan, H., Vyborny, C., MacMahon, H., Metz, C., Doi, K., & Sickles, E. (1987, July). Digital mammography. ROC studies of the effects of pixel size and unsharp-mask filtering on the detection of subtle microcalcifications. *Invest Radiology, 22*(7), 581-589.

Cheng, H., Cai, X., Chen, X., Hu, L., & Lou, X. (2003). Computer-aided detection and classication of microcalcifications in mammograms: A survey. *Pattern Recognition, 36*, pp. 2967 – 2991.

Cheng, H., Lui, Y., & Freimanis, R. (1998, June). A Novel Approach to Microcalcification Detection Using Fuzzy Logic Techniques. *IEEE Trans on Medical Imaging, 17, No 3*.

Cheng, H., Wang, J., & Shi, X. (2004). Microcalcification Detection Using Fuzzy Logic and Scale Space Approaches. *Pattern Recognition, 37*, pp. 363-375.

Ciatto, S., Del Turco, M., Risso, G., Catarzi, S., Bonardi, R., Viterbo, V., et al. (2003, Feb). Comparison of standard reading and computer aided detection (CAD) on a national proficiency test of screening mammography. *Eur J Radiol., 45, No.2*.

Daponte, J., & Fox, M. (1988). Enhancement of chest radiographs with gradient operators. *IEEE Trans Medical Imaging, 7, no.2*, 109-117.

Dengler, J., Behrens, S., & Desaga, J. (1993, Dec). Segmentation of Microcalcifications in Mammograms. *IEEE Trans on Medical Imaging, 12, No 4*.

Deshpande, A., Narote, S. P., Udupi, V., & Inamdar, H. P. (2005). A Region Growing Segmentation for Detection of Microcalcification in Digitized Mammograms. *International Conference on Cognition and Recognition*, (pp. 774-779).

Dhawan, A., Buelloni, G., & Gordon, R. (1986, March). Enhancement of Mammographic Features by Optimal Adaptive Neighborhood Image Processing. *IEEE Trans on Medical Imaging, 5, No 1*.

Doi, K. (2007). Computer-aided diagnosis in medical imaging: Historical review, current status and future potential. *Comput Med Imaging Graph., 31, No. 4-5*, pp. 198-211.

Eastman, G. W., Wald, C., & Crossin, J. (2006). *Getting Started in Clinical Radiology - From image to diagnosis.* Thieme.

Eberl, M., Fox, C., Edge, S., Carter, C., & Mahoney, M. (2006, Mar-Apr). BI-RADS Classification for Management of Abnormal Mammograms. *J Am Board Fam Med, 19, No 2*.

Evans, K. (2007). *Mammography: The Promise of Improved Brest Cancer Detection.* eRadimaging.

Ferlay, J., Shin, H., Bray, F., Forman, D., Mathers, C., & Parkin, D. (2010). *GLOBOCAN 2008.* Retrieved from Cancer Incidence and Mortality Worldwide: IARC CancerBase: http://globocan.iarc.fr

Freer, T., & Ulissey, M. (2001). Screening mammography with computer-aided detection: Prospective study of 12860 patients in a Community Breast Center. *Radiology, 220*, pp. 781-786.

Gelas, A., Bernard, O., Friboulet, D., & Prost, R. (2007, July). Compactly Supported Radial Basis Functions Based Collocation Method for Level-Set Evolution in Image Segmentation. *IEEE Trans on Image Processing, 16, No 7*.

Giger, M. L. (2004, Oct). Computerized Analysis of Images in the Detection and Diagnosis of Breast Cancer. *Semin Ultrasound CT MR, 25, Nº5*.

Gonzalez, R., & Woods, R. (2002). *Digital Image Processing* (2nd Edition ed.). New Jersey: Prentice Hall, Inc.

Gray, H. (2000). *Anatomy of the Human Body.* New York: Bartleby.

Grohman, W., & Dhawan, A. (2001). Fuzzy convex set-based pattern classification for analysis of mammographic microcalcifications. *Pattern Recognition, 34, No 7*, pp. 1469-1482.

Gunderman, R. B. (2006). *Essential radiology: clinical presentation, pathophysiology, imaging.* Thieme.

Guyton, A. C., & Hall, J. E. (2000). *Textbook of Medical Physiology* (10th ed.). (W. S. Company, Ed.)

Haus, A., & Yaffe, M. (2000, July). Screen Film and Digital Mammography: Image Quality and Radiation Dose Considerations. *Radiologic Clinics of North America, 38, No.4*, pp. 871-898.

Heine, J., Deans, S., Cullers, D., Stauduhar, R., & Clarke, L. (1997, Oct.). Multiresolution Statistical Analysis of High-Resolution Digital Mammograms. *IEEE Trans on Medical Imaging, 16, No 5*, pp. 503-515.

Hologic. (2010). *R2 Image Checker*. Retrieved Jan. 16, 2011, from R2 ImageChecker Digital CAD: http://www.hologic.com/pt/breast-screening/imagechecker/

Houssami, N., Given-Wilson, R., & Ciatto, S. (2009, Apr). Early detection of breast cancer: overview of the evidence on computer-aided detection in mammography screening. *J Med Imaging Radiat Oncol., 53, No.2*.

Humar, P. (2009). *Matlab Exchange*. Retrieved April 2011, from Homomorphic Filtering: Homomorphic Filtering

iCAD. (2009). *iCad*. Retrieved Jan. 16, 2011, from http://www.icadmed.com/

Jähne, B. (2005). *Digital Image Processing* (6th edition ed.). Springer.

Ji, T., Sundareshan, M., & Roehrig, H. (1994, December). Adaptive Image Contrast Enhancement Based on Human Visual Properties. *IEEE Trans on Medical Imaging, 13, No. 4*.

Kallergi, M., Woods, K., Clarke, L., Qian, W., & Clark, R. (1992, Sept-Oct). Image segmentation in digital mammography: Comparison of local thresholding and region growing algorithms. *Computerized Medical Imaging and Graphics, 16, No 5*, pp. 323-331.

Karssemeijer, N. (1993). Adaptive Noise Equalization and Image Analysis in Mammography. In H. Barrett, & A. Gmitro, *Information Processing in Medical Imaging* (Vol. 687, pp. 472 - 486). Springer Berlin / Heidelberg.

Karssemeijer, N., & Brake, G. (1996, Oct). Detection of Stellate Distortions in Mammograms. *IEEE Trans on Medical Imaging, 15, No 5*.

Kass, M., Witkin, A., & Terzopoulos, D. (1988). Snakes active contour models. *International Journal of Computer Vision*, pp. 323-331.

Kaushak, C. (2007). Breast Mammography: Pictorial Review. *Indian Journal for the Practising Doctor, 4, No.1*.

Kendall, A. (2009, Mar). *Mathworks.* Retrieved June 16, 2011, from Determine and count unique values of an array: http://www.mathworks.com/matlabcentral/fileexchange/23333-determine-and-count-unique-values-of-an-array

Khoo, L., Taylor, P., & Given-Wilson, R. (2005). Computer-aided Detection in the United Kingdom National Breast Screening Programme: Prospective Study. *Radiology, 237*, pp. 444-449.

Kim, J., Park, J., Song, K., & Park, H. (1997, Oct). Adaptive mammographic image enhancement using first derivative and local statistics. *IEEE Trans on Medical Imaging, 16, No 5*.

Kimme-Smith, C., Gold, R., Bassett, L., Gormley, L., & Morioka, C. (n.d.). Diagnosis of breast calcifications: comparison of contact, magnified, and television-enhanced images. *American Journal of Roentgenology, 153, No 5*, pp. 963-967.

Kroon. (2010, July). *Snake - active contour*. Retrieved April 2011, from The Mathworks: http://www.mathworks.com/matlabcentral/fileexchange/28149-snake-active-contour

Kroon, D. (2008, March 06). *Matlab Central.* Retrieved April 16, 2011, from Region Growing: http://www.mathworks.com/matlabcentral/fileexchange/19084

Lai, S., Li, X., & Bischof, W. (1989, Dec). On Techniques for Detecting Circumscribed Masses in Mammograms. *IEEE Trans on Medical Imaging, 8, No 4*.

Laine, A., Fan, J., & Schuler, S. (1994). A framework for contrast enhancement by dyadic wavelet analysis. *Proc. 2nd Int. Workshop on Mammography*, (pp. 91-100).

Laine, A., Fan, J., & Yang, W. (1995, September). Wavelets for Contrast Enhancement of Digital Mammography. *IEEE Engineering in Medicine and Biology*, 536-550.

Laine, A., Schuler, S., Fan, J., & Huda, W. (1994, September). Mammographic Feature Enhancement by Multiscale Analysis. *IEEE Trans on Medical Imaging, 13, No 4*.

Lau, T., & Bischof, W. (1991, June). Automated detection of breast tumors using the asymmetry approach. *Comput Biomed Res., 24, No 3*.

Lee, C. (2002). Screening mammography: proven benefit, continued controvery. *Radiology Clinics of North America, 40*, pp. 395-407.

Lee, C. H., Dershaw, D. D., Kopans, D., Evans, P., Monsees, B., Monticciolo, D., et al. (2010, January). Breast Cancer Screening With Imaging: Recommendations From the Society of Breast Imaging and the ACR on the Use of Mammography, Breast MRI, Breast Ultrasound, and Other Technologies for the Detection of Clinically Occult Breast Cancer. *Journal of the American College of Radiology, 7*.

Li, H., Liu, R., & Lo, S. (1997, December). Fractal Modeling and Segmentation for the Enhancement of Microcalcifications in Digital Mammograms. *IEEE Trans on Medical Imaging, 16*(6), 785-798.

Lima, J. (1995). *Física dos Métodos de Imagem com Raios-X.* Coimbra: Asa.

Ma, Z., Tavares, J. M., Jorge, R. N., & Mascarenhas, T. (2009, August 04). A Review of algortihms for medical image segmentation and their applications to female pelvic cavity. *Computer Methods in Biomechanics and Biomedical Engineering*.

Masala, G. (2006). Computer Aided Detection on Mammography. *World Academy of Science, Engineering and Technology, 15*.

Masala, G. (2006). Pattern Recognition Techniques Applied to Biomedical Patterns. *International Journal of Biological and Medical Sciences*.

Mencattini, A., Salmeri, M., Rabottino, G., & Salicone, S. (2010, Nov). Metrological Characterization of a CADx System for the Classification of Breast Masses in Mammograms. *IEEE Trans Instrumentation and Measurement, 59, No.11*, pp. 2792-2799.

Miller, P., & Astley, S. (1994). Automated detection of breast asymmetry. *Series in Machine, 9*, pp. 247-261.

Mini, M., & Thomas, T. (2003, Oct 15-17). A neural network method for mammogram analysis based on statistical features. *TENCON 2003. Conference on Convergent Technologies for Asia-Pacific Region, 4*, pp. 1489- 1492.

Morrow, W., Paranjape, R., Rangayyan, R., & Desautels, J. (1992, Sept). Region-based contrast enhancement of mammograms. *IEEE Trans on Medical Imaging, 11, No 3*.

Mudigonda, N., & Rangayyan, R. (2001, Dec). Detection of Breast Masses in Mammograms by Density Slicing and Texture Flow-Field Analysis. *IEEE Trans on Medical Imaging, 20, No. 12*.

Näppi, J., & Dean, P. (2000, May). A Multiscale Algorithm for Segmenting Calcifications from High-Resolution Mammographic Specimen Radiographs. *Journal of Digital Imaging, 113*(2), 130-132.

Narendra, P., & Fitch, R. (1981, November). Real-time adaptive contrast enhancement. *IEEE Trans. Pattern Anal Machine InteII, PAMI-3*, 655-661.

Nersissian, D. (2004). *Determinação das Dimensões do Ponto Focal de Tubos de Raio-X utilizando um Sensor CCD e o Método das Funções de Transferências.* Tese de Doutoramento em ENgenharia Eléctrica, Universidade de São Paulo.

Nesbitt, D., Aghdasi, F., Ward, R., & Morgan-Parkes, J. (1995). Detection of microcalcifications in digitized mammogram film images using wavelet enhancement and local adaptive false positive suppression. *IEEE Pacific Rim Conference on Conference on Communications, Computers, and Signal Processing.*

NHSBSP Equipment. (2009, April). Commisioning and Routine Testing of Full Field Digital Mammography System. *0604, 3*.

Oliver, A., Lladó, X., Pérez, E., J., P., Denton, E., Freixenet, J., et al. (2010, Oct). A Statistical Approach for Breast Density Segmentation. *J Digit Imaging, 23, No.5*.

Osher, S., & Sethian, J. (1988). Fronts Propagating with Curvature Dependent Speed:Algorithms Based on Hamilton-Jacobi Formulations. *Journal of Computational Physics, 79*, pp. 12-49.

Papadopoulos, A., Fotiadis, D., & Likas, A. (2002). An Automatic Microcalcification Detection System Based on a Hybrid Neural Network Classifier. *Artificial Intelligence in Medicine, 25*, pp. 146-167.

Pisano, E., & Yaffe, M. (2005). Digital Mammography. *Radiology, 234*, pp. 353–362.

Pizer, S., Amburn, E., Austin, J., Cromartie, R., Geselowitz, A., Greer, T., et al. (1987, Sept). Adaptive histogram equalization and its variations. *Computer Vision, Graphics, and Image Processing, 39, No 3*.

Rangayyan, El-Faramawy, Desautels, & Alim. (1997). Measures of acutance and shape for classification of breast tumors. *IEEE Trans. Medical Imaging, 16, No 6*, 799-810.

Rangayyan, R. (2005). *Biomedical Image Analysis.* CRC Press.

Rangayyan, R., Ayres, F., & Desautels, J. (2007). A review of computer-aided diagnosis of breast cancer: Toward the detection of subtle signs. *Journal of the Franklin Institute, 344*, pp. 312-348.

Rangayyan, R., Shen, L., Shen, Y., Desautels, J., Bryant, H., Terry, T., et al. (1997, September). Improvement of Sensitivity of Breast Cancer Diagnosis with Adaptive Neighborhood Contrast Enhancement of Mammograms. *IEEE Trans on Information Technology in Biomedicine, 1, no.3*, 161-170.

Saha, P., Udupa, J., Conant, E., Chakraborty, D., & Sullivan, D. (2001, Aug.). Breast tissue density quantification via digitized mammograms. *IEEE Trans on Medical Imaging, 20, No 8*, pp. 792-803.

Sampat, M., Markey, M., & Bovik, A. (2005). Computer-Aided Detection and Diagnosis in Mammography. In A. Bovik, *Handbook of Image and Video Processing* (pp. 1195-1217). Elsevier.

Sankar, D., & Thomas, T. (2010, Oct). A New Fast Fractal Modeling Approach for the Detection of Microcalcifications in Mammograms. *J Digit Imaging. 2010 Oct;23(5):538-46. Epub 2009 Jul 18., 23, N.5*, pp. 538-546.

Schulz-Wendtland, R., Fuchsjäger, M., Wackerc, T., & Hermannd, K. (2009). Digital mammography: An update. *European Journal of Radiology, 72*, pp. 258-265.

Seeley, R., Stephens, T., & Tate, P. (2004). *Anatomy and Physiology.* The McGraw−Hill Companies.

Seker, H., Odetayo, M., Petrovic, D., & Naguib, R. (2003, June). A Fuzzy Logic Based Method for Prognostic Decision Making in Breast and Prostate Cancers. *IEEE Trans on Information Technology in Biomedicine, 7, No 2*.

Shapiro, L., & Stockman, G. (2002). *Computer Vision.* Prentice Hall.

Simonetti, G., Cossu, E., Montanaro, M., Caschili, C., & Giuliani, V. (1998). What's new in mammography. *European Journal of Radiology, 27*, pp. 234-241.

Sivaramakrishna, R., Obuchowski, N., Chilcote, W., Cardenosa, G., & Powell, K. (2000). Comparing the Performance of Mammographic Enhancement Algorithms. *AJR, 175*, pp. 45-51.

Soille, P. (1999). Morphological Image Analysis: Principles and Applications. *Springer-Verlag*, 173-174.

Strickland, R., & Hahn, H. (1996, April). Wavelet transforms for detecting microcalcifications in mammograms. *IEEE Trans on Medical Imaging, 15, No 2*.

Suckling, J. (1994). *The Mammographic Image Analysis Society Digital Mammogram Database Exerpta Medica.* (I. C. Series, Editor) Retrieved from http://peipa.essex.ac.uk/info/mias.html

Taplin, S., Rutter, C., & Lehman, C. (2006). Testing the Effect of Computer-Assisted Detection on Interpretive Performance in Screening Mammography. *AJR, 187*, pp. 1475-1482.

Taylor, C., Champness, J., Reddy, M., Taylor, P. P., & Given-Wilson, R. (2003, Sep.). Reproducibility of Prompts in Computer-aided Detection (CAD) of Breast Cancer. *Clinical Radiology, 58, No.9*, pp. 733-738.

Thangavel, K., Karnan, M., Sivakumar, R., & Mohideen, A. (2005). Automatic Detection of Microcalcification in Mammograms– A Review. *ICGST International Journal on Graphics, Vision and Image Processing*, (pp. 31-61).

The MathWorks, Inc. . (2011). *fspecial*. Retrieved March 2011, from The Mathworks: http://www.mathworks.com/help/toolbox/images/ref/fspecial.html

Tiu, C., Jong, T., & Hsieh, C. (2008). Self organizing map neural network with fuzzy screening for micro-calcifications detection on mammograms. *IEE Conference on Soft Computing in Industrial Applications.*

Valverde, F., Guil, N., & Muñoza, J. (2004). Segmentation of Vessels from Mammograms Using A Deformable Model. *Computer Methods and Programs in Biomedicine, 73*, pp. 233-247.

Wang, S., Lim, K., Khoo, B., & Wang, M. (2007). A Geometric Deformation Constrained Level Set Method for Structural Shape and Topology Optimization. *CMES, 18, No 3*, pp. 155-181.

Wang, T., & Karayiannis, N. (1998, Aug.). Detection of Microcalcifications in Digital Mammograms Using Wavelets. *IEEE Trans on Medical Imaging, 17, No 4*.

Wang, X., Lederman, D., Tan, J., & Zheng, B. (2010). Computer-aided Detection: The Impact of Machine Learning Classifier and Image Feature Selection on Scheme Performance. *IJIIP: International Journal of Intelligent Information Processing, 1, No 1*.

Webster, J. (2006). *Encyclopledia of Medical Devices and Instrumentation* (2nd ed., Vol. 4). U.S.: Wiley Insterscience.

Wei, L., Yang, Y., & Nishikawa, R. (2005, Oct.). Relevance vector machine for automatic detection of clustered microcalcifications. *IEEE Trans on Medical Imaging, 24, No 10*.

Wei, L., Yang, Y., & Nishikawa, R. (2009, June). Microcalcification classification assisted by content-based image retrieval for breast cancer diagnosis. *Pattern Recognition, 42, No 6*, pp. 1126-1132.

Wellner, P. (1993). *Adaptive Thresholding for the DigitalDesk.* Rank Xerox Research Centre - Cambridge Laboratory.

Winsberg, F., Elkin, M., Macy, J., Bordaz, V., & Weymouth, W. (1967, Aug.). Detection of Radiographic Abnormalities in Mammograms by Means of Optical Scanning and Computer Analysis. *Radiology, 89*, pp. 211-215.

Wirth, M., & Stapinski, A. (2004, May). Segmentation of the breast region in mammograms using snakes. *Computer and Robot Vision*, pp. 385-392.

Woods, K., Doss, C., Bowyer, K., Clarke, L., & Clark, R. (1992). A neural network approach to microcalcification detection. *Nuclear Science Symposium and Medical Imaging Conference*, *2*, pp. 1273-1275.

Yang, C. (2006). Image enhancement by modified contrast-stretching manipulation. *Optics & Laser Technology, 38*, 196-201.

Yoon, J., & Ro, Y. (2002, January). Enhancement of the Contrast in Mammographic Images Using the Homomorphic Filter Method. *IEICE Trans on Information and Systems, E85-D, no. 1*, 298-303.

Zhang, L., Qian, W., Sankar, R., Song, D., & Clark, R. (2001). A new false positive reduction method for MCCs detection in digital mammography. *Acoustics, Speech, and Signal Processing, IEEE International Conference on*, *2*, pp. 1033-1036.

Zuiderveld, K. (1994). Contrast Limited Adaptive Histograph Equalization. In *Graphic Gems IV* (pp. 474–485). San Diego: Academic Press Professional.